Doctoral Dissertation
Doctoral Program in Aerospace Engineering (36th cycle)

Lagrangian dynamics in wall-bounded transitional and turbulent flows: Particle tracking and network-based analyses

Davide Perrone

* * * * *

Supervisors
Prof. Stefania Scarsoglio, Supervisor
Prof. Luca Ridolfi, Co-supervisor

Doctoral Examination Committee:
Prof. Guido Boffetta, Referee, Università degli Studi di Torino
Prof. Cristian Marchioli, Referee, Università degli Studi di Udine
Prof. Gabriele Bellani, Università di Bologna
Prof. Francesco Avallone, Politecnico di Torino
Prof. Costantino Manes, Politecnico di Torino

Politecnico di Torino
May 17th, 2024

I hereby declare that, the contents and organisation of this dissertation constitute my own original work and does not compromise in any way the rights of third parties, including those relating to the security of personal data.

....

Davide Perrone

Turin, May 17th, 2024

Summary

The goal of this Thesis is to combine results from high-resolution numerical simulations with novel analysis methodologies to shed light on the characterizing processes of wall-bounded turbulence and transition. By exploiting large quantities of data and designing analysis frameworks that are able to leverage such data, new insights are gained on several aspects of wall-bounded turbulence. Among these methods, a particular relevance will be occupied by graph-based approaches, which we use to model certain fluid features as sets of interactions.

The results presented hereafter include mainly contributions from the Lagrangian viewpoint of fluid dynamics, *i.e.*, the viewpoint where the observer moves with the fluid. We used this approach to study the dispersion of tracers in channel flow at varying Reynolds number, which we analysed by means of a discretized representation of their motion which was in turn translated into a network. By doing so, the role of near-wall coherent structures and their influence on particle dispersion was quantified. Moreover, Reynolds scaling properties were measured and a Reynolds independence was found in the outer flow.

The mixing of inertial particles was also studied in channel flow. In this case, mixing was quantified by measuring close encounters of particle pairs. In particular, the relation between the spatially heterogeneous timescales of the flow and the inertia of particles was explored, showing that clustering phenomena do not appear at the same locations for different particles, but instead are dependent on the position inside the channel.

Finally, the deformation of puffs in a transitional channel flow was studied. The numerical simulation of transition involves a spatially evolving flow, which is laminar with wave-like perturbations at the inlet and turbulent at the outlet. Puff deformation is measured by computing the principal axes of the particle cloud, which provides simplified measures regarding their size and elongation. We characterized the interplay between the flow scales and the puff deformation, which are mainly ruled by the puff size. In particular, we found that small puffs are more stretched than larger ones, and that this effect is heightened in the transitional region. By measuring other flow features, we link this behaviour to the intermittency typical of transition.

From the Eulerian perspective, we employed a network-based approach, the visibility graph, to study boundary layer transition. We transform fixed-point time-series into a graph by means of a convexity criterion. Similarly to other studies in this work, a methodological innovation is used here with the aim of shedding light on particular aspects of a known fluid problem, namely identification of turbulent regions in transitional flows. The properties of the resulting graph are able to describe the geometric features of the time-series, which we in turn relate to the properties of the underlying flow. In particular, we found that the visibility approach is particularly sensitive to the transition from an intermittent state to a fully turbulent one. We use this feature to provide a characterization of the turbulent-non turbulent interface starting from spatially coarse data.

All these approaches are characterized by the necessity of treating very large quantities of data, which are significantly extensive in time and space. The key challenges in this case lie in the generation of the data itself, which will be covered in the following with particular regard to the numerical simulation of channel flows, and in the interpretation of the results. The analysis frameworks include network-based approaches, which are powerful tools in fluid dynamics as they enable the uncovering of several key interactions taking place in turbulent flows.

Acknowledgements

I wish to thank my supervisors, Stefania Scarsoglio and Luca Ridolfi, for leading me in the discovery of scientific research. Their help went beyond what was expected, especially when it was needed the most.

I am indebted to Hans Kuerten for graciously welcoming me in Eindhoven. His research and his help greatly contributed to my work in the past few years. I am also grateful to Peter and Hamed.

At Politecnico I worked alongside many great colleagues, especially Emanuele, Salvatore, Cesare, Francesco, Daniel and Alessandro. I found a sincere friend in Matteo, without whom my experience would not have been the same.

I thank my father, whose support never wavered, and my mother, whom I miss dearly.

Words cannot express in full how grateful I am to Elisa.

Contents

Chapter 1

Introduction

The motion of Newtonian fluid flows is the result of the interaction of viscous and inertia forces. Although in some cases viscous forces prevail, smoothing the velocity field so that regular, *laminar* solutions arise, in most engineering applications and geophysical phenomena the inertial effects are dominant. In the mathematical description of fluid motion, *i.e.*, the Navier-Stokes equations, the dominant effect of inertia translates to the presence of nonlinear interactions inside the flow [211].

Following from the nonlinear features of fluid motion, energy, which enters the flow through an external forcing, is transferred from the largest eddies to smaller ones and so on. The direct consequence of the energy cascade is that the velocity field loses its smoothness and is instead characterized by features of several, different scales. Turbulence is the resulting broadband, seemingly chaotic superimposition of eddies in a fluid flow. If the inertia prevails over viscous forces, the motion of fluids departs from the unstable laminar solution and experiences transition to turbulence, *i.e.*, the breakup of the ordered state into the chaotic one.

Turbulence arises in several settings, of which one of the most relevant is wall-bounded flows. The presence of a solid boundary in the flow domain causes the turbulent flow properties to be strongly heterogeneous and anisotropic. Near the walls, intense velocity gradients and fluctuations enhance momentum transfer, so that frequently low-speed fluid is ejected into the outer flow and conversely high-momentum fluid moves closer to the wall. Although the mean flow close to the wall can be determined statistically (at least at high Reynolds numbers), wall-bounded flows exhibit complex spatially and temporally coherent features. In particular, the inner flow is populated by a repetition of vortices and structures that actively contribute to the cyclic vertical motion of the fluid.

The properties of near-wall turbulence affect the dispersion and mixing of advected substances, or carried particles. In general turbulence greatly enhances dispersion, as the velocity fluctuations displace particles across the entire flow domain. In the case of wall-bounded flows, the heterogeneity of the flow field along the wall-normal direction makes so that also dispersion and mixing have a dependence on the wall distance. Furthermore, the aforementioned near-wall structures entrain the advected particles, possibly reducing dispersion (even if the local velocity fluctuations are high). The coherence inherent to particle motion in the near-wall region cannot be captured by looking at the local velocity statistics alone. Instead, a stronger understanding may be gained by shifting to a Lagrangian point of view and following the motion of advected particles, which sample the evolving flow field.

Finally, the transition to turbulence in the presence of walls exhibits two direction of heterogeneity (the one normal to the wall and the one along which turbulence develops). Moreover, the shift from a laminar flow to a turbulent one is coupled to the evolution of near-wall structures, which are the main driver of the transfer of energy from the mean flow to smaller scales. Indeed, through the analysis of the evolution of the coherent features of transitional wall-bounded flows, one may discern information regarding the spatial and temporal scales of turbulence, its driving factors and the influence on dispersing substances. The overall mechanisms that lead to turbulence and their interplay with wall-induced phenomena are not fully understood, and their study may provide deeper insight on the prediction and control of transition.

The above problems, namely the understanding of wall-bounded flows with particular regard to particle motion and transition, are the subject of the work contained in this thesis. This work is motivated by the paramount importance in practical applications of turbulence. A turbulent flow over a wing surface exerts more drag than a laminar one, causing an aircraft to spend more fuel. Conversely, turbulence enhances mixing and facilitates chemical reactions. Heat is removed from surfaces exposed from a flow faster if the flow is turbulent.

With regard to particle motion, we aim to characterize the dispersion of massless particles in a channel flow. The goal is to provide a detailed view on the dispersion of tracer particles, which is of course highly dependent on the wall distance at release. We also aim to correlate the features of dispersion to the local velocity field, in particular to near-wall structures. We do so at varying Reynolds number, in order to show the relevance of this parameter in dispersion problems. In the same channel flow setting, we study the mixing intensity of inertial particles, especially with respect to the interplay between local flow features and the inertia of particles.

Regarding transitional, wall-bounded flows, we focus on two main cases, namely flat plate boundary layer and channel flow. In the first case, we focus on the analysis of time-series with the goal to characterize them and ultimately to provide a simplified criteria to distinguish the turbulent regions from the non turbulent ones. In the latter, instead, we study the motion and shape of sets of particles, aiming to show the correlation between the particle features and the properties of the flow at varying scale.

Two main distinct efforts are needed in order to perform this kind of work. First, one needs to obtain data from turbulent and transitional flow fields. In this regard, both experiments and computer simulations are viable approaches.

Computer simulations provide unparalleled access to the flow data, as all flow variables are readily available across the entire domain. Still, care must be ensued to make sure that the simulations are well-resolved enough that the resulting data is physically correct. Experiments, instead, are by their own nature physically correct, although obtaining spatially extensive data from a turbulent flow field may prove difficult. This thesis fully revolves around data obtained from computer simulations.

Since the goal is the study of turbulence, no modelling assumption can be employed to reduce the computational burden. Instead, the entire flow field, including all the eddies up to the dissipation scales need to be properly resolved. The resulting approach is referred to as *direct numerical simulation* (DNS), as all small-scale features are directly simulated instead of modelled. The computational cost of this endeavour scales approximately as $\mathrm{Re}^{9/4}$ and quickly becomes prohibitive for relevant cases, even with current high performance computing systems. At the same time, relatively high Reynolds numbers are only achievable in simple geometries, such as rectangular channels and pipes.

Computational algorithms and computer codes need optimization and refinement in order to meet the demand for simulations at ever-increasing resolution. In this thesis, the current state of the art concerning the algorithms commonly used to simulated channel flow at high Reynolds number is presented. Additionally, the implementation of a new code, specifically designed for massively parallel computer architectures, is delineated.

The second effort required lies in perspective used to represent flow field data and its interpretation. Two complementary perspectives are commonly used to study fluid flows. The Eulerian one involves an observer which is fixed with respect to the reference frame of the domain. Instead, the Lagrangian perspective entails an observer which moves with the flow velocity and is thus advected by the fluid. Since it is somewhat easier to obtain fixed-point data from experiments and simulations alike, the Eulerian perspective is dominant in the study of turbulence. Nonetheless, the Lagrangian perspective arises naturally when mixing and dispersion phenomena are considered and is the most apt framework to study them.

Furthermore, particles advected by transitional and turbulent flows tend to exhibit a coherent organization which impacts on their overall dispersion and is closely related to the organized structures typical of these flows. In the most of the following work, we use the Lagrangian perspective to quantify the dispersion of particles and the presence of relevant patterns in their motion.

The interpretation is also critical to advance the understanding of turbulence. In some of the following work we use, as an interpretation framework, the application of graph theory to turbulent flows. Graphs are mathematical objects representing sets of interacting units, which provide measures to describe the interactions and their structure. With some care, it is possible to define graphs starting from flow data and use these graphs to obtain insight on the data itself. Of course, an approach that relies on defining an alternative representation of flow properties introduces some complexities. Indeed, in order to remedy to the added complexity of network-based methods, careful understanding of the relation between the flow data and the network defined over it must be ensured. One of the objectives of this thesis is to demonstrate that this effort is worthwhile because of the wealth of information that can be extracted using graph-based approaches.

This thesis is composed as follows. After this Introduction, Chapter 2 reviews the current understanding of turbulence, especially including the results obtained from Lagrangian approaches. Chapter 3 deals with the numerical simulation of turbulent and transitional flows, and in particular outlines the architecture of a new computer code designed for high Reynolds number channel flow. Chapter 4 introduces graph theory and reviews its application to fluid dynamics.

In Chapter 5, the trajectories of massless particles released in a turbulent channel flow is used to define a network which accounts for the wall-normal transfer of fluid. The effects of coherent patterns on particle motion and the influence of the Reynolds number are studied. Chapter 6 contains the analysis of mixing of inertial particles in a turbulent channel flow, highlighting the role of the Stokes number and its relation with the flow timescales. In Chapter 7 a network-based approach is used to study boundary layer transition, providing a method to locate the interface between turbulent and non turbulent regions of the flow domain. Chapter 8 considers the shape evolution of clouds of massless tracers in a transitional channel flow. The deformation of puffs is shown to be strongly scale-dependent and, in particular, is influenced by the incompleteness of the energy cascade in the transitional regime. Finally, Chapter 9 concludes this thesis and gives some final remarks on the results obtained and on future developments.

Chapter 2

Turbulence and transition

In this Chapter the problem of turbulence is introduced by a mathematical and physical standpoint, starting from its governing equations. Furthermore, transition to turbulence, *i.e.* the process which leads an ordered, yet unstable, fluid flow to an apparently chaotic one, will be examined.

2.1 Turbulence

In an incompressible fluid with constant density ρ, moving locally at a velocity $\mathbf{v}$ in a three-dimensional, Cartesian domain, both the mass and the momentum are conserved at any point in space and any time. The conservation laws can be expressed through the continuity and momentum equations, generally referred to as the Navier-Stokes equations

$$\nabla \cdot \mathbf{v} = 0, \tag{2.1}$$

$$\frac{\partial \mathbf{v}}{\partial \mathrm{t}} + \mathbf{v} \cdot \nabla \mathbf{v} = -\frac{\nabla p}{\rho} + \nu \Delta \mathbf{v} + \mathbf{f}, \tag{2.2}$$

with the appropriate boundary and initial conditions [166]. In equation 2.2, the pressure p is a scalar field chosen in order to satisfy the continuity equation 2.1, while ν is the kinematic viscosity of the fluid and $\mathbf{f}$ is a generic forcing. The solution of equations 2.1-2.2 is, in general, an extremely complex velocity field. Vortices of several scales, ranging from the largest permitted by the domain geometry to very small ones (bounded to the scale at which dissipation is dominant, *i.e.*, the Kolmogorov scale), evolve in an apparently unpredictable manner. The pseudo-chaotic behaviour of the velocity field and the absence of a stable, stationary flow configuration are the defining feature of turbulence.

The momentum equation outlines two competing phenomena, whose combination is the root for the phenomenological appearance of turbulence. The first is dissipation, that is the tendency of sharp gradients to become smoother as time passes. Dissipation is proportional to the Laplacian of the velocity $\Delta\mathbf{v}$ and to the viscosity ν. On the other hand, the convective term $\mathbf{v} \cdot \nabla \mathbf{v}$ is tightly linked to the acceleration of the flow and rules the transfer of energy between vortices of different scales.

The balance between dissipation and convection is determined by the combination of the flow speed, the typical length scale of the domain and the viscosity. Non-dimensional variables can be introduced by selecting the velocity and length scales U and L, appropriate to the flow under consideration. By defining the non-dimensional velocity $\mathbf{v}^\star = \mathbf{v}/U$ and the non-dimensional length $l^\star = l/L$ and omitting volumetric forcing, the Navier-Stokes equations 2.1-2.2 become

$$\nabla \cdot \mathbf{v}^\star = 0, \tag{2.3}$$

$$\frac{\partial \mathbf{v}^\star}{\partial \mathrm{t}} + \mathbf{v}^\star \cdot \nabla \mathbf{v}^\star = -\nabla p^\star + \frac{\nu}{UL} \Delta \mathbf{v}^\star, \tag{2.4}$$

where the pressure $p^\star$ has been normalized using ρU^2 and all differential operators are non-dimensional as well. In equation 2.4, UL/ν is the Reynolds number Re, which defines the ratio between inertial and viscous forces. In the following, the * apex will be dropped when indicating non-dimensional variables.

In the case of very low Reynolds number, the case of *creeping flow* arises, which is time-reversible and non-chaotic. At small Reynolds numbers the flow appears ordered and characterized by the layered motion of fluid particles, which is the case of *laminar motion*. Laminar flows are usually characterized by lower momentum and energy transfer. This thesis instead deals with cases in which the Reynolds number is generally high, such that inertial forces prevail at almost all scales, or at least high enough that the flow eventually becomes turbulent. While at large scales the convective term has a dominant effect and ensues the transfer of energy between flow scales, at small scales the Laplacian of the velocity becomes large enough due to small-scale gradients that the term $\Delta \mathbf{v}^\star/\mathrm{Re}$ becomes non-negligible, leading to dissipation.

Because of these phenomena, the scale-dependent nature of turbulent fluid motion emerges. Energy, coming from external forcing such as gravity or other work sources, is transferred from the larger scales to the smaller, up to the point where dissipation is dominant and no further energy transfer takes place. This process is usually described as the *energy cascade* and is the fundamental tenet of the current understanding of turbulence. As the Reynolds number grows, the separation between the large, energy-injecting scales and the small dissipating scales grows.

One may assume that at the smallest scales of the flow no influence of the larger scales is present and, rather, only the rate at which energy is transferred and the viscosity ν are important. This assumption leads to Kolmogorov's theory [69, 147], which provides the most important framework currently used for the statistical study of turbulence. When the separation between the large, forcing scales and the dissipation scale is large enough, a range of scales appears, in which the effects of both dissipation and external forcing are not relevant. In this *inertial range* only the turbulent kinetic energy dissipation rate ϵ, that is the transfer rate of energy from large to small scales, is relevant.

The analysis of fluid flows can be performed through a variety of approaches, which vary in resolution and versatility. Experiments resolve naturally all flow scales and provide a truthful representation of turbulence, but the possibility of measuring the entire flow field is limited and care is needed to isolate the phenomena of interests. Computer simulations, instead, allow unparalleled access to spatiotemporal data. On the other hand, they must be executed with accuracy in order to represent the complex spatiotemporal behaviour of the flow. In industrial settings methods of simulation based on the statistical stationariety of a flow (Reynolds Averaged Navier Stokes, RANS) or on the filtering of the small velocity scales (Large Eddy Simulation, LES) are widely used, due to their simplicity and the reduced computational burden [229, 161]. Still, due to the need of closure models for turbulence which are empirical and often of lacking precision in the most complex flow cases, their use is not possible for the study of turbulence. Instead, one must resort to the simulation of all scales of motion within a flow, without the need for closure models, to obtain an accurate depiction of turbulence. This approach, termed Direct Numerical Simulation (DNS), is limited to moderate Reynolds numbers (due to the growing separation between scales and, thus, the need for larger resolutions) and simplified geometries [134]. An important class of flows that are simulated by means of DNS is that of wall-bounded flows, *i.e.* flows in a domain which has at least one solid boundary.

2.1.1 Wall-bounded flows

Whenever a solid boundary S is present at the frontier of the flow domain, a no-slip boundary condition arises, *i.e.*

$$\mathbf{v}(\mathbf{x}) = 0, \forall \mathbf{x} \in S. \tag{2.5}$$

The combination of the zero velocity at the boundary and of the nonzero velocity away from the boundary gives rise to a junction region, the *boundary layer*. Notable examples include pipe (Poiseuille) flow, channel flow and boundary layer (Blasius) flow [98]. All these cases are characterized by the presence of shear, *i.e.* a wall-normal velocity gradient. Its intensity per unit of surface at the wall, the wall shear stress τ_w, is of great importance. From the wall shear stress, a reference velocity can be defined as $u_\tau = \sqrt{\tau_w/\rho}$, that is, the *friction velocity*. By using the friction velocity and a relevant dimension of the flow (the pipe radius R, the channel half-height δ, or the boundary layer thickness), one can normalize the Navier-Stokes equations and define a *friction Reynolds number* $\mathrm{Re}_\tau = u_\tau \delta/\nu$, which is a measure of the separation between the largest scales of the flow (of size δ) and the small near-wall features (of size ν/u_τ). By using the reference scale of the near wall features u_τ and $l_w = \nu/u_\tau$, an *inner* normalization can be defined by introducing a non-dimensional velocity $\mathbf{v}^+ = \mathbf{v}/u_\tau$ and a non-dimensional length $\mathbf{x}^+ = \mathbf{x}/l_w$.

The most relevant result in the study of wall-bounded turbulence is that the mean velocity U^+ (which is nonzero only in the axial/streamwise direction) is uniquely determined by the distance from the wall y^+, at least for very large Reynolds numbers Re_τ and sufficiently close to the wall. In particular, very close to the wall the velocity grows linearly, *i.e.*

$$U^+(y^+) = y^+, \quad y^+ < 5 \tag{2.6}$$

while slightly away from the wall a logarithmic law is found

$$U^+(y^+) = \frac{1}{k} \log y^+ + B, \quad 30 < y^+ < 0.2\delta^+ \tag{2.7}$$

where $k \approx 0.4$ is the Von Kármán constant, which is universal [124]. Figure 2.1 show the mean velocity profile in a numerically simulated channel flow at $\mathrm{Re}_\tau = 180$, along with the standard deviation of the three velocity components (that are, instead, dependent also on the Reynolds number).

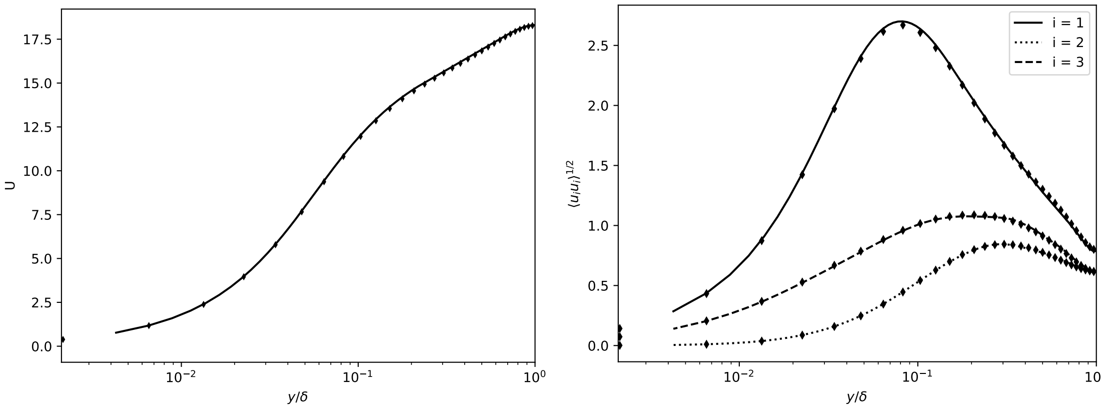

(a) Mean velocity

(b) Standard deviation

Figure 2.1: Statistical moments of the velocity in channel flow at $\mathrm{Re}_\tau = 180$, DNS data from [217]

Given that the spatial extension of the logarithmic region is limited by the Reynolds number, only simulations and experiments conducted at high Reynolds number exhibit the presence of a log layer which is sufficiently large to allow an accurate measurement of the Von Kármán constant. Recent numerical results show the presence of a logarithmic layer up to $y^+ = 2500$ at $\mathrm{Re}_\tau = 10000$ [85].

Coherent patterns in wall turbulence

While turbulence is mostly chaotic, the velocity fields of a turbulent flow do not appear entirely composed of pseudo-random fluctuations with no organized pattern. Instead, the birth, growth and disappearance of localized features can be observed. These features are usually constituted by a portion of the fluid which moves coherently. Furthermore, such patterns, usually termed *coherent structures*, repeat themselves with similar features at different times and positions in the flow.

An important class of coherent structures found in wall-bounded flows is that of wall structures, that is the set of patterns usually found very close to the wall. In particular, the region where y^+ is less than about 60, which is also characterized by the most intense velocity fluctuations, is home to quasi-streamwise vortices. These vortices, which are slightly misaligned with the streamwise direction and are also pointing upwards, are the fundamental constituents of near-wall turbulence [97]. Their vortical behaviour entraps high-momentum fluid from the outer flow and brings it closer to the wall, while also ejecting lower speed fluid into the outer flow. The combined action of these two processes, called *sweeps* and *ejections*, determines the appearance of streamwise streaks with high and low streamwise velocity. In turn, it is the instability of these streaks that generates the quasi-streamwise vortices in a self-sustaining process, *i.e.* the *near wall cycle* [99]. This process sustains wall-turbulence, albeit it is interesting to note that numerical evidence indicates that the sole role of the wall is that of causing shear, which is instead the main actor behind the energy transfer taking place. Streamwise streaks are shown in figure 2.2 using data from a numerically simulated channel flow. It can be noted that their length is comparable or even larger than the channel size $\delta = 1$. Other interesting structures appear near the wall, such as the horseshoe vortices that arise from the union of two, counter-rotating, streamwise vortices [7]. Common methods used for the identification of coherent structures rely on the computation of indicator functions obtained from the local strain rate of the flow, such as the λ_2 and the Q criteria [232].

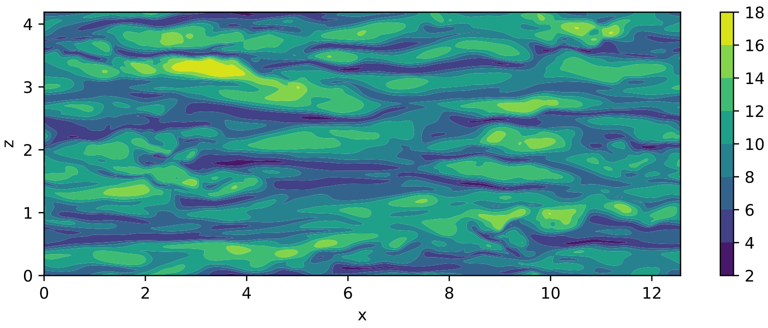

Figure 2.2: Streamwise velocity u at a wall-normal coordinate $y^+ = 10$ in a numerically simulated channel flow at $\mathrm{Re}_\tau = 180$. The simulation domain has a size $L_x \times L_y \times L_z = 4\pi\delta \times 2\delta \times 4\pi\delta/3$, where δ is the channel half-height.

2.2 Transition to turbulence

While a sufficiently high Reynolds number is a necessary condition for the onset and sustainment of turbulence, it is in general not sufficient. Indeed, an unperturbed laminar (*i.e.*, ordered) solution of the Navier-Stokes equation could theoretically last indefinitely. In reality, as was first shown by the experiments of Reynolds for pipe flow, for each flow case there exists a *critical* Reynolds number above which the flow is turbulent, while below that number the flow exhibits turbulence in a temporally and/or spatially localized manner, a behaviour known as *intermittency* [168, 56]. In experiments, small, but finite, perturbations are inserted into the flow by the wall roughness, external vibrations of the experimental apparatus and so on. These finite perturbations cause the transition to turbulence. Of course, if the Reynolds number is sufficiently small, the flow remains laminar independently of the intensity of perturbations. The transition from a laminar state to a turbulent one is in general characterized by the linear growth of perturbation, their subsequent nonlinear interactions with the base laminar flow and together with themselves, their breakdown and the final onset of fully developed turbulence.

While the growth of finite perturbations involves nonlinear interactions between flow modes, whether or not perturbations of infinitesimal amplitude lead to turbulence may be determined by means of linear stability analysis. For the case of plane channel flow with walls at $y = \pm 1$ the laminar base flow is $U(y) = U_c(1-y^2)$ for the streamwise component and zero for the wall-normal and spanwise ones. Assuming a two-dimensional perturbation of the wall-normal velocity of the kind

$$v' = \hat{v}' \mathrm{e}^{i(\alpha x - \omega t)}, \tag{2.8}$$

The wall-normal projection of the momentum equation 2.2 reduces to

$$\frac{\mathrm{d}^4 \hat{v}'}{\mathrm{d}y^4} - 2\alpha^2 \frac{\mathrm{d}^2 \hat{v}'}{\mathrm{d}y^2} - i(\alpha - \omega)\mathrm{Re}_c \left[U(y) \left(\frac{\mathrm{d}^2 \hat{v}'}{\mathrm{d}y^2} - \alpha^2 \hat{v}' \right) - \frac{\mathrm{d}^2 U(y)}{\mathrm{d}y^2} \right] = 0, \tag{2.9}$$

which is the Orr-Sommerfeld equation and can be solved as an eigenvalue problem for ω and the associate eigenfunction $\hat{v}'$ [151, 196]. Numerical solution of the equation 2.9 in the case of plane channel flow shows that an unstable mode (with $\mathrm{Re}(\omega) > 0$) arises when the centerline Reynolds number is larger than $\mathrm{Re}_c = 5772$ [152].

It is notable to recall that not all flows undergo linear instability. In particular, pipe flow and plane Couette flow are linearly stable at all Reynolds numbers, *i.e.*, there exists a sufficiently small perturbation that does not trigger transition at any value of the Reynolds number. Indeed, experiments have achieved laminar pipe flow at Reynolds numbers up to 100000 by thoroughly controlling the experimental setup [160]. Nonetheless, after a certain point the perturbations must be so small for the flow to remain laminar that turbulence arises due to the nonlinear amplification of the disturbances [4, 5].

In channel flow the wave-like perturbation, which is the most unstable solution of the Orr-Sommerfeld equation and is generally referred to as the *Tollmien-Schichtling wave*, grows at first linearly, after which it starts interacting nonlinearly with the base flow, giving rise to Λ-shaped vortices. These vortices quite rapidly stretch and breakup into smaller structures, initiating the transfer of energy to smaller scales which is the onset of turbulence. Once this is complete, fully developed turbulent flow is achieved. This route to turbulence is known as Klebanoff-type transition [6]. The entire phase spanning from the end of the linear growth of small-amplitude perturbations up to fully developed turbulence is characterized by velocity fields with strong velocity fluctuations and, in general, strong spatio-temporal complexity. The appearance and, also, the disappearance of localized turbulent spots makes so that the border between non-turbulent and turbulent flows is of difficult investigation.

The development of finite amplitude flow structures and, subsequently, turbulence during transition can be interpreted as the advancement of the solution of the Navier-Stokes equations in a state space towards, eventually, some kind of *attractor*. While there is no deterministic asymptotic state, the statistical convergence of turbulent flows has been associated with the notion of a strange attractor [117]. Numerical simulations have shown that intermittent motion in the transitional regime is often associated with invariant (*i.e.*, traveling wave) solutions of the Navier-Stokes equations, termed *exact coherent states* [112]. The transitional flow exhibits a state-space dynamics that revolves around these coherent states, which act as attractors for the recurrent behaviour of the flow [103, 156]. Turbulent and intermittent states can eventually decay into laminar flow, with appropriate timescale depending on the Reynolds number [178]. In channel flow at low Reynolds numbers, typical intermittent patterns include bands tilted rather than aligned with the streamwise direction, which may split into smaller bands or decay entirely to laminar flow [76].

The growth and subsequent breakup of the structures found in Klebanoff-type transition, such as the roll up of Λ-vortices and the formation of hairpin-like structures, form the prototype of the typical features found in wall-bounded turbulence [177, 167, 125]. In this sense, late stage transition already contains all the essential features of turbulence and is a setting in which turbulence itself can be studied in an elementary form.

Klebanoff-type transition is not the only pathway to turbulence in wall-bounded flows. Another mechanism arises when some factor external to the boundary layer, such as turbulence in the free stream of the flow around a flat plate, exerts a vertical forcing on the boundary layer and triggers the transition. This route to turbulence, which circumvents the usual (and slow) growth of perturbations, is known as *bypass* transition [230]. The mechanisms composing bypass transition are roughly as follows. First, the perturbation in the free stream, which may be even developed turbulence, generate large-scale perturbations of the streamwise velocity (that is, streaks) in the laminar boundary layer. While free stream turbulence has a broadband nature, because of a process known as *shear sheltering* in the boundary layer only low frequency perturbations appear [96]. The boundary layer acts as a low-pass filter for external perturbation because of the presence of mean shear, which makes so that the effect of high-frequency perturbations are cancelled out. Streaks, after their appearance, are lifted towards the edge of the boundary layer by the action of the high-frequency components of the perturbation in the free stream [231, 188]. This ultimately causes their secondary instability, the formation of spots and, ultimately, bypass transition to turbulence.

While in the case of orderly transition the largest influence on the criticality of the flow is taken by the Reynolds number, in the case of bypass transition the matter is complicated by the chaotic behaviour and the variety of the free stream forcing, so that the onset of turbulence may also depend on other factors such as the turbulent intensity [20]. Several factors appear to influence the onset of bypass transition, such as the system geometry, the external flow conditions (especially the pressure gradient, which is stabilizing if aligned with the flow and destabilizing if adverse) and the wall roughness in experimental setups.

The physical and industrial applications associated with the appearance of turbulence motivates the study of transition to turbulence. The increased momentum transfer linked to turbulent velocity fluctuations causes a strong increase in wall friction and, thus, drag. Given the importance of drag reduction, significant efforts have been made with the objective of predicting, controlling and delaying the onset of turbulence [19, 55, 68, 84]. Another problem tightly linked with the prediction of transition is that of the determination of the spatial and temporal location of the turbulent-non-turbulent interface, which mostly relies on the fact that certain flow quantities have different values in turbulent and laminar regimes [42, 28]. The problem is further complicated by the complex, almost fractal, shape of the interface and its time-dependence. Accordingly, the definition of an appropriate indicator function and of a threshold should, in theory, suffice to distinguish laminar and turbulent regions. Several of these indicator functions have been proposed. As vorticity is perhaps the most striking and peculiar feature of turbulence, its use as an indicator function should be straightforward. Unfortunately, in the most general cases where turbulence is also present in the free stream and also due to the vorticity associated with mean shear, the usefulness of the measurement of the vorticity does not provide clear information on the distinction between laminar and turbulent regions of the domain. The intense velocity fluctuations associated with transitional flow lead to the choice of functions of the velocity as indicator. A common choice in boundary layers is the sum of the wall-normal and spanwise velocity fluctuations $|v'| + |w'|$. With extensive knowledge of the flow field, data processing techniques can be used to compute an interface location depending on time. A widely used technique is Otsu's method, which is an image segmentation technique that identifies the optimal threshold of a scalar value (in boundary layers,

$|v'| + |w'|)$ [153]. In particular, the method achieves the objective of minimizing the *intra-class* variance within the turbulent and the laminar regions, and does so by maximizing the *inter-class* variance between the laminar and turbulent regions. Because of the dependence on y of the wall-normal velocity fluctuations, a global (y-independent) threshold cannot be provided and Otsu's procedure has to be applied to isolated vertical slices of the boundary layer flow [143]. The dependence on the wall-distance of the segmentation parameters makes the choice of a threshold problematic and the wide application of the method difficult.

2.3 Lagrangian turbulence

The observation of fluid motion can be carried out according to different paradigms. In contrast with the Eulerian perspective, which relies on an observer fixed with respect to some reference frame, the Lagrangian approach relies on an observer that is carried by the fluid and moves at its velocity at any point and time. The balance of forces acting on an infinitesimal fluid particle carried by the flow is

$$\frac{\mathrm{D}\mathbf{v}}{\mathrm{Dt}} = -\frac{\nabla p}{\rho} + \nu \Delta \mathbf{v} + \mathbf{f}, \tag{2.10}$$

which is the Navier-Stokes momentum equation in Lagrangian form. Equation 2.10 is a straightforward rewriting of Newton's second law. The equivalence with the Eulerian form 2.2 is evident by the definition of the *material derivative* D/Dt

$$\frac{\mathrm{D}f}{\mathrm{Dt}} = \frac{\partial f}{\partial \mathrm{t}} + \mathbf{v} \cdot \nabla f, \tag{2.11}$$

which combines the temporal and convective terms; the latter in particular represents the change of f experienced by the Lagrangian observer when moving through a non-homogeneous field advected by the velocity $\mathbf{v}$.

The Lagrangian perspective arises naturally in the study of mixing and dispersion of quantities advected by the fluid, which are strongly enhanced by turbulence [226, 199, 142]. The most elementary form in which dispersion can be studied is through the analysis of trajectories $\mathbf{X}(\mathbf{x}_0, t)$ of massless particles, *i.e.* tracers, that are equivalent to the infinitesimal fluid particles. Diffusing species can be modeled by tracers given that they are passive, *i.e.*, their motion and concentration do not exert feedback on the carrier flow, their response time is infinitesimal with respect to the typical timescale of the flow, and their own molecular diffusion is negligible with respect to turbulent dispersion.

The prime setting for Lagrangian studies of turbulence is that of computer simulations. Indeed, numerical simulations allow the integration of trajectories of truly massless particles, while in experiments one needs to seed the flow with tracer-like particles which will inevitably have some sampling issues due to finite inertia [213].

Of course, simulations are limited by the available computational power. The very first studies of Lagrangian tracers were concerned with the analysis of single particle statistics in homogeneous isotropic turbulence, while only later two-particle analyses were conducted [225, 184, 22]. In general, the particle trajectories are obtained by integrating the Eulerian velocity field along the path of particles and starting from the release location $\mathbf{x}_0$, *i.e.*,

$$\frac{\partial \mathbf{X}(\mathbf{x}_0, t)}{\partial t} = \mathbf{v}(\mathbf{X}(\mathbf{x_0}, \mathbf{t}), \mathbf{t}) \tag{2.12}$$

which indicates how the velocity at the position of particles is used to compute their own (Lagrangian) velocity.

2.3.1 Single-particle statistics

Several relevant problems emerge regarding the Lagrangian properties of turbulence. While direct numerical simulations allow the exact computation of particle trajectories, lower order methods of flow simulation, due to the missing small scales, need stochastic models to accurately represent particle dispersion [165, 222, 111]. The prime example of such models is the Langevin equation, which models the acceleration as a Markov process [34, 33]. These models rely especially on the correlations of the velocity and acceleration correlations of Lagrangian tracers, whose knowledge is extensively needed for accuracy especially in complex flows. Moreover, distributions of Lagrangian accelerations exhibit strong intermittency in the form of long tails due to extreme events. The Lagrangian velocity autocorrelation is defined as

$$\rho_{ij}(\tau, \mathbf{x}_0) = \frac{\langle v_i'(t_0, \mathbf{x}_0) v_j'(t_0, \mathbf{x}_0)\rangle}{\langle v_i'^2(t_0, \mathbf{x}_0)\rangle \langle v_j'^2(t_0 + \tau, \mathbf{x}_0)\rangle}, \tag{2.13}$$

where $\langle \cdot \rangle$ is an ensemble mean over particles with the same release location $\mathbf{x}_0$, τ is the delay over which the autocorrelation is computed and v_i' is the i-th component of the velocity fluctuation. Significant information can be extracted from the correlation function $\rho_{ij}(\tau, \mathbf{x}_0)$ in the form of its integral

$$T_{L,ij}(\mathbf{x}_0) = \int_0^{+\infty} \rho_{ij}(\tau, \mathbf{x}_0) \mathrm{d}\tau, \tag{2.14}$$

which is the Lagrangian integral timescale. The integral timescale provides a measure of the typical times of particle motion. At times much shorter than T_L, the behaviour of particles is almost entirely ruled by their initial velocity, because the velocity shortly after t_0 is strongly correlated to $v(t_0)$. In this *ballistic* regime, the variance of particle position grows as fast as t^2. For very long times, Taylor's prediction of dispersion linear in time is instead recovered [210].

Numerical studies of Lagrangian correlations have been carried out in homogeneous isotropic turbulence, where the release coordinate and the direction are irrelevant and cross-correlations are zero [228, 227, 198]. In more complex setting, the cross-correlations cannot be ignored and their value must be considered when formulating models. Given the industrial importance of wall-bounded flows, direct simulations of Lagrangian tracers in such settings are needed to correctly inform modeling. Several basic results can be achieved through dimensional considerations akin to Kolmogorov's scaling laws [148, 63]. Lagrangian studies of tracers have been carried out in channel and shear flows at low Reynolds number, investigating velocity and acceleration correlations and statistics [219, 133, 44, 149, 47, 208]. Other setups of particular interest for geophysical flows have been investigated as well by means of direct numerical simulation, albeit more scarcely [36, 127]. Simulations at larger Reynolds numbers have been carried out; [111] reached $\mathrm{Re}_\tau = 950$, while later $\mathrm{Re}_\tau = 1440$ was achieved [200, 94]. Still, these values reach only moderate levels of scale separation and lag behind both the typical industrial cases and the Reynolds numbers reached in channel flow simulations for Eulerian measurements [85].

2.3.2 Multiparticle statistics

Other than the characterization of the properties of single particles, the most relevant aspects of Lagrangian turbulence is the study of the behaviour of groups of particles. This problem emerges in a straightforward manner from several industrial and geophysical applications, such as the dispersion of pollutant from a plume in the atmosphere or industrial mixing problems. In its simplest form, the problem of multiparticle dispersion reduces to the study of the mutual distance of a pair of particles, whose initial distance is $\mathbf{r}_0$, with respect to the time from release [183, 176].

Richardson was the first to recognize the role of a continuum of flow scales, *i.e.*, the turbulent eddies, in determining pair dispersion and the distribution of distances in a particle cloud from its center of mass [169]. The application of Kolmogorov's similarity theory to pair dispersion led to the development of the fundamental framework of Batchelor [15, 12, 13, 14]. At very short times, the pair separation is ruled by the velocity differences, that is the Eulerian velocity structure function. In homogeneous and isotropic turbulence, Batchelor obtained that the mean square separation of a pair of particles $r(t)$ (which is scalar because direction is not relevant due to isotropy), follows the ballistic regime

$$\langle r^2(t)\rangle - r_0^2 \approx \left[D_{LL}(r_0) + 2D_{NN}(r_0)\right] t^2, \tag{2.15}$$

where D_{LL} and D_{NN} are the longitudinal and transverse structure functions, respectively. The most important results are achieved when r_0 is in the inertial range, where Kolmogorov's theory yields an exact prediction for the structure functions and equation 2.15 reduces to

$$\langle r^2(t)\rangle - r_0^2 \approx \frac{11}{3} C \left(\epsilon r_0\right)^{2/3} t^2, \tag{2.16}$$

with C and ϵ being a universal constant and the local turbulent dissipation rate, respectively. After this short time, the initial separation and the time are in the inertial range Eulerian velocity differences are not relevant anymore. From dimensional considerations it is obtained that mean square separation of particles grows superdiffusively as

$$\langle r^2(t)\rangle - r_0^2 \approx g\epsilon t^3, \tag{2.17}$$

where g is the universal, *Richardson* constant. The crossover between the ballistic regime and Richardson scaling takes place at a time of order $\sqrt[3]{r_0^2/\epsilon}$.

Although Richardson scaling has been observed in two-dimensional flows, its appearance in full, three-dimensional, homogeneous and isotropic simulations has proven elusive [101, 35, 206]. Indeed, equation 2.17 is based on the assumption that only eddies at the scale r contribute to dispersion. Recent studies have challenged the validity of this assumption, providing evidence that dispersion is influenced by the whole continuum of flow scales up to r and that the presence of coherent flow features cannot be ignored [58].

The analysis of features of pair separation provides an insight on both dispersion processes and the underlying turbulence. As an example, pair dispersion exhibits temporal asymmetry, *i.e.* particle pairs disperse faster backward in time than forward. This behaviour has been linked to the irreversibility of the energy cascade in turbulent flows [100, 30].

The study of multiparticle structures has focused mainly on tetrahedra, but also on more complex puffs. In all cases, the shape evolution has been studied by means of invariant measures of multiparticle sets, such as the eigenvalues of the position covariance matrix [23, 21, 79, 131]. Finally, the study of the deformation of material structures in turbulence leads naturally to the finding that certain sets of fluid particles exhibit coherence in time. These sets, which widely influence the overall flow dynamics, are termed *Lagrangian coherent structures* [81]. Notable approaches to this regard include the study of finite time Lyapunov exponents, which maps itself nicely with pair and multiparticle dispersion, and the search of invariant sets.

In wall-bounded flows, the matter is further complicated by the relevance of the initial alignment of pairs of particles or multiparticle structures with respect to the flow reference system. Most notably, the relative dispersion of pairs that are aligned transversely to the mean shear direction is greatly increased. Few studies have focused on multiparticle statistics in the context of non-uniform flows, also because the large amount of parameters that need to be considered for a thorough analysis [162, 163]

2.3.3 Inertial particles

Tracer particles are a representation of the Lagrangian fluid particle, *i.e.* an inertialess object that is perfectly carried from the flow. Real particles instead have finite inertia and do not react instantly to velocity changes of the carrier flow. In particular, the characteristic response time of particles meeting two conditions, namely a very low Reynolds number

$$\mathrm{Re}_p = \frac{d_p||\mathbf{u}_p - \mathbf{v}||}{\nu}, \tag{2.18}$$

where d_p and $\mathbf{u}_p$ are the particle diameter and velocity, and small size with respect to the smallest flow scales, can be computed with the Stokesian assumption

$$\tau_p = \frac{d_p^2 \rho_p}{18\nu}, \tag{2.19}$$

with ρ_p being the particle density. The ratio between the particle characteristic time and the smallest local timescale τ_K (that is, the Kolmogorov time) is the Stokes number

$$\mathrm{St}_K = \frac{\tau_p}{\tau_K} \tag{2.20}$$

and defines the regime of motion of the inertial particle. At low Stokes numbers (much smaller than unity) particles are akin to tracers, so that they follow quite closely the flow velocity. At very large Stokes numbers instead, particles behave ballistically (*i.e.*, their behaviour is mostly determined by their initial velocity) and react weakly to the local velocity fluctuations.

Most interestingly, when the particle timescale matches that of the flow (*i.e.*, $\mathrm{St}_K = \mathcal{O}(1)$, the synchronization between the motion of eddies and that of particles leads to highly intermittent particle concentration and thus the appearance of clusters that are located away from vortex cores. The so-called *inertial clustering* is therefore one of the most remarkable phenomena concerning inertial particles, owing also to the difficulty incurred when trying to predict the spatial and temporal features of clusters and the causes and whereabouts of their formation [136, 31, 154, 181, 17, 60, 175].

Proposed mechanisms for the formation of clusters take into account, among others, the local fluid acceleration and the strain rate [77, 43]. Notably, while peak clustering is in general achieved when the particle timescale matches that of the smallest scales of the flow, in high Reynolds number turbulence also larger clusters are formed by the matching of the particle timescale with the typical times of the inertial scale [150, 29]. Cluster have sizes similar to those of the flow scales that contribute to their formation and are similarly short-lived, continuously dissolving and recombining in an endless process [121].

The appearance of segregation and clustering phenomena has a significant dependence on both particle properties and flow conditions. Important parameters to this regard include the density of particles, that may be denser or lighter than the carrier fluid, the presence or less of gravity and the concentration of particles [16, 157, 64, 18, 216, 37]. Especially regarding concentration, while when particles are dilute their back-force on the fluid (due to Newton's third law) has a negligible effect on the overall turbulence statistics, at larger concentrations a *two-way coupling* regime arises, where the presence of particles has a non-negligible effect on the carrier flow [218]. If the volumetric concentration is even larger, also collisions between particles become relevant (the so-called *four-way coupling*) [65].

The analysis of clusters itself is complicated by the need of accurately characterizing particle distributions. The acceleration statistics of inertial particles highlight the impact of inertia on the dampening of velocity fluctuations [126]. Radial distribution functions exhibit self-similarity in presence of inertial clustering and reveal information about the overall organization of clusters, but neglect most of their spatial complexity [109, 82]. Other methods include box-counting, Voronoi tessellations and wavelet filters [171, 11, 135]. Overall, the quantitative identification of clusters rely on the choice of thresholds, which may be prone to arbitrariness, although it is possible to define methods that are insensitive to the choice of threshold in a certain range.

While the properties of inertial particles are already subject to a range of complexities in homogeneous turbulence, their behaviour in wall-bounded flows presents further complications [78]. Inertial particles tend to migrate away from regions where turbulence is the most intense. Accordingly, they accumulate at the walls (even in the absence of gravity) experiencing a phenomenon called *turbophoresis* [132, 108, 110, 32, 179, 137]. The resulting high concentration of particles at the wall makes the simulation of particle-laden flows for long times challenging, as even in the case of low overall concentrations one cannot escape accounting for the back reaction of particles on the near-wall flow and mutual collisions in order to accurately integrate trajectories.

The typical features of near-wall turbulence, in particular sweeps and ejections, move particles towards the wall and back into the outer flow, but the inertia of particles coupled with their low velocity at the wall makes so that only ejecting motions with sufficient spatial coherence are effective in lifting particles away from the wall [128, 66]. Particles instead become concentrated into very elongated (longer than δ) streamwise-aligned streaks associated with negative velocity fluctuations. Moreover, flow scales are dependent on the distance from the wall, which causes clusters to form at different values of particle inertia across the wall. Indeed, a new Stokes number can be defined using the timescale derived from the friction velocity, *i.e.*, $\mathrm{St}^+ = \tau_p^+ = \mathrm{St}_K \tau_\eta^+$, which is constant for particles with fixed diameter and density. The Stokes number St_K, instead, is not constant and is proportional to τ_η^+, which takes a small value at the wall and grows monotonically away from it.

2.4 Open questions

Let us briefly review the open problems in the current understanding of fluid physics that will be tackled in this thesis. Single particles statistics and simple multiparticle structures (such as pairs) have been extensively studies (although, in general, a characterization at higher Reynolds number would be beneficial). Instead, the collective behaviour of large numbers of dispersing particles has not been studied in depth, especially in wall-bounded geometries. We refer in particular to mixing of particles which are initially orderly distributed and transition to a fully mixed state. Although some general predictions can be made about their motion both shortly after release and after long times, the intermediate regime is of difficult characterization and is also the most interesting, due to it being the time at which the effects of local turbulence are the most relevant. The work concerning the dispersion of particles in turbulent channel flow is found in chapter 5.

Another area of interest regarding dispersion and mixing in turbulent flows is that of non-tracer particles. Mixing of heavy particles in non-homogeneous geometry is influenced by inertial clustering, although a quantification is made difficult in channel flows due to the presence of different phenomena depending on wall distance (turbophoresis close to the walls, isotropic clustering at the center of the channel). Accordingly, we introduce a measure of mixing and apply it to a large set of inertial particles, reporting the results in chapter 6.

Of the many issues currently affecting the current understanding of transitional flows, the ones that will be the subject of parts of this thesis are the identification of the turbulent-non turbulent interface and the behaviour of particle puffs advected by non fully developed flows. The former problem is deeply related to the classification of flow field data and was chosen to showcase the properties and the effectiveness of a data analysis technique based on graphs. Indeed, the identification of turbulence based on simple thresholds remains difficult. The latter, instead, represents a continuation of the work on multiparticle structures, which is even rarer in the setting of transitional flows. Multiple questions are addressed in this work. Of course, the behaviour of such structures in a flow that is evolving from an orderly state to a chaotic one is described in depth. Moreover, multiparticle structures are known to behave according to their scale, but a full characterization of this dependence is lacking. Accordingly, we aim to study puffs of different sizes at release. The benefit of doing so in a transitional flow is that, being the energy distributed differently across scales in intermittent and fully developed flow, also the deformation of puffs will be different. The study of puffs can then be related to the incompleteness of the energy cascade and to the amount of intermittency present. These two problems are tackled in chapters 7 and 8

Chapter 3

Direct numerical simulation of channel flow and particle tracking

In this Chapter, the methods used for performing a direct numerical simulation of a turbulent channel flow will be outlined. First, the treatment of the Navier-Stokes equations, the spatial and temporal discretization and the initial and boundary conditions will be described. After that, details on the implementation of a parallel computer code will be given. Finally, the tracking of Lagrangian particles in a numerically simulated flow will be briefly discussed.

3.1 Equations and discretization

3.1.1 Problem formulation

Channel flow is the most basic wall-bounded flow configuration. The idealized setup comprises of two infinite, parallel walls put at a distance of 2δ from each other, in the midst of which a fluid with density ρ and viscosity ν flows. The fluid motion is driven by a mean pressure gradient or, equivalently, a homogeneous bulk volume force, which is oriented along the streamwise direction x. Accordingly, a mean flow appears, with the only nonzero component being U. In the wall-normal y and spanwise z directions, the mean flow is zero, *i.e.*, $V = W = 0$. Instead of solving for an infinite domain, one transforms the domain into a torus by setting periodic boundary conditions along x and z and defining a streamwise and spanwise length, l_x and l_z, of the domain. This configuration is shown in figure 3.1.

The problem is thus to obtain a solution of the Navier-Stokes equations made

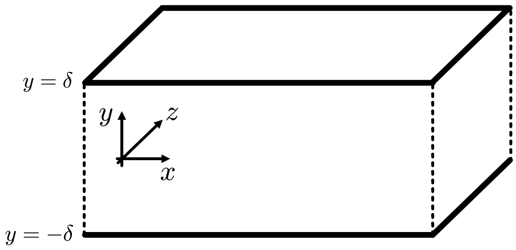

Figure 3.1: Schematic of the channel flow domain

non-dimensional using the friction velocity u_τ, the viscosity ν and the channel half-height δ, that is

$$\nabla \cdot \mathbf{v} = 0, \tag{3.1}$$

$$\frac{\partial \mathbf{v}}{\partial \mathrm{t}} = -\frac{\nabla P}{\rho} - \boldsymbol{\omega} \times \mathbf{u} + \frac{1}{\mathrm{Re}_\tau} \Delta \mathbf{v} + \mathbf{f}. \tag{3.2}$$

Equations 3.1-3.2 are the rotation form of equations 2.1-2.2, obtained through vector identities. $\boldsymbol{\omega} = \nabla \times \mathbf{v}$ is the vorticity vector. $P = p + \rho \mathbf{v} \cdot \mathbf{v}/2$ is the total pressure and $\mathbf{f}$ is the constant bulk force driving streamwise mean motion. The boundary conditions are periodic along the streamwise and spanwise directions, while the no-slip condition $\mathbf{v} = 0$ is imposed on the two walls.

In order to avoid solving for the pressure in order to satisfy continuity, one would want to formulate equation 3.2 in order to both eliminate the pressure and automatically satisfy continuity. This is done first by applying the divergence operator the the momentum equation, obtaining

$$\Delta P = -\rho \nabla \cdot (\boldsymbol{\omega} \times \mathbf{u}), \tag{3.3}$$

given that the divergence operator commutes with both the temporal derivative and the Laplacian, and that $\mathbf{f}$ being constant has zero divergence. Subsequently, we denote for simplicity the nonlinear term of each component of the momentum equation as $h_i = (\mathbf{f} - \boldsymbol{\omega} \times \mathbf{u}) \cdot \hat{\mathbf{e}}_i$. By applying the Laplacian to the wall-normal projection of the momentum equation, and using continuity and equation 3.3, we obtain

$$\partial_\mathrm{t} \Delta v = -\partial_\mathrm{y} \nabla \cdot \mathbf{h} + \Delta h_2 - \frac{1}{\mathrm{Re}_\tau} \Delta (\Delta v). \tag{3.4}$$

With a similar procedure, an equation for the wall-normal vorticity $\eta = \partial_\mathrm{z} u - \partial_\mathrm{x} w$ can be obtained:

$$\partial_\mathrm{t} \eta = \partial_\mathrm{z} h_1 - \partial_\mathrm{x} h_3 - \frac{1}{\mathrm{Re}_\tau} \Delta \eta. \tag{3.5}$$

The solution of equation 3.4 is split into two separate equations to avoid computing the fourth derivative of v, by defining $\phi = \Delta v$. By grouping the nonlinear terms equations 3.4-3.5 become

$$\begin{cases} \partial_\mathrm{t}\phi & = h_\phi - \frac{1}{\mathrm{Re}_\tau}\Delta\phi \\ \Delta v & = \phi \\ \partial_\mathrm{t}\eta & = h_\eta - \frac{1}{\mathrm{Re}_\tau}\Delta\eta \end{cases} \tag{3.6}$$

with the appropriate boundary conditions

$$\begin{cases} v(y = \pm\delta) & = 0 \\ \partial_\mathrm{y} v(y = \pm\delta) & = 0 \\ \eta(y = \pm\delta) & = 0 \end{cases} \tag{3.7}$$

After solving equations 3.6-3.7, the u and w components of the velocity can be recovered by using continuity and the definition of the wall-normal vorticity.

3.1.2 Discretization

Fourier polynomials

Along the x and z directions, where the boundary conditions are periodic, the natural choice for the discretization is to use Fourier polynomials. A periodic field can be approximated by a finite sum of orthogonal, wavelike polynomials of the kind

$$v(\mathbf{x}, t) \approx \sum_{k_x=-N_x/2}^{N_x/2} \sum_{k_z=-N_z/2}^{N_z/2} \hat{v}_{k_x k_z}(y,t) \mathrm{e}^{i2\pi(k_x/l_x x + k_z/l_z z)}. \tag{3.8}$$

The approximation error decays exponentially with the number of modes, although this is true only if all the relevant features of the approximated function have been portrayed by the approximation. The application of the approximation 3.8 to equations 3.6 yields a system of equations for each (k_x, k_z) wavemode pair. Since the ∂_x and ∂_z derivatives are local in wave space, such system is uncoupled:

$$\begin{cases} \partial_\mathrm{t}\hat{\phi}_{k_x k_z} = \hat{h}_{\phi,k_x k_z} - \frac{1}{\mathrm{Re}_\tau}\left(-\alpha^2 - \beta^2 + \partial_\mathrm{yy}\right)\hat{\phi}_{k_x k_z} \\ \left(-\alpha^2 - \beta^2 + \partial_\mathrm{yy}\right)\hat{v}_{k_x k_z} = \hat{\phi}_{k_x k_z} \\ \partial_\mathrm{t}\hat{\eta}_{k_x k_z} = \hat{h}_{\eta,k_x k_z} - \frac{1}{\mathrm{Re}_\tau}\left(-\alpha^2 - \beta^2 + \partial_\mathrm{yy}\right)\hat{\eta}_{k_x k_z} \end{cases} \tag{3.9}$$

where $\alpha = 2\pi k_x/l_x$ and $\beta = 2\pi k_z/l_z$. The nonlinear term in wavespace $\hat{h}_\phi$ and $\hat{h}_\eta$ could be computed starting from the values of the vorticity and the velocity in wavespace with a convolution product, but the computational cost is quadratic with the number of modes and becomes prohibitive quickly. Instead, one can compute the nonlinear terms in real space after computing the transform of the velocity $\hat{\mathbf{v}}$ and the vorticity $\hat{\boldsymbol{\omega}}$. While the computation of discrete Fourier transforms is in general quadratic with the number of modes, the use of Fast Fourier Transform (FFT) algorithms enables its execution in $\mathcal{O}(N \log N)$ time, given that the collocation points are equispaced. In order to avoid aliasing of higher frequencies, the 2/3 rule is applied, by computing the nonlinear terms onto a denser grid [158].

Starting from the definition of the wall-normal vorticity η and from continuity, the streamwise and spanwise velocity can be recovered using

$$\begin{cases} \hat{u}_{k_x k_z} = \frac{-i\alpha\partial_{\mathrm{yy}}\hat{v}_{k_x k_z}+i\beta\eta}{-\alpha^2-\beta^2} \\ \hat{w}_{k_x k_z} = \frac{-i\beta\partial_{\mathrm{yy}}\hat{v}_{k_x k_z}-i\alpha\eta}{-\alpha^2-\beta^2} \end{cases} \tag{3.10}$$

where the spectral representation of derivatives has been used. We note that equation 3.10 is undefined for the (0,0) mode (where $\alpha = \beta = 0$). To recover $\hat{u}_{0,0}$ and $\hat{v}_{0,0}$ the Navier-Stokes equation is used instead

$$\begin{cases} \partial_{\mathrm{t}}\hat{u}_{00} = \hat{h}_{1,00} + \frac{1}{\mathrm{Re}_\tau}\partial_{\mathrm{yy}}\hat{u}_{00} \\ \partial_{\mathrm{t}}\hat{w}_{00} = \hat{h}_{3,00} + \frac{1}{\mathrm{Re}_\tau}\partial_{\mathrm{yy}}\hat{w}_{00} \end{cases} \tag{3.11}$$

Compact finite differences

Due to non-periodicity, the discretization along the wall-normal direction cannot be done by means of Fourier polynomials. A common choice in this regard is to employ Chebyshev polynomials [38], *i.e.*, a set of orthonormal polynomials of the form

$$T_k(y) = \cos\left(k \arccos y\right), \quad y \in [-1{,}1], \tag{3.12}$$

While the choice of Chebyshev polynomials gives arguably the best properties with regards to convergence and also enables the solution of relatively simple linear systems to advance the solution in time, there are also some drawbacks. The choice of the wall-normal grid, which is forced to the Gauss-Lobatto quadrature points, becomes restrictive at high Reynolds numbers. In particular, the quadratic growth of the number of points near the wall quickly leads to a very small grid spacing, which is unnecessary to fully resolve the flow field and most importantly leads to the use of very short time-steps Δt, as one still needs to satisfy the CFL condition

$$\max\left\{\frac{u\Delta x}{\Delta t}, \frac{v\Delta y}{\Delta t}, \frac{w\Delta z}{\Delta t}\right\} < 1 \tag{3.13}$$

to have a stable scheme.

A different choice, granting more flexibility in the selection of the wall-normal grid, is that of an hybrid spatial discretization. In particular, finite difference schemes of high order are a common choice [85, 123, 2]. While the grid can be arbitrarily set and the imposition of boundary conditions is straightforward, the accuracy of ordinary finite differences schemes (in which the derivative at one point is a linear combination of the values of the function at some neighbouring points) is lacking compared to spectral methods, especially for multiscale problems such as turbulence. Indeed, in the previously introduced spectral method, the value (in real space) of the wall-normal derivative at one point is a function of all Chebyshev modes.

A way to mimic the behaviour of spectral derivatives while maintaining the basic idea of finite differences is the use of a *compact* finite differences scheme [172, 119]. Instead of depending only on the values of the function at neighbouring points, the derivative is a linear combination of both neighbouring function values and neighbouring values of the derivative. A scheme of this kind for the second derivative $f'' := \partial_{\mathrm{yy}} f$, comprising of 4 points for the derivative stencil and 7 points for the function stencil, is as follows:

$$\begin{aligned}\beta_{i-2} f''_{i-2} + \beta_{i-1} f''_{i-1} + \beta_i f''_i + \beta_{i+1} f''_{i+1} + \beta_i f''_i = \\ \alpha_{i-3} f_{i-3} + \alpha_{i-2} f_{i-2} + \alpha_{i-1} f_{i-1} + \alpha_i f_i + \alpha_{i+1} f_{i+1} + \alpha_{i+2} f_{i+2} + \alpha_{i+3} f_{i+3}.\end{aligned} \tag{3.14}$$

The β_j and α_j coefficients are computed by matching the Taylor expansion of $f"_j$ and f_j for all j up to the tenth order, with the assumption that $\beta_i = 1$. The resulting linear system, which accounts also for uneven grid spacing, can be solved for all grid points $i = 0 \dots N$. We note that the resulting linear system may be badly conditioned. Particular care needs to be taken when formulating a stencil for the grid points close to the boundaries, where not all stencil points from equation 3.14 are available. No ghost points are used and the stencils are shortened. As an example, the stencil for the second derivative at $i = 0$ is

$$f''_0 + \beta_1 f''_1 + \beta_2 f''_2 = \alpha_0 f_0 + \alpha_1 f_1 + \alpha_2 f_2 + \alpha_3 f_3. \tag{3.15}$$

Assembling the β_j and α_j coefficients computed for each grid point leads to the definition of two banded matrices B_n and A_n for each derivative of n-th order, which can be used to compute the derivative according to

$$B_n \begin{pmatrix} f''_0 \\ \vdots \\ f''_N \end{pmatrix} = A_n \begin{pmatrix} f_0 \\ \vdots \\ f_N \end{pmatrix}. \tag{3.16}$$

Notably, equation 3.16 makes so that the derivative at one point is dependent on the values of the function at all points, mimicking the global dependence of the derivative in spectral space. A scheme of this kind is nominally fourth order, mostly because it is limited by the shorter stencils near the wall.

3.1.3 Time advancement

Following the discretization of the derivatives, a time stepping scheme is needed to advance the solution in time. While a fully implicit scheme would be beneficial in order to relax constraints on the time step, especially for the integration of the linear term which is stiff, the cost associated with the numerical inversion of the nonlinear term makes its use too expensive. The solution in this case is to use a third-order hybrid scheme, which combines a three stage Runge-Kutta scheme for the nonlinear terms and an implicit Crank-Nicholson scheme for the linear operator [197]. Indicating with $L(f) = \nu \Delta f$ the linear operator and with $N(f)$ the nonlinear term, a substep of the scheme is

$$f^{k+1} = f^k + \Delta t \left[\alpha_k L(f_k) + \beta_k L(f_{k+1}) + \gamma_k N(f_k) + \zeta_k N(f_{k-1})\right], \quad k = 1{,}2{,}3 \tag{3.17}$$

with the coefficients

$$\alpha = \begin{pmatrix} \frac{29}{96} \\ -\frac{3}{40} \\ \frac{1}{6} \end{pmatrix} \qquad \beta = \begin{pmatrix} \frac{37}{160} \\ \frac{5}{24} \\ \frac{1}{6} \end{pmatrix} \qquad \gamma = \begin{pmatrix} \frac{8}{15} \\ \frac{5}{12} \\ \frac{3}{4} \end{pmatrix} \qquad \zeta = \begin{pmatrix} 0 \\ -\frac{17}{60} \\ -\frac{5}{12} \end{pmatrix} \tag{3.18}$$

In equation 3.17 f_0 is the state at the previous full step, while f_3 is the next full step.

With the introduction of a time-stepping scheme, it is possible to discuss how the boundary condition are imposed to the solution of equations 3.6-3.7. In particular, while the Dirichlet conditions on ϕ and η can be readily imposed when integrating these two quantities, the imposition of the Neumann condition on the wall-normal velocity is not straightforward, as one would need to determine the (nonzero) value of ϕ at the boundaries that yields a null derivative of v. To do so, we first define

$$\mathcal{L}(f^{k+1}) = f^{k+1} + \Delta t \beta_k L(f^{k+1}) \tag{3.19}$$

and

$$\mathcal{R}(f^k) = f^k + \Delta t \left[\alpha_k L(f^k) + \gamma_k N(f_k) + \zeta_k N(f_{k-1})\right]. \tag{3.20}$$

The solution is split into three separate problems. The first is the particular solution containing the full right hand side of the time-stepping scheme $\mathcal{R}$ and homogeneous boundary conditions for ϕ

$$\begin{cases} \mathcal{L}(\phi_p^{k+1}) = \mathcal{R}(\phi_p^k) \\ L(v_p^{k+1}) = \phi_p^{k+1} \\ \phi_p^{k+1}(y = \pm\delta) = 0 \\ v_p^{k+1}(y = \pm\delta) = 0 \end{cases} \tag{3.21}$$

The other two problems solve the homogeneous problem without the right hand side $\mathcal{R}$ and with a one-sided unitary Dirichlet condition at the boundary

$$\begin{cases} \mathcal{L}(\phi_a^{k+1}) = 0 \\ L(v_a^{k+1}) = \phi_a^{k+1} \\ \phi_a^{k+1}(y=\delta) = 1 \\ \phi_a^{k+1}(y=-\delta) = 0 \\ v_a^{k+1}(y=\pm\delta) = 0 \end{cases} \tag{3.22}$$

$$\begin{cases} \mathcal{L}(\phi_b^{k+1}) = 0 \\ L(v_b^{k+1}) = \phi_b^{k+1} \\ \phi_b^{k+1}(y=\delta) = 0 \\ \phi_b^{k+1}(y=-\delta) = 1 \\ v_b^{k+1}(y=\pm\delta) = 0 \end{cases} \tag{3.23}$$

The full solution is recovered by summing the solution of the particular problem and those of the two homogeneous problems

$$\phi^{k+1} = \phi_p^{k+1} + A\phi_a^{k+1} + B\phi_b^{k+1} \tag{3.24}$$

$$v^{k+1} = v_p^{k+1} + Av_a^{k+1} + Bv_b^{k+1} \tag{3.25}$$

The coefficients A and B are determined in order to yield $\partial_{\mathrm{y}} v^{k+1}(\pm\delta) = 0$ by solving a 2x2 linear system:

$$\begin{bmatrix} \partial_{\mathrm{y}} v_a(\delta) & \partial_{\mathrm{y}} v_b(\delta) \\ \partial_{\mathrm{y}} v_a(-\delta) & \partial_{\mathrm{y}} v_b(-\delta) \end{bmatrix} \begin{pmatrix} A \\ B \end{pmatrix} = -\begin{pmatrix} \partial_{\mathrm{y}} v_p(\delta) \\ \partial_{\mathrm{y}} v_p(-\delta) \end{pmatrix} \tag{3.26}$$

The homogeneous problems 3.22-3.23 and the inversion of the linear system 3.26 do not depend on time and thus do not need to be solved at any iteration. Instead, the homogeneous solutions $v_{a/b}$, $\phi_{a/b}$ can be computed once (at least, if the time-step does not change) and stored.

3.2 Implementation

In this section, the implementation of a novel channel flow code will be described. The code employs a pseudospectral method, with Fourier-Galerkin discretization along the streamwise x and spanwise z directions. Compact finite differences are used to compute y (wall-normal) derivatives. Given the computational cost involved with the solution of the Navier-Stokes equations at reasonable values of the Reynolds number Re_τ, the code has been designed to run on parallel machines, leveraging a large amount of computer cores. The code has been written using the C++ language, is compiled on Linux machines using `g++` and uses OpenMPI v4 for the parallelization.

Modern supercomputer architectures are composed by a large number of compute nodes, each one containing $\mathcal{O}(100)$ of single CPU cores. The total number of CPU cores in today's systems reaches the hundreds of thousands [195]. The standard for the creation of parallel application on HPC (High Performance Computing) architectures is the Message Passing Interface (MPI), which allows the user to assign different data and different instructions to several parallel processes and provide means of exchanging data between processes [46]. DNS codes are usually parallelized by assigning a subset of the wavenumbers to each process. Given that most of the computation, including especially the time-advancement, is local to the wavenumber, each process can advance the data related to its wavenumber subset. Still, since the pseudospectral code requires a transform of the spectral fields into physical space, the program needs to exchange data between cores in order to compute the discrete Fourier transforms necessary to obtain real data.

In the case of channel flow codes, a common parallelization strategy is to divide either the spanwise k_z or streamwise k_x wavenumber between different MPI processes, which is commonly termed as a *slab* architecture. In this case, only one communication pass is needed to compute a transform into real space. Still, the main drawback is that the total number of usable MPI processes (and thus of CPU cores) is limited by the number of spanwise N_z or streamwise N_x wavenumbers; because of this, the large number of CPU cores available in an HPC system may not be fully leveraged. A common workaround is to assign multiple CPU cores to each MPI process by employing a shared memory paradigm such as OpenMP [39, 111, 123]. Unfortunately, the overhead associated with spawning multiple shared memory threads and the poor scaling of the performance makes so that also in this way the number of total CPU cores used cannot be increased indefinitely.

Another method, which enables the use of a larger number of cores, is to split both the k_x and k_z wavenumbers across MPI processes, yielding a *pencil* (two-dimensional) parallelization. The number of MPI processes becomes then roughly bounded by $N_x N_z$, which for large values of Re_τ approaches $\mathcal{O}(10^6)$. The drawback in this case is that two communication passes are needed to transform the data into real space, instead of one as was for the slab parallelization. Given the large latency of communications compared to compute and memory operations, especially when the network interconnection is involved, some remediation to the penalty imposed by the double communication is needed.

The code described in the following employs a pencil parallelization and adopts a topology-aware implementation of the communications to reduce the associated cost.

Data structure

The spectral coefficients $\hat{f}_{k_x k_z}(y,t) \in \mathfrak{C}$ of the generic field $f(\mathbf{x},t) \in \mathfrak{R}$ with $N_x \times N_z$ polynomials are

$$f(\mathbf{x},t) = \sum_{k_x=-N_x/2}^{N_x/2-1} \sum_{k_z=-N_z/2}^{N_z/2} \hat{f}_{k_x k_z}(y,t) \mathrm{e}^{i(\alpha x+\beta z)}, \tag{3.27}$$

which satisfy the Hermitian symmetry property, *i.e.* $\hat{f}_{k_x k_z} = \hat{f}^{\star}_{-k_x -k_z}$, where the * indicates complex conjugation. Because of this, only around half of the Fourier coefficients need to be stored. In particular, we discard coefficients with negative k_x, so that the total number of stored coefficients is $N_x/2+1 \times N_z$. These wavenumbers need to be split across MPI processes. All the grid points along y for each single wavenumbers are stored on the same process, as they are needed together during the time advancement of the solution. We define a number of processes along which the k_x wavenumbers are split, that is N_s, and a number of processes along which the k_z wavenumbers are split, *i.e.* N_c. The total number of processes is thus $N_c N_s$.

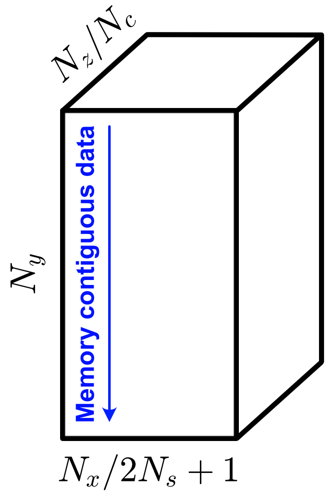

Figure 3.2: Array structure in spectral space; the blue arrow indicates column-major storage

On each process, variables in spectral space are stored in an array of complex numbers in double precision, with size $N_y \times N_x/2N_s + 1 \times N_z/N_c$, as is depicted in figure 3.2. The $+1$ frequency along x is unused on all processes except the last, where it is used to store the Nyquist frequency. The object used to store the data is an `Eigen::TensorFixedSize<std::complex<double>>` object from the Eigen library, which provides indexed access to the data and vectorized array operations [57]. The data is stored into memory in column-major order, *i.e.* when traversing the array sequentially into memory the fastest changing index is the first. Column-major storage is indicated by the blue arrow in the figure. The first dimension of the array has been chosen to be y so that all the data from a single wavenumber is stored in a contiguous memory location and can be copied using fast, vectorized operations.

Communications and transforms to real space

To obtain the data in real space, two communications and two one-dimensional transforms of the data need to be performed. The first communication makes so that all k_z wavenumbers are gathered on the same processes, while splitting the y grid points along the N_c processes. After this, the 1D, complex-to-complex transform along z can be performed. Subsequently, the second communication gathers all k_x wavenumbers on the same processes, while splitting the now-transformed z spatial points along the N_s processes. Finally, the 1D complex-to-real transform is performed, yielding the full real data.

In order to optimize the double communication, we implement a strategy that relies on the knowledge of the hardware topology. The two communications take place along an abstract structure defined by the MPI standard, that is the *communicator*. An MPI application usually defines a global communicator, containing all processes. In our code, we also define a set of N_s subcommunicators containing each N_c processes for the communication along z, and a set of N_c subcommunicators containing each N_s processes for the communication along x. We then impose that all processes in the z-subcommunicators are located on the same physical processor, so that at least one of the two communications does not need to happen over the network and thus has better performance. Recent processors used in HPC systems have a large number of CPU cores (64 or even 96). Also, the interconnection speed between cores on the same processors is much faster than that taking place over the network. The OpenMPI implementation provides a function (`MPI_Comm_split_type`) that allows the creation of split subcommunicators according to hardware topology. The x-communicator instead comprises processes spanning different sockets, that is different physical processors. We note that each machine generally contains at least one socket, with two being the most common.

The procedure used to perform the transform is the following:

- Using a call to the `MPI_Alltoallw` function along the intra-node communicator, the k_z wavenumbers are gathered onto the same process according to the schematic shown in figure 3.3. By setting the datatype and displacement parameters in the function call it is possible to transfer the data from the spectral array to a buffer of size $N_y/N_c \times N_x/2N_s + 1 \times 3N_z/2$ in a single pass. Also,

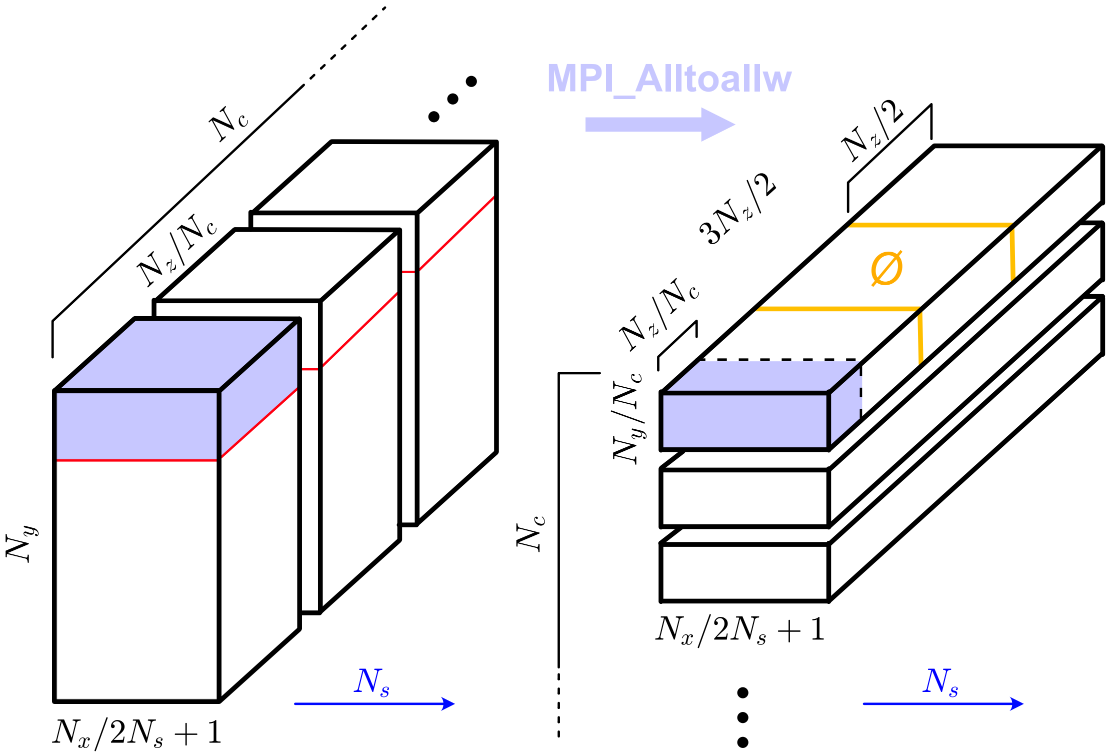

Figure 3.3: Schematic of the first communication. Solid blocks indicate arrays of data stored on the same process. The purple region is the message transferred between two processes.

by setting an offset to the displacement of the data sent by the second half of the processes, it is possible to automatically introduce the padding of the array according to the 2/3 rule. We recall that, in order to avoid aliasing, the nonlinear terms are to be calculated on a grid with a larger number of points than the number of polynomials, specifically 50% more points. To do so, before performing the discrete Fourier transform, the array of the spectral coefficients is padded with zero, so that the FFT algorithm performs the transform onto a larger grid. We also note that the coefficients are stored in the order provided by the output of the FFT routine, *i.e.* first all the positive coefficients, than the negative coefficients in inverse order: $k_z = 0{,}1{,}2\ldots-3,-2,-1$. Because of this, the padding is added in the middle of the buffer.

- A 1D, complex-to-complex transform is performed along z, using the FFT algorithm. The FFTW library is used, which allows to perform multiple 1D transforms at once improving computation time. We note that the FFTW library requires a planning phase, which is executed once before the main computation occurs.

- The data is now a function of the real coordinate z the z-axis of the arrays. The k_x wavenumbers are gathered onto the same process using another call to `MPI_Alltoallw`. From each process, except the last, the $k_x = N_x/2N_s + 1$ frequency is discarded. The Nyquist frequency is distributed from the process with rank equal to N_s using `MPI_Scatterv`. Again, padding is introduced by transferring the data into a larger array, so that zeros are at the end of the array (noting that only the positive wavenumbers are stored). The receiving buffer has size $N_y/N_c \times 3N_x/4+1\times 3N_z/2N_s$ and this transform is schematized in figure 3.4.
- A 1D, complex-to-real transform is performed along x, using the specific FFT algorithm that exploits the Hermitian symmetry. The final array, holding fully real data, has size $N_y/N_c \times 3N_x/2 \times 3N_z/2N_s$ and is again split across cores and sockets, albeit in a different fashion.

Using a similar, but inverse procedure, the data can be transformed from real space to its spectral coefficients.

The transform operation, including the communication passes, is in general the most computationally expensive operation in the simulation process, accounting for up to 80% of the total runtime. Because of this, any optimization yields great benefit. The performance improvement given by the topology aware implementation depends on the size of the message transferred during the z-communication, which is $16N_yN_z(Nx/2N_s+1)/N_c^2$ bytes. This dependence is caused by the fact that the transferred message needs to fit into the processor cache to be actually able to be transferred between cores. During preliminary testing we found that the mean and median speedup with respect to a topology-unaware solution was the largest when the message size is around 100 kB.

Code description

The computer code executes the following steps:

1. the global, intra-node and inter-node communicator are initialized taking into account the available computational resources
2. the FFTW planning phase is executed according to the array sizes set by the user
3. the matrices used to compute the wall-normal derivatives are obtained using a compact finite differencing scheme as the one previously described in this Chapter
4. the homogeneous solutions $v_{a/b}$ and $\phi_{a/b}$ are computed

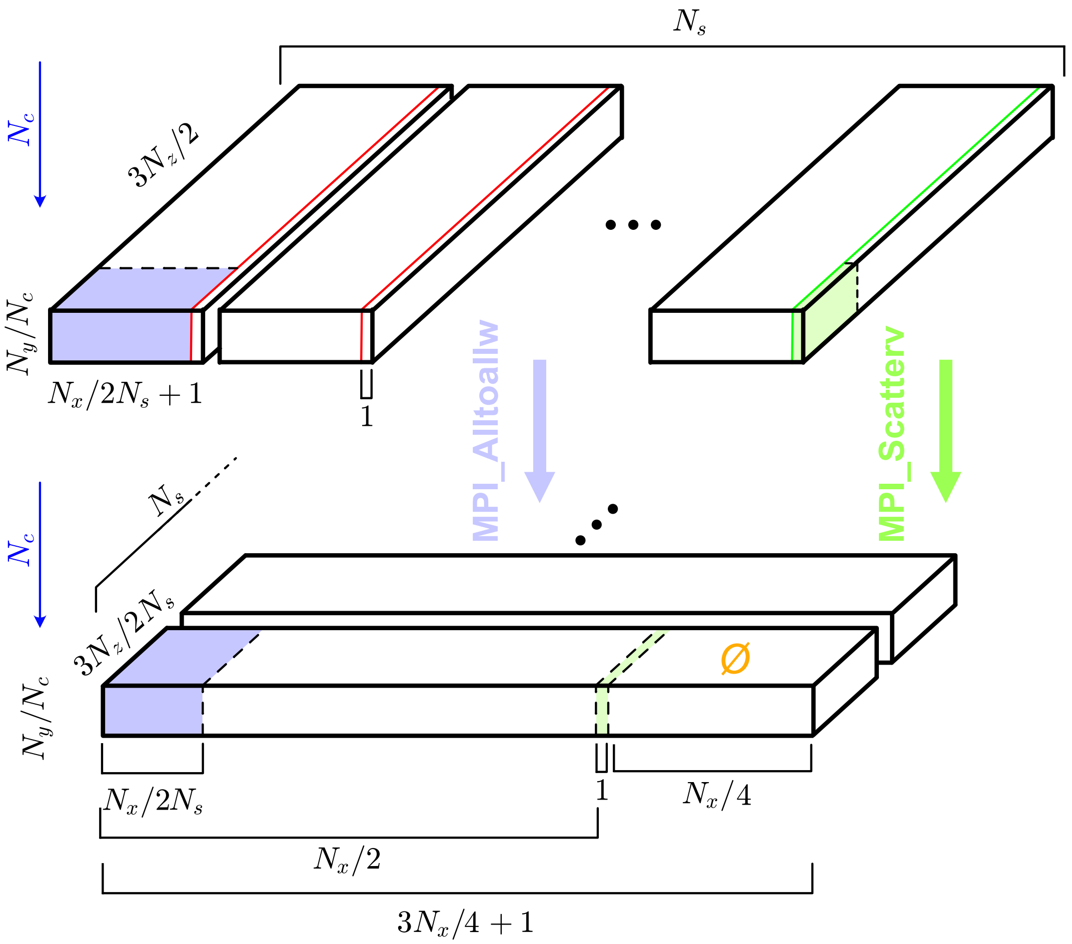

Figure 3.4: Schematic of the second communication. Solid blocks indicate arrays of data stored on the same process.

5. an initial condition is set, either from a stored file or as a superposition of a parabolic profile with large amplitude waves that trigger rapid transition to a fully developed turbulent state

6. the time-stepping starts:

   - at the beginning of each substep of the Runge-Kutta scheme, the velocity data in spectral space is used to compute the vorticity in spectral space, according to

$$\omega_x = \partial_{\mathrm{y}} w - \partial_{\mathrm{z}} v, \qquad \omega_y = \partial_{\mathrm{z}} u - \partial_{\mathrm{x}} w, \qquad \omega_z = \partial_{\mathrm{x}} v - \partial_{\mathrm{y}} u \tag{3.28}$$

   - the three velocity and vorticity components are transformed from spectral space to real space using the previously described routines. Using the data in real, the nonlinear term is computed:

$$h_1 = f_x - w\omega_y + v\omega_z, \qquad h_2 = w\omega_x - u\omega_z, \qquad h_3 = u\omega_y - v\omega_x, \tag{3.29}$$

where $f_x = 1$ is the mean pressure gradient, or equivalently the constant bulk force. After the three nonlinear terms are computed, they are transformed back into spectral space and the nonlinear terms h_η and h_ϕ are obtained from 3.5-3.4.

- the equation that advances the wall-normal vorticity η in time can now be solved. Equation 3.17, applied to the vorticity, reads

$$\left(1 - \beta_k \Delta t L\right) \eta^{k+1} = \left(1 + \alpha_k \Delta t L\right) \eta^k + \Delta t \left(\gamma_k N_k + \zeta_k N_{k-1}\right). \tag{3.30}$$

By introducing the spectral representation of the derivatives into the linear operator L and by indicating the right hand side with $\mathcal{R}_k$, equation 3.30 becomes

$$\left(1 - \beta_k \Delta t \frac{-\alpha^2 - \beta^2 + \partial_{\mathrm{yy}}}{\mathrm{Re}_\tau}\right) \eta^{k+1} = \mathcal{R}_k \tag{3.31}$$

which is valid for each wavenumber pair (k_x, k_z). Multiplying by the compact finite differences second order matrix B_2, and substituting the differencing relation 3.16, we finally obtain

$$\left[\left(1 - \beta_k \Delta t \frac{-\alpha^2 - \beta^2}{\mathrm{Re}_\tau}\right) B_2 - \frac{\beta_k \Delta t}{ret} A_2\right] \eta^{k+1} = B_2 \mathcal{R}_k, \tag{3.32}$$

which is an heptadiagonal linear system. We solve this linear system using the Lapack solver for banded matrices `zgbsv`, which is more suitable than a general full matrix solver.

- the same procedure is performed for the advancement of ϕ
- the equation $\Delta v^{k+1} = \phi^{k+1}$ is solved in order to obtain the wall-normal velocity. The derivatives at the wall of the particular solution are computed, so that the coefficients A and B of the homogeneous solutions can be determined. The full solution is thus assembled.
- following [123], if the time step does not change the value of the linear operator $L(\phi^{k+1})$ and $L(\eta^{k+1})$ is computed and stored using

$$L(\phi^{k+1}) = \frac{\phi^{k+1} - \mathcal{R}_k}{\beta_k \Delta t} \tag{3.33}$$

which does not involve the computation of the derivatives and thus improves accuracy.

- the streamwise and spanwise velocity are computed starting from v and η using equations 3.10, except for the 0-0 mode for which the Navier-Stokes equation 3.11 is solved in a similar fashion to the equations for η and ϕ.

7. at the end of each step, if necessary, the Courant number is computed. The simulation can be run with constant Courant number instead of constant Δt. Since the change of the time step Δt causes the need to recompute the homogeneous solutions and the linear operators, an hybrid approach is more advisable, *i.e.* the time step can be adjusted every few (≈ 50) steps.

8. statistical quantities such as the bulk velocity and the wall friction are computed. Velocity fields can be stored to disk.

3.3 Simulation of transitional flows

The simulation of transitional flows can be achieved in several ways. If spatial transition is concerned, the matter is complicated by the need to impose a boundary condition that accounts for the evolution of the flow from laminar to turbulent. Conversely, one would prefer to employ a pseudospectral method, due to its benefits, also along the direction along which the flow evolves, even if the approximation with Fourier polynomials imposes the use of a periodic boundary condition.

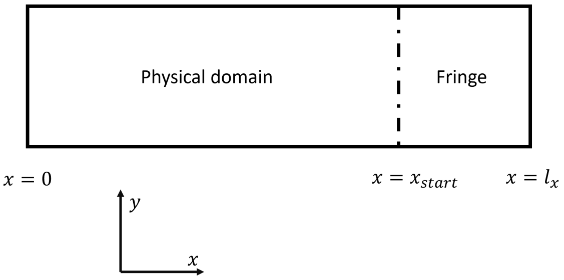

Figure 3.5: Domain division into physical and fringe regions.

The solution that will be discussed in this section and that has been implemented for some of the work that will be discussed later (see chapter 7) is that of the *fringe region* technique [187, 146]. The numerical solver is identical to the fully developed case, but a localized forcing term is added in the Navier-Stokes equation:

$$\frac{\partial \mathbf{v}}{\partial t} + \mathbf{v} \cdot \nabla \mathbf{v} = -\frac{1}{\rho}\nabla p + \nu \Delta \mathbf{v} + \lambda(x)(\tilde{\mathbf{v}} - \mathbf{v}), \tag{3.34}$$

where $\lambda(x)$ is the shape function of the forcing and $\tilde{\mathbf{v}}$ is the desired inflow solution.

The shape function is nonzero only in a confined portion of the domain, *i.e.*, the fringe region as shown in figure 3.5, and has equation

$$\lambda(x) = \lambda_{\text{max}} S\left(\frac{x - x_{\text{start}}}{\Delta_{\text{rise}}}\right) - S\left(\frac{x - x_{\text{end}}}{\Delta_{\text{fall}}}\right), \tag{3.35}$$

where $S(y)$ is a smooth step function

$$S(y) = \begin{cases} 0 & \text{if } y \leqslant 0 \\ 1/\left[1 + \mathrm{e}^{\left(\frac{1}{y-1}+\frac{1}{y}\right)}\right] & \text{if } 0 < y < 1 \\ 1 & \text{if } y \geqslant 1 \end{cases} \tag{3.36}$$

and $\lambda_{\max}$ is positive and of the order of Δt^{-1}.

Inside the fringe region, which is usually set at the end of the physical domain (although this is not necessary due to periodicity), the flow is forced towards the imposed solution $\tilde{\mathrm{v}}$. The imposed solution acts as a distributed boundary condition; indeed, at the end of the fringe region the flow evolves again according to the physically-sound Navier-Stokes equations. In the following, we will set $\tilde{\mathrm{v}}$ to be a superposition of the laminar profile and of two solutions of the Orr-Sommerfeld equations, *i.e.* a two-dimensional and a three-dimensional Tollmien-Schlichting wave. By doing so, the flow at the beginning of the domain is laminar with some perturbations, after which it evolves naturally into turbulence. When the fringe region is reached, the flow is forced back to the laminar perturbed state, so that periodicity is satisfied. The computational domain needs to be sufficiently elongated to enable transition to fully occur.

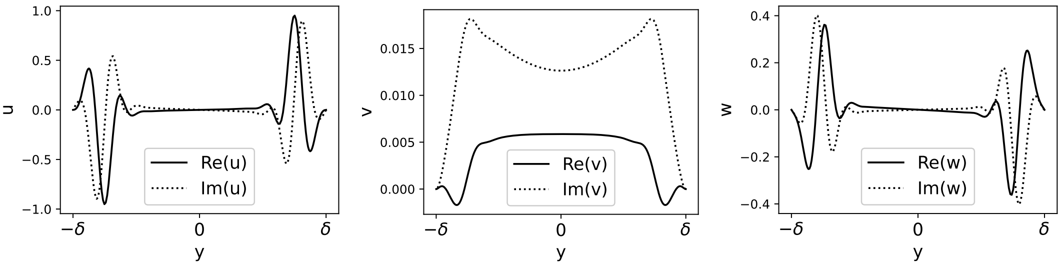

(a) Streamwise component (b) Wall-normal component (c) Spanwise component

Figure 3.6: Three-dimensional eigenfunctions of the spatially evolving Orr-Sommerfeld equation for $\alpha_{3D} = 0.788 + 0.2106i$, $\beta = 2$ and $\omega = 0.3$.

As the perturbations are spatially evolving, the Orr-Sommerfeld equation needs to be formulated for spatially evolving waves:

$$\frac{\mathrm{d}^4\hat{v}}{\mathrm{d}y^4} - 2\left(\alpha^2+\beta^2\right)\frac{\mathrm{d}^2\hat{v}}{\mathrm{d}y^2} + \left(\alpha^2+\beta^2\right)^2\hat{v} - i\alpha Re_c\left(1-y^2\right)\left[\frac{\mathrm{d}^2\hat{v}}{\mathrm{d}y^2} - \left(\alpha^2+\beta^2\right)\hat{v}\right] - 2i\alpha Re_c\hat{v} = \\ = -i\omega Re_c\left[\frac{\mathrm{d}^2\hat{v}}{\mathrm{d}y^2} - \left(\alpha^2+\beta^2\right)\hat{v}\right], \tag{3.37}$$

where $Re_c = 3Re_b/2$ is the centerline Reynolds number of the parabolic streamwise velocity profile, α and β are the streamwise and spanwise wavenumbers of the perturbation and ω is the temporal wavenumber of the perturbation (which is real because the TS waves evolve only in space). Equation 3.37 is a nonlinear eigenvalue problem which can be solved, after proper space discretization, with the companion matrix method. An example of the solution is given in figure 3.6.

After solving the Orr-Sommerfeld equation, the other components of the velocity may be obtained by using continuity in the two-dimensional case or by solving Squire's equation in the three dimensional one. Taking $e\hat{t}a$ as the wall-normal vorticity, Squire's equation is

$$\frac{\mathrm{d}^2\hat{\eta}}{\mathrm{d}y^2} - \left(\alpha^2 + \beta^2\right)\hat{\eta} - \mathrm{Re}_c\left[i\alpha\left(1 - y^2\right) - i\omega\right]\hat{\eta} = -2i\beta y\hat{v}. \tag{3.38}$$

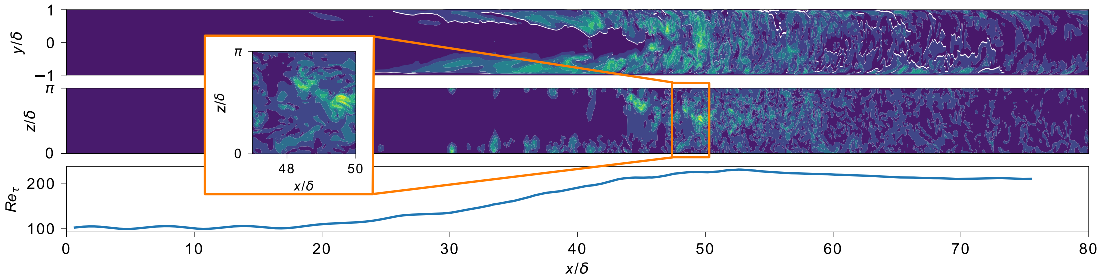

Figure 3.7: Flow field of a spatially evolving transitional flow obtained using the fringe region technique. On the bottom, the evolution of the friction Reynolds number Re_τ is plotted against the streamwise coordinate x. The fringe region is omitted from the plots

3.4 Particle tracking

In order to perform Lagrangian simulations, a method to integrate trajectories of particles inside a turbulent velocity field is needed. To do so, two necessities arise: the definition of an integration scheme and the choice of an interpolation method of the discrete simulation data (as particles are not located, in general, in the grid points during their motion).

While the choice of the former is usually simple, as one uses the same explicit integration which is employed to integrate the nonlinear terms in the Eulerian simulation, the choice of the latter is more difficult. Different approaches may be used, ranging from the direct transformation of the spectral coefficients of the velocity at the particle location (which usually has prohibitive computational cost) to trilinear interpolation. In this case the velocity is obtained using the values of the immediately neighbouring grid points in real space. To obtain a denser grid onto which compute the interpolation, usually the real field obtained after dealiasing is used. In this way, the number of grid points is increased by a factor of 3/2 along the periodic directions.

The use of the linear scheme may lead to the introduction of large errors, especially in the computation of the acceleration of particles [83]. Still, the spatial positions of particles obtained through trilinear interpolation are statistically accurate if a large enough sample of tracers is considered [111].

After the velocity of the flow field $\mathbf{v}$ at the particle position $\mathbf{X}$ is obtained, one may integrate it to obtain the trajectory of the particle using

$$\frac{\mathrm{d}\mathbf{X}}{\mathrm{d}t} = \mathbf{v}, \tag{3.39}$$

which is advanced in time using a time-stepping scheme of choice.

In the case of inertial particles, the velocity of the particle $\mathbf{v}_p$ differs from that of the fluid at the same point (assuming point particles). In this case, also the velocity of particles needs to be integrated according to

$$\frac{\mathrm{d}\mathbf{v}_p}{\mathrm{d}t} = \frac{\mathbf{v}(\mathbf{X}) - \mathbf{v}_p(\mathbf{X})}{\tau_p}, \tag{3.40}$$

with τ_p being the particle relaxation time. Furthermore, a correction can be defined for particles with non-negligible Reynolds number, that is

$$\frac{\mathrm{d}\mathbf{v}_p}{\mathrm{d}t} = \frac{\mathbf{v}(\mathbf{X}) - \mathbf{v}_p(\mathbf{X})}{\tau_p}\left(1 + 0.15\mathrm{Re}_p^{0.687}\right), \tag{3.41}$$

where $\mathrm{Re}_p = d_p||\mathbf{v} - \mathbf{v}_p||/\nu$ is the particle Reynolds number [130].

If the back reaction of inertial particles is to be accounted for, then the force acting from the fluid on particles needs to be computed and added back as a forcing in the momentum equation by distributing it onto the nearby grid points. Additionally, if four-way coupling, (*i.e.*, collisions) is to be included in the simulation, one needs to compute the mutual distance of all particle pairs to see if they come closer than their diameter.

Chapter 4

Complex networks and fluid flows

In this Chapter the theory of networks and its application to the study of fluid flows are introduced. Since its emergence from the work of Euler, graph theory has provided a way to transform physical problems into geometrical ones and algebraic methods to treat this geometrical interpretation of reality [25, 67, 61, 1]. The study of networks has found its use in a large amount of problems, spanning from the coloring of maps to path planning and protein folding [212, 223, 95]. The definition of networks encompasses a large class of mathematical objects that are particularly suitable to represent the non-trivial interactions between objects in a complex system. The mathematical foundation of network theory, along with the relevant metrics and strategies to compute them, are given in Section 4.1. Furthermore, a brief review of recent application to fluid dynamics is delineated in Section 4.2.

4.1 Networks

4.1.1 Definition

A network, or *graph*, $\mathcal{G}$ is a mathematical object consisting of two sets, one of vertices, or nodes, $\mathcal{V} = \{v_i\}$ and one of edges, or links, $\mathcal{E} = e_{ij} = (v_i, v_j)$ [9]. The *order* of a graph, that is the number of vertices, is $N = |\mathcal{V}|$, while its *size* $K = |\mathcal{E}|$ is the number of edges it contains. If two nodes are connected, they are said to be *adjacent*.

Each edge e_{ij} connects two nodes v_i and v_j, so that it can be represented as the unordered (ordered) pair of vertices it connects. In the case of unordered pairs, the graph is *undirected*, *i.e.* each edge does not contain a directional information and $e_{ij} \in \mathcal{E} \iff e_{ji} \in \mathcal{E}$. On the other hand, graphs that account for a directional

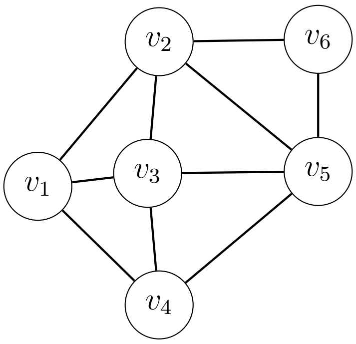

Figure 4.1: Example of a graph. The vertexes $\{v_i\}$ are connected by a set of edges.

information contained in edges are called *directed graphs*, and the existence of a directed edge from node v_i to v_j does not imply the existence of the edge from v_j to v_i ($e_{ij} \in \mathcal{E} \nRightarrow e_{ji} \in \mathcal{E}$). Given that in general $e_{ii} \notin \mathcal{E}$ (a graph does not contain self-loops, *i.e.*, edges that start and end on the same vertex), the maximum size of an undirected graph of order N is $N\left(N-1\right)/2$, while the maximum size of the equivalent directed graph is $N\left(N-1\right)$. A graph is said to be *complete* if it contains all possible edges. A subset of nodes *induces* a subgraph, which is a graph comprising of the subset of nodes and the subset of edges that are incident to these nodes [26].

If a scalar value W_{ij} is associated with each edge, the graph is said to be *weighted*. Weighted networks are useful to model systems where pairwise interactions are not only binary, but also have a measurable property [54]. Networks that model the transport of a physical quantity, as an example, have edges that are weighted according to the amount of transport taking place between two connected nodes.

From the definition of links one can introduce a straightforward representation of a graph in algebraic form, *i.e.*, the *adjacency matrix* $\mathbf{A} \in \mathbb{R}^{N\times N}$. Each element of $\mathbf{A}$ is defined as

$$A_{ij} = \begin{cases} 1, \text{ if } e_{ij} \in \mathcal{E} \\ 0, \text{ if } e_{ij} \notin \mathcal{E}. \end{cases} \tag{4.1}$$

From its definition, some properties of A follow. It is a square matrix of the same size of the graph, which is symmetric for undirected graphs ($a_{ij} = a_{ji}$) and asymmetric for directed ones ($a_{ij} \neq a_{ji}$). Analogously, a matrix $\mathbf{W}$ containing for each i, j pair the value of the weight corresponding to the link between v_i and v_j, that is, the *weight matrix*, can be defined. In the case of the simple graph shown in figure 4.1, the adjacency matrix is

$$\mathbf{A} = \begin{bmatrix} 0 & 1 & 1 & 1 & 0 & 0 \\ 1 & 0 & 1 & 0 & 1 & 1 \\ 1 & 1 & 0 & 1 & 1 & 0 \\ 1 & 0 & 1 & 0 & 1 & 0 \\ 0 & 1 & 1 & 1 & 0 & 1 \\ 0 & 1 & 0 & 0 & 1 & 0 \end{bmatrix} \tag{4.2}$$

The adjacency matrix is not only a convenient way to store a graph, but it also enables the computation of its properties. Most notably, the algebraic properties of A map into the most important properties of the graph, fulfilling the transformation of a complex sets of objects and their interplay into an algebraic form. In the following paragraphs, the most important properties of graphs and the way they are obtained from its matrix representation are detailed.

4.1.2 Centrality measures

An important class of network metrics is that of *centrality* measures. Centrality refers to the importance of a node in the network, especially with respect to the role of each node in the dynamical phenomena that is taking place on the network. A common example is that of the aerial transportation network, where airports acts as node and their centrality, measured using different metrics, characterizes the importance of each airport in the network.

Degree centrality The most straightforward centrality measure is the *degree* k, which is the number of connections incident to each node. In the case of an undirected network, it is the row-wise sum (or the column-wise one, which is equivalent due to symmetry) of the adjacency matrix

$$k_i = \sum_{j \in \mathcal{V}} A_{ij}. \tag{4.3}$$

In the case of directed graphs instead, two variants of the degree are computed. The *ingoing* degree k_i^{I} refers to the number of edges that ends in the i-th node, while the outgoing degree k_i^{O} is the number of edges that starts in said node. Both are again computed from the adjacency matrix as the column- and row-wise sums, respectively:

$$k_i^{\mathrm{I}} = \sum j \in \mathcal{V} A_{ji}, \tag{4.4}$$

$$k_i^{\mathrm{O}} = \sum j \in \mathcal{V} A_{ij} \tag{4.5}$$

Furthermore, in the case of weighted networks, the equivalent sums of the weight matrix W yield the value of the strength s (both for the directed and undirected variants) of each node.

The statistical distribution of the degree $P(k)$ provides an insightful characterization of network properties. The statistical moments of the degree give information on the average number of connections (which is obtained from the mean degree) and on the statistical differences between nodes. Random graphs models, in particular, are fully characterized by their degree distribution, as long as N is large. Original random models accounted for equiprobable edge formation (thus yielding binomial degree distributions) [59]. With the incipient application of graph theory to the data derived from large, real-world systems (such as social networks), it was noted that common network organizations were not adequately represented by models that considered edge formation equally probable independently of each other. Instead, it was found that edges where more likely to be incident to high-degree nodes. Such networks have a degree distribution that follow a power law

$$P(k) = Ck^{-\gamma}, \tag{4.6}$$

and are usually termed *scale-free* networks [220]. Scale-free networks indeed follow a fractal degree distribution, which most notably makes so that their features are similar independently of the scale considered (at least, for very large graphs). Scale-free networks exhibit an organization which is typical of many common systems, *i.e.*, one composed of *hubs*, which are the few nodes with large amounts of connection, or high degree centrality, and a multitude of poorly connected nodes.

Paths and betweenness centrality Two nodes may be directly connected, or they may be connected through a *path*, that is an ordered set of edges, comprising of more than one edge. Among all paths connecting two nodes i and j, there is one which is the *shortest path* of length d_{ij}, which is composed by the minimum number of edges. The search of shortest paths between edges is a problem of great importance in graph theory, as it is strongly related to the real-world problems which are mapped into networks. From the algorithmic standpoint, the calculation of shortest paths has in general quadratic complexity with the number of nodes, which makes optimization strategies important especially for very large graphs. The most notable algorithm devised to search for shortest paths in a network is that of Dijkstra [49]. The definition of shortest path can be extended to weighted networks by using the weight as a cost measure or, conversely, an efficiency measure and penalize/prioritize specific paths accordingly.

The importance of nodes can be quantified starting from the notion of shortest paths. Intuitively, the importance of a node may be measured by the number of shortest paths that include it, which is in general unrelated to the number of connections (the degree). As an example, in a communication network nodes that are traversed by a large number of shortest paths are bottlenecks, where large amounts of data flow and that, in the event of failures, have a major impact on the network dynamic as a whole [10]. The (normalized) number of shortest paths passing through a node is the *betweenness centrality*, defined as

$$B_i = \sum_{s,t \in \mathcal{V}, s \neq t \neq i} \frac{n_{st}(i)}{n_{st}}, \tag{4.7}$$

where n_{st} is the number of shortest paths connecting vertices s and t and $n_{st}(i)$ the number of those paths that pass through the i-th node. Equation 4.7 can be extended to measure the number of shortest paths running through each edge

$$B_{ij} = \sum_{s,t \in \mathcal{V}, s \neq t} \frac{n_{st}(ij)}{n_{st}}, \tag{4.8}$$

where $n_{st}(ij)$ is the number of shortest paths passing through the e_{ij} edge. Furthermore, an average (or *characteristic*) path length can be defined as the average length of the shortest paths connecting all pair of nodes

$$L = \frac{1}{N(N-1)} \sum_{i,j,\, i \neq j} d_{ij}, \tag{4.9}$$

which measures the typical distance between nodes in a graph and is useful to characterize the efficiency of a network in transferring information between nodes. If disconnected components are present in the graph, *i.e.*, if there are some pairs of nodes for which there is no possible path, the characteristic path length diverges.

Eigenvector centrality Another quantification of centrality arises from the consideration of an intertwined metric, one in which the centrality of a node is determined by the centrality of the nodes it is connected to. By setting the centrality measure e_i as the sum of the eigenvector centralities of adjacent nodes multiplied by a factor $1/\lambda$, one obtains

$$e_i = \frac{1}{\lambda} \sum_{j \in \mathcal{V}} A_{ij} e_j, \tag{4.10}$$

which is the eigenvector problem associated to the adjacency matrix

$$\mathbf{A}\mathbf{e} = \lambda \mathbf{e}. \tag{4.11}$$

Accordingly, the centrality measure e_i is termed the *eigenvector centrality* [140, 27]. As a non-negative centrality measure is sought after, the eigenvector associated to the largest eigenvalue is to be chosen, according to the Perron-Frobenius theorem. The eigenvector centrality is a popularity measure, whose notable applications include the ranking of webpages in internet search engines.

4.1.3 Structure measures

Other than node-related measures, a graph can also be characterized using properties that capture its structure, most notably the local and global organization of links, the presence of communities and so on. While most of these features have effects on centrality measures, so that one may use, *e.g.*, the degree statistics to gain information onto the structure of a graph, more frequently a deeper insight is obtained through a rigorous characterization of structure properties, at the expense of added complexity and heavier computational burden.

Clustering coefficient The *clustering coefficient* c_i quantifies the local density of links around a given node. It does so by computing the probability that any two neighbours of the i-th node are themselves connected and, thus, that a connected triple of nodes is also a triangle (that is, the induced subgraph is complete) [220, 62]. It can be computed using

$$c_i = \frac{\sum_{j,m} A_{ij} A_{jm} A_{mi}}{k_i(k_i - 1)} \tag{4.12}$$

Assortativity In many real-world phenomena it is observed that connected entities share some properties and, in turn, that entities that share properties are more likely to be connected. In the framework of networks, the likelihood of similar (with respect to a certain property) nodes to be connected is termed *assortativity*. In its most basic form, the assortativity coefficient r is measured as the Pearson correlation coefficient of the degree of connected node pairs. Accordingly, it is a measure that describes the network as a whole, providing a single value $r \in [-1,1]$. In particular, a graph can be *assortative* if similar nodes are usually connected ($r > 0$) or disassortative if instead edges appear more frequently between dissimilar nodes ($r < 0$) [144].

Communities and modularity In the context of network science, communities are subsets of vertices that can be grouped together, especially because they present a relatively large amount of edges between themselves and a relatively small amount of edges connecting them with the rest of the network. The appearance and structure of communities have a pivotal role in networks, mostly because they bound the interaction between nodes to a subset of the whole network [74]. The key metric used for the measurement of the goodness of a given graph partitioning is the *modularity* Q, which quantifies the fraction of edges that lie inside of a community with respect to the same number if edges were disposed at random. Its value is

$$Q = \frac{1}{2K} \left[A_{ij} - \frac{k_i k_j}{2K} \right] \delta_{c(i),c(j)} \in [0,1], \tag{4.13}$$

where $k_i k_j / 2K$ is the expected number of links if a random distribution is expected and $\delta_{c(i),c(j)}$ is equal to one if vertices i and j belong to the same community and zero otherwise. We note that the modularity definition can be extended to weighted and directed networks, using

$$Q' = \frac{1}{m}\left[W_{ij} - \frac{s_i^I s_j^O}{m}\right]\delta_{c(i),c(j)}, \tag{4.14}$$

with $m = \sum_{ij} W_{ij}$ being the sum of all network weights [118]. We finally remark that the modularity of a whole graph can be split into the contribution of each k-th community, *i.e.* $Q = \sum_k q_k$, with q_k obtained from equation 4.13 restricting the sum to nodes belonging only to the k-th community.

While the modularity provides a way to evaluate the goodness of any partitioning imposed to a network, it does not provide a way to find the optimal partitioning. To do so, one must find a way to systematically create partitions and evaluate their modularity, then choosing the one with the largest modularity. Evaluating all possible ways to partition a network is impossible for even small graph sizes. Instead, a common approach relies on progressively eliminating key edges in order to create disconnected components that are treated as communities [141, 138, 139]. In particular, the betweenness of edges emerges as an useful metric in this context. Indeed, one aims to eliminate the edges that connect nodes belonging to different communities, in order to create disconnected components, which may be identified analytically [209]. If a network has a modular structure (that is, a community structure is clearly identifiable), such edges host a large number of shortest paths since they are the only way of communication between distinct communities. Accordingly, their removal isolate communities. The algorithm is as follows:

1. the betweenness centrality of all edges is computed.
2. the edge with the largest value of B_{ij} is removed
3. disconnected components, if present, are identified and taken as partitions of the graph
4. the modularity Q of the complete network (with no edge removed) is computed using the partitioning from the previous step
5. the betweenness centrality is recomputed and steps 2-5 are repeated until no edge remains
6. the partitioning that maximizes the modularity is chosen

We note that the recomputation of the edge betweenness at each step, while costly, is necessary to ensure that the optimal partitioning is found. A similar procedure can be adapted to weighted and directed networks, especially if network weights indicate the importance of a connection (and not, conversely, a cost measure). When identifying connected components in directed networks, moreover, one may distinguish between *weakly* connected components, *i.e.*, components in which a path exists between any two edges disregarding its direction, and *strongly* connected components in which a bidirectional path exists between all node pairs.

Another method of community identification stems from the definition of the *combinatorial Laplacian matrix* $\mathbf{\Lambda}$, which is

$$\Lambda_{ij} = \begin{cases} k_i \text{ if } i = j, \\ -1 \text{ if } i \neq j \ \wedge \ e_{ij} \in \mathcal{E} \\ 0 \text{ otherwise} \end{cases} \tag{4.15}$$

The definition of the Laplacian matrix can also be extended to directed graphs with

$$\Lambda_{ij} = \begin{cases} k_i^I + k_i^O \text{ if } i = j, \\ -1 \text{ if } i \neq j \ \wedge \ e_{ij} \in \mathcal{E} \\ -1 \text{ if } i \neq j \ \wedge \ e_{ji} \in \mathcal{E} \\ -2 \text{ if } i \neq j \ \wedge \ e_{ij} \in \mathcal{E} \ \wedge \ e_{ji} \in \mathcal{E} \\ 0 \text{ otherwise.} \end{cases} \tag{4.16}$$

In any case, the Laplacian matrix is symmetric and semi-definite positive [26]. The community properties of the graph are closely related to the spectral properties of $\mathbf{\Lambda}$. Let $\lambda_1 < \ldots \lambda_n \in \mathbb{R}$ be the eigenvalues of $\mathbf{\Lambda}$. If a graph is connected (or strongly connected for directed graphs), then only $\lambda_1 = 0$, while $\lambda_2, \ldots, \lambda_n > 0$. The first non-trivial eigenvalue is instead closely related to the possibility of partitioning the graph. Indeed, its magnitude is an indication of how hard it is to distinguish separate communities. Furthermore, the associated eigenvector $\mathbf{v}_2$ will provide information regarding which nodes can be grouped together [51]. Indeed, if one is able to find a criterion to group the components of $\mathbf{v}_2$, then this will lead to a grouping of nodes into communities, as each i-th component of the leading non-trivial eigenvector of $\mathbf{\Lambda}$ corresponds to vertex v_i of the graph.

Motifs Large networks appear, in general, complex due to their size and the non-triviality of the relationships between nodes. Still, when looking in detail at the behaviour of small subsets of nodes, one may find that certain patterns appear repeated. *Motifs* are simple interactions entertained by subsets of nodes that appear with statistically significant frequency and are relevant, through their individual contribution, to the processes described by the network as a whole [3, 192]. More specifically, motifs are subgraphs that appear more frequently than in the appropriate null model of the examined graph. Search algorithms for motifs are in general computationally expensive and involve a depth-first search that examines all subgraphs of fixed size contained in a network [221]. Furthermore, the definition of an appropriate null model is not always straightforward, so that the relative frequency of motifs must be used instead of their relevance with respect to a random graph.

4.2 Applications to fluid dynamics

Networks appear suitable to represent, analyse and model the interactions taking place in complex dynamical systems. The application to fluid flows arises naturally, as one may think of a turbulent flow as the result of the space- and time-dependent interaction of a multitude of simple units, be it points in the flow domain or advected particles [86, 203]. Moreover, the insightful methods of analysis provided by graph theory allow the exploitation of the wealth of data produced by simulation and experiments with ever-growing resolution and detail to an extent which goes beyond usual approaches, such as statistical analysis.

Because of this, several aspect of turbulent and transitional flows have been analysed through the application of network theory. The general approach is the following: one first needs to find a suitable mapping of fluid data into a sets of nodes and their mutual interactions. After that, network metrics are correlated to known fluid properties and further insight is extracted.

Flow data can be mapped into networks starting from different forms. The most important kinds of flow data in this regard are Lagrangian trajectories, time-series and spatial data. In the following, a brief review of all three approaches will be given.

4.2.1 Lagrangian trajectories

A first possibility when transposing Lagrangian trajectories into a network-like sets of interactions is to use a proximity-based criteria to detect a relationship between particles. In this case, a node in the network corresponds to single advected particles or sets of them, and a link is established when one or more particles from different nodes come at a distance lower than a certain threshold. Furthermore, if nodes are comprised of more than one particle, a weight can be assigned to each link, corresponding to the number of particles in close proximity. This approach has been applied to geophysical, two-dimensional flows, and to fully developed wall-bounded turbulence [155, 174, 173, 92, 8]. This method yields a reduced-order representation of particle motion and is a natural framework to study mixing, especially in complex flows where other measures may fail. Still, care must be ensued when selecting the threshold, as a small threshold value limits the number of particle pairs that come sufficiently close to each other and thus the resolution of the method. On the other hand, features of particle motion at scales smaller than the threshold are neglected by the network representation and their removal must be taken into account.

Proximity-based criteria have been extended to include time-averaged measures of distance between tracers [80]. The resulting networks allow to identify coherent sets, through the identification of communities based on spectral clustering using the graph Laplacian $\mathbf{\Lambda}$ or other clustering means [214, 215, 190, 191]. Additionally, one may consider the similarity of trajectories without regard for their actual distance [189]

Another possibility stems from the definition of the Lagrangian flow map. The trajectories described in equation 2.12 can be equivalently represented as orbits of a dynamical system defined on a flow domain Ω

$$\Phi_{t_0}^{\tau}(\mathbf{x}_0) = \mathbf{X}(\mathbf{x}_0, t_0 + \tau) : \Omega \times \mathbb{R}^+ \to \Omega, \tag{4.17}$$

which maps the starting position of particles at t_0 into that after a time τ. If the domain Ω is divided into a set of partitions

$$L_i,\ i = 0 \dots N : \cup_i L_i = \Omega \text{ and } L_i \cap L_j = \emptyset \quad \forall i, j \tag{4.18}$$

then the flow map can be discretized. In particular, if one defines a measure for the amount of fluid contained in each partition $m(L_i)$, a discrete state $\{s_i = m(L_i)\}$ of the system can be computed at any time. The transition from the discrete state at $t = t_0$ to the state at $t = t_0 + \tau$ is measured as

$$P_{ij}(t_0, \tau) = \frac{m\left(L_i \cap \Phi_{t_0+\tau}^{-\tau}(L_j)\right)}{m(L_i)}. \tag{4.19}$$

Each entry i, j of $\mathbf{P}$ is the probability that fluid contained in L_i at $t = t_0$ will be found in L_j at $t = t_0 + \tau$ [70]. If the underlying flow respects continuity, the transition matrix is row-stochastic (the sum of all rows is one) and is thus assimilable to a Markov chain.

In practice, the transition matrix can be built from discrete trajectory data rather than from the flow map by defining $m(L_i)$ as the number of Lagrangian particles found in L_i at any time, and by counting the number of Lagrangian particles that move from partition L_i to partition L_j in the considered time frame.

Finally, one may take the transition matrix $\mathbf{P}$ as a network weight matrix and thus define a graph where the nodes represent fixed domain partitions and the edges are the fluid exchanges between these partitions, with weights corresponding to the intensity of the latter.

This approach has been extensively applied to the analysis of geophysical flows, especially with respect to oceanic currents where Lagrangian tracers are either numerically integrated from velocity fields or are obtained from buoy data [72, 71, 48, 193, 170]. In particular, the spectral properties of the transition matrix have been used to identify invariant sets, *i.e.*, regions of space that exchange low amounts of fluid with the rest of the domain. In this sense, networks based on the transition probability matrix appear suitable to identify coherent structures, although a lot depends on the resolution employed to discretize the flow domain.

4.2.2 Time-series analysis

In the context of fluid flows, time-series represent the evolution of certain flow variables, *e.g.* the local Eulerian velocity. Starting from a time-series, one of the approaches that can be used to obtain a network representation is to employ the notion of recurrence [53, 233, 52]. In general, recurrence is a property of the state of dynamical systems, which occurs when the trajectories of the system come in close proximity (with respect to a certain metric) to previous states, a concept that is closely correlated to that of a Poincaré map [180].

The state space described by a single time-series is trivial and does not usually lead to significant insight on the underlying phenomena. [89] used the three-dimensional time-series of the position of tracers to compute recurrence properties starting from sparse Lagrangian data, revealing and quantifying dominant flow scales. Another approach involves state space reconstruction via *embedding* [122].

The most prominent embedding method is time-delay embedding, which allows state space reconstruction by combining k subsequent steps of the time series (with or without delay between them) into a state space vector. Takens's theorem guarantees that if the embedding dimension k is at least twice the dimension of the attracting set in the considered system, then the attractor itself may be reconstructed using only the observation obtained through the time-series [205]. Nonetheless, the dimensional complexity of the turbulent attractor makes somewhat difficult to formulate a clear choice of the embedding dimension.

Another important choice in the definition of recurrent networks is the choice of a threshold. It is indeed possible to assign a fixed number of neighbours to each node of the network, thus creating a k-nearest neighbour recurrence network, although this may include distant connections if the local state space has a low density and, conversely, may exclude some relevant connection. The natural choice in the context of physical system is therefore to assign a fixed threshold ϵ (which accordingly defines an ϵ-recurrence network), possibly after analysing the distribution of state space distances [106]. Applications to fluid dynamics include the study of the instability in combustion phenomena, the identification of coherent sets of tracers and transition phenomena in stratified flows [102, 75, 201, 207, 89, 73].

Another approach, which has gained widespread adoption in the analysis of fluid flows, is that of the *visibility graph* [114]. The visibility graph approach defines a graph assigning each individual time-step to a node and setting a link between nodes according to a visibility criterion. More specifically, the edge e_{ij} between nodes corresponding to time-steps t_i and t_j are connected if and only if

$$u(t_k) \leq (u(t_j) - u(t_i)) \frac{t_k - t_i}{t_j - t_i}, \quad \forall k = i, \dots, j, \tag{4.20}$$

where $i < j$ without loss of generality. The procedure according to which links are formed is shown schematically in figure 4.2.

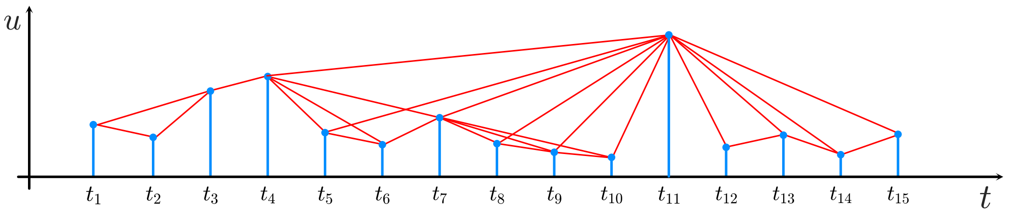

Figure 4.2: Construction of a simple visibility graph starting from a time-series. Red lines indicate active links.

Edges in the visibility graph are created if an uninterrupted straight line can be traced between the corresponding data points, which follows from the local convexity of the data. A possible variation is that of an *horizontal visibility graph*, which is based on a slightly simplified criterion [113]. The visibility graph approach does not require, differently from other methods, the definition of *a priori* parameters. It is also invariant to affine transformation of the time-series, so that time-series with similar geometrical structure but different mean and standard deviation will map into the same network. Most notably, the visibility graph descends purely from the geometrical appearance of the time-series and is not directly related to the processes underlying to it. As such, while its application may provide insight on the structure of the time-series, the inference of results on the underlying processes requires further interpretation.

The visibility graph has been applied to several fluid dynamics cases. Notably, distinguishing between forward- and backward-in-time contributions allow for the quantification of temporal irreversibility, which was linked to the presence of large-scale coherent motions in turbulent flows [115, 93]. The application to experimental data allowed to classify time-series feature and provide an identification of intermittent phenomena [45, 87]. Also, the modulation applied from large to small flow scales in wall-bounded flows has been studied [90, 88]. More complex settings, such as magnetohydrodynamics flows and heated jets, have been subject to visibility graph analysis [40, 41, 145]. Finally, the visibility graph can be computed from a time-series with fast algorithms (in $\mathcal{O}(N \log N)$ time, N being the number of nodes), which makes it suitable for use in large datasets [116].

4.2.3 Spatial data

Finally, the definition of a graph may come from assigning different points in the flow domain to network nodes and defining links between them following the presence of a statistical correlation or another kind of relation between them. Accordingly, one defines a *spatial network* in which nodes have also a position and therefore mutual distances.

Networks based on climate data usually belong to this category, as one can exploit the correlations between data, even at long spatial distances, to show the global interdependence of weather phenomena [186, 50]. Correlations between flow variables have also been used in the study of turbulence, both isotropic and wall-bounded, revealing non-local relationships between flow features [185, 91].

Other than statistical correlations, also link definitions based on the vortical properties of the flow and the resulting induced velocities have been explored [204]. This approach has been applied to two-dimensional isotropic turbulence, showing that there are preferential zones in which flow control can be exerted, with the particular goal of modulating and controlling turbulence [224].

Chapter 5

Transport network analysis of channel flow mixing

Some of the contents presented in this Chapter have been previously published. Below are provided the references:

D. Perrone, J.G.M Kuerten, L. Ridolfi, S. Scarsoglio, "Wall-induced anisotropy effects on turbulent mixing in channel flow: A network-based analysis", in *Phys. Rev. E* **102**, 043109 (2020)

D. Perrone, J.G.M Kuerten, L. Ridolfi, S. Scarsoglio, "Network analysis of Reynolds number scaling in wall-bounded Lagrangian mixing", in *Phys. Rev. Fluids* **6**, 124501 (2021)

5.1 Rationale

In this chapter, the application of the transition matrix approach, *i.e.*, the *transport network*, first introduced in section 4.2.1 to tracer data from direct numerical simulations of channel flow will be treated.

The goal of this work is twofold: from the methodological standpoint, we aim to define a new approach to study mixing problems in complex settings (in this case the complexity arises from the chaotic nature of turbulence). The necessity for this arises from the ever-growing availability of high-resolution data from simulation and experiments, which in turn makes important to exploit analysis techniques that are able to provide in-depth insight into the processes underlying to the data itself. From the physical standpoints, instead, we aim to obtain a quantification of mixing in channel flow, with particular regard to coherent structures of particle motion and their influence on the overall mixing.

To achieve these goals we first perform direct numerical simulations (DNS) of channel flow at varying Reynolds numbers Re_τ ranging from 180 to 950. Then, we split the channel domain into wall-normal levels which we take as the partitions of the transition matrix approach. We measure the exchange of fluid between these partitions by integrating the trajectories of Lagrangian tracers, therefore obtaining a time-dependent transition matrix. In this way, the main focus is on wall-normal mixing. We repeat this process with several uncorrelated batches of particles, in order to obtain a statistically significant representation of mixing in the channel.

Starting from the network representation of particle motion, we obtain results on the Reynolds number scaling of dispersion, which is tightly correlated to the degree of nodes. We also are able to identify sections of the channel domain in which particles remain trapped and the underlying coherent motions that contribute to the trapping.

In the following, section 5.2 contains an overview of the methods employed, section 5.3 shows the results obtained and section 5.4 provides a discussion and an interpretation of the results.

5.2 Methods

The Lagrangian data were obtained through the numerical integration of trajectories of tracer particles using the Eulerian velocity field from a direct numerical simulation of turbulent channel flow. The Navier-Stokes equations were solved with the pseudospectral method introduced in Chapter 3, making use of Fourier discretization along the periodic directions x and z and the Chebyshev-τ approach along the wall-normal direction y. The simulations were performed at five different Reynolds numbers $\mathrm{Re}_\tau = \delta u_\tau/\nu = 180, 265, 395, 590, 950$. The parameters used for the five simulations, including the box size $L_x \times L_y \times L_z$, the number of polynomials employed in the discretization $N_x \times N_y \times N_z$ and the time-step in outer units Δt are given in table 5.1.

Table 5.1: Main parameters for the direct numerical simulations at five Reynolds numbers Re_τ: domain size $L_x \times L_y \times L_z$, number of polynomials used for the simulation $N_x \times N_y \times N_z$ and time step Δt

Re_τ	$L_x \times L_y \times L_z$	$N_x \times N_y \times N_z$	Δt
950	$2\pi\delta \times 2\delta \times \pi\delta$	$768 \times 385 \times 768$	$1 \cdot 10^{-4}$
590	$2\pi\delta \times 2\delta \times \pi\delta$	$768 \times 385 \times 768$	$1.25 \cdot 10^{-4}$
395	$2\pi\delta \times 2\delta \times \pi\delta$	$512 \times 257 \times 512$	$1.5 \cdot 10^{-4}$
265	$2\pi\delta \times 2\delta \times \pi\delta$	$512 \times 257 \times 512$	$2 \cdot 10^{-4}$
180	$4\pi\delta \times 2\delta \times 4\pi\delta/3$	$384 \times 193 \times 192$	$2.5 \cdot 10^{-4}$

In order to obtain the partitions needed for the transport network, we divide the channel into $N_l = 100$ equal levels along the y direction, each with thickness equal to $2\delta/N_l$. Particles are therefore released in an $N_l \times 100$ grid located at $x = 0$, so that 100 particles are located in each level. The grid has a spacing of $\Delta y = 2\delta/N_l$ along y direction and $L_z/100$ along the spanwise direction. Accordingly, $N_p = 10000$ particles are released. All trajectories are integrated for a duration of $T = 10$ in outer units, so that the entire transient phase of the mixing process (before the asymptotic Taylor regime) is considered.

In order to construct the network, we take into account the previously defined levels and map the set of trajectories $\mathbf{x}(\mathbf{x}_0, t)$ into a sequence of traversed levels. Accordingly, we transform the continuous evolution of particle positions into a set of discrete states $\mathbf{s} \in \mathbb{R}^{N_l}$, with each entry s_i equal to the the number of particles contained in the i-th level. The transition matrix $\mathbf{P}(t_0, \tau)$ is built following the procedure indicated in 4.2.1. Each entry P_{ij} of the matrix is defined as the probability that a particle, located in level i at $t = t_0$, is situated in level j at $t = t_0 + \tau$. Instead of computing the flow map Φ directly, we approximate each entry by the fraction of the particles released in level i at time t_0 that is in level j at the subsequent time $t_0 + \tau$. The formula used is

$$P(t_0, \tau)_{ij} = \frac{N_{i \to j}(t_0, \tau)}{N_i(t_0)}, \tag{5.1}$$

where $N_{i \to j}(t_0, \tau)$ is the number of particles that after a delay τ have moved from level i to j, while N_i is the number of particles originally located in level i (which is always 100). Because of continuity and the fact that particles cannot leave the domain, the sum of all rows of the transition matrix is one (meaning that all particles released from each level can be tracked into another level). Instead, the sum of columns of $\mathbf{P}$ is not one and is instead the number of particles contained in the i-th level at time $t_0 + \tau$ (normalized by $N_i(t_0) = 100$).

Formally, $\mathbf{P}(t_0, \tau)$ is the transition process from the state $\mathbf{s}_{t_0}$ of the system at the release time to the state $\mathbf{s}_{t_0+\tau}$ after a delay τ. In particular, for all delays τ it holds that $\mathbf{s}_{t_0+\tau} = \mathbf{P}^{\intercal}(t_0, \tau)\mathbf{s}_{t_0}$, where the superscript $^{\intercal}$ denotes matrix transposition. Starting from the definition of the transition probability matrix, one can define a network by assigning each level to a node and creating weighted links between the generic i and j nodes according to the entries P_ij. In this way, a network with a weight matrix $\mathbf{W}$ equal to $\mathbf{P}(t_0, \tau)$ is created for each delay τ. We keep track of the diagonal terms (the self-loops of the network, *i.e.*, particles that after a delay τ are still in the original level or have returned back to it), although they are not used in the formal network definition.

The adjacency matrix of the network, constructed starting from its definition in equation 4.1, gives information regarding the material connection between levels. In particular, each entry A_{ij} is nonzero if at least one tracer has moved from level i to j. The construction of the network and its adjacency matrix is depicted in figure 5.1, showing how individual tracers are binned into levels and the resulting adjacency matrix.

Since with the previously defined layout particles are initially confined to a single

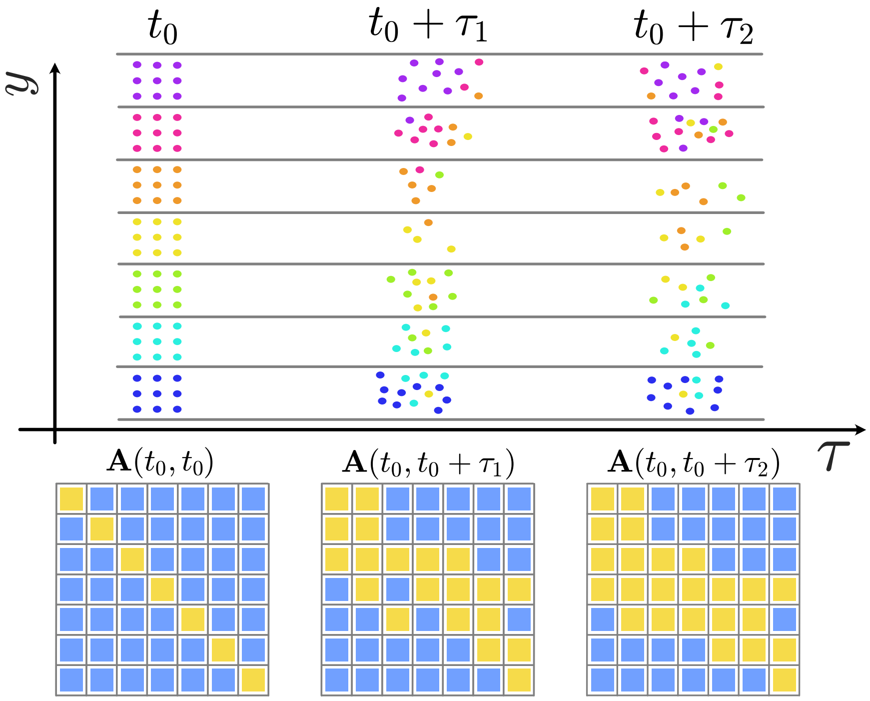

Figure 5.1: Construction of the transport network, with a schematic depiction of the motion of tracers between levels and of the corresponding network adjacency matrices. Particles are identified through a color-coding according to their release level and their trajectories are integrated. For each time step after release, a network can be obtained, of which the adjacency matrix $\mathbf{A}$ is shown below (with nonzero entries in yellow).

location along the streamwise direction x, they are subject to an instantaneous turbulent velocity field. Accordingly, to evaluate the influence of the instantaneous velocity field on the initial dispersion of particles and on the behaviour of the transport network, we release $N_b = 61$ subsequent sets of particles, all comprising of the same grid of tracers, for each Reynolds number. The release of batches is separate by an amount of type which depends on the Reynolds number, that is, a time larger than the Lagrangian integral timescale at the center of the channel (where it is the largest). In this way, we guarantee that separate batches are uncorrelated.

Whenever each batch b of particles is inserted into the channel and the trajectories of its particles are integrated, we build a transport network for each delay τ by defining its weight matrix $\mathbf{W}(b, \tau)$ (in the following we will omit the argument t_0, as it is fixed to zero in all cases). We therefore obtain a succession of weight matrices covering the entire evolution of tracer dispersion in the channel. Repeating this procedure for all realizations yields N_b succession of matrices, each pertaining to a different batch of particles with its own peculiar features due to the different initial conditions.

Different realization of the transport network evolution are uncorrelated, as they stem from uncorrelated sets of particle trajectories. An ensemble analysis of network properties can be carried out by averaging the properties of different realizations. As we deal mostly with node-related quantities (which depend on the node index i, on the delay τ and on the realization b), it is useful to introduce a notation for the averaging across realizations, and a separate notation for the averaging and other statistical properties along the wall-normal direction i. Starting from the generic quantity $q_i(b,\tau)$, we define the y-average $q^{(n)}(b,\tau) = \sum_{i=1}^{N_l} q_i(b,\tau)/N_l$ and an ensemble-average $\langle q_i(b,\tau)\rangle = \sum_{b=1}^{N_b} q_i(b,\tau)/N_b$. The y-average $\bullet^{(n)}$ and the ensemble average $\langle\bullet\rangle$ are illustrated in figure 5.2.

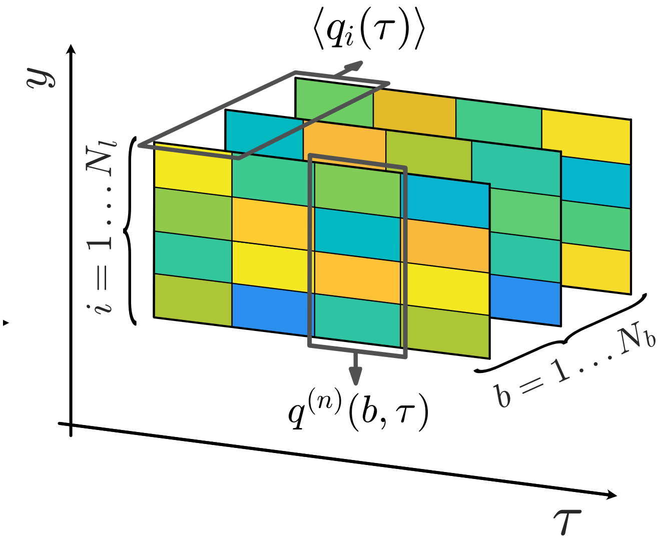

Figure 5.2: Schematic of the two kinds of averaging used in the following. A generic quantity $q_i(b,\tau)$, associated to the i-th level and b-th batch, can be averaged along y or across realizations.

5.3 Results

5.3.1 Transport network evolution

First, let us analyse the qualitative evolution of the transport network obtained from a single realization at $\mathrm{Re}_\tau = 950$, in order to gain understanding of its main features. Shortly after release, particles have only travelled a short distance along the wall-normal direction, as dispersion is dominated by streamwise advection. As the delay τ increases, tracers drift away from their release location driven by the diffusive action of turbulence and new links are formed with growing range. We note that, since trajectories are well-resolved in time and due to the coarse dimension of the levels inside the channel, it is not possible for a tracer to cross a level without its position being recorded in at least one state. After very long times, tracers lose memory of their starting position and become thoroughly mixed across the channel.

The evolution of the network weight matrix provides a full description of the vertical motion of tracers, albeit in a discrete setting. Figure 5.3(a) shows $\mathbf{W}$ graphically, together with the instantaneous distribution of tracers (which are color-coded to show their starting level). At $\tau^+ = 100$ (first row of the figure) there is no evidence of short mixing, and indeed only links between close levels are active. Accordingly, only the entries of the network weight matrix close to the diagonal are different from zero. New connections appear as time passes and the mixing of particles goes on. At intermediate times ($\tau^+ = 500$ and $\tau^+ = 3990$, second and third row of the figure) the activation of links further away from the diagonal took place, although the strongest connections are still found between nearby nodes. In particular, even at quite long times, the links between levels that are both located close to the solid boundary have larger weight, indicating that particles released close to the channel walls employ more time to diffuse towards the central region. Finally, at $\tau^+ = 15200$ (last row of the figure) all particles are thoroughly mixed and connections appear to be randomly distributed. The random appearance of connections follows the loss of memory by particles regarding their release location, which in turn arises from being at a time much longer the the integral timescale. If the normalization factor N_i in equation 5.1 is neglected, then weights are integer and can be modelled by a Poisson distribution with mean $\lambda = N_p/(N_l^2) = 1$ (the number of particles divided by the number of possible links)

$$f(W_{ij};\lambda) = \frac{\lambda^{W_{ij}}\mathrm{e}^{-\lambda}}{W_{ij}!} \tag{5.2}$$

The agreement between the weight distribution at $\tau^+ = 15200$ and the Poisson distribution 5.2 is shown in figure 5.3(b) and was also tested using the Kolmogorov-Smirnov test.

5.3.2 Degree centrality

During the ballistic regime, *i.e.*, when the time is much shorter than the Lagrangian integral timescale T_L defined in equation 2.14, all particles released from the same (wall-normal) location are still confined in the neighbourhood of that location and also their velocity is strongly correlated to that at release. Indeed, they are in the ballistic regime, during which their motion is solely determined by their initial velocity. In particular, the variance $\sigma_y^2(y_0,\tau)$ of their wall-normal position is

$$\sigma_y^2(y_0,\tau) = \tau^2\sigma_v^2(y_0,0), \tag{5.3}$$

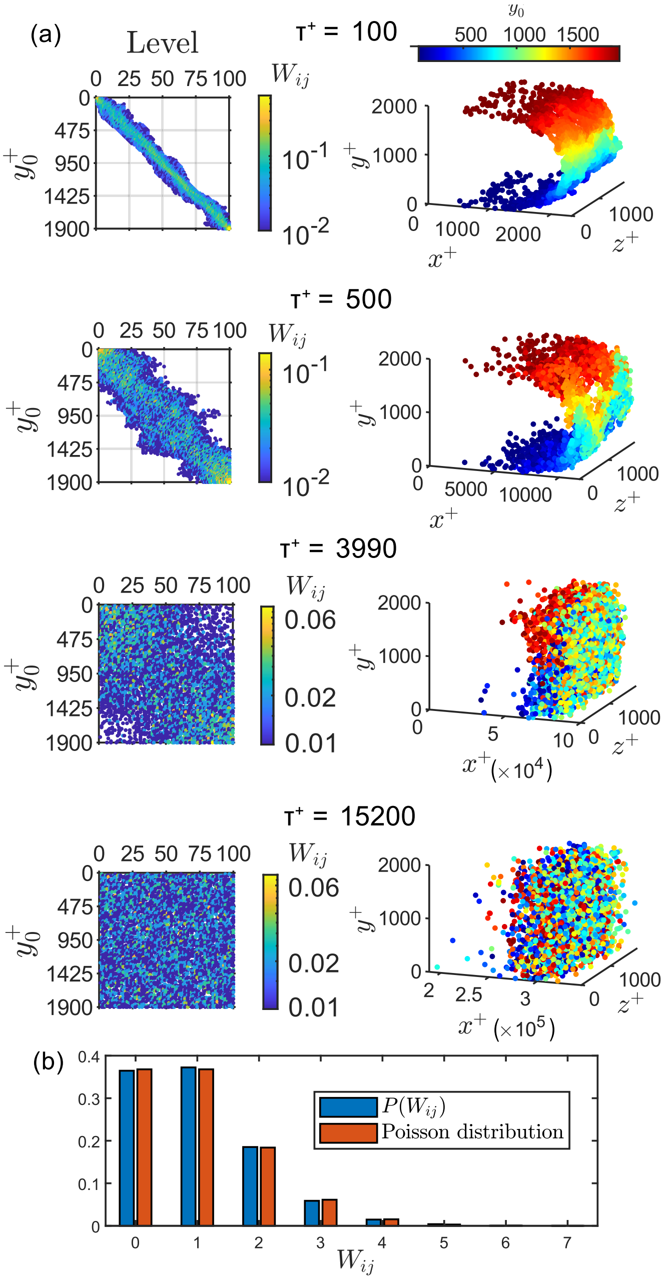

Figure 5.3: (a) Evolution of the network weight matrix for a single realization at $\mathrm{Re}_\tau = 950$ and corresponding position of tracers, with their starting location color-coded. b) The distribution of the weights W_{ij} at $\tau^+ = 1.52 \cdot 10^4$ compared to the Poisson distribution $\lambda = 1$

with $\sigma_v^2(y_0,0) = \overline{v_y v_y}(y_0,0)$ being the wall-normal velocity variance (shown for all Reynolds numbers in figure 5.4(c)). Confirmation of the ballistic regime defined in

5.3 is shown in figure 5.4(a)

In the discrete approach afforded by the transport network, the dispersion of sets of particles is quantifiable by measuring the number of other levels which become connected by the motion of these particles as a function of τ. Conversely, mixing into the i-th level can be quantified by measuring the number of release levels whose particles are present in level i at any time τ, which is a measure of backward-in-time dispersion. This quantification is done by measuring the number of outgoing, or ingoing, connections out and in of each node, that is, the outgoing degree k_i^O or the ingoing degree k_i^I.

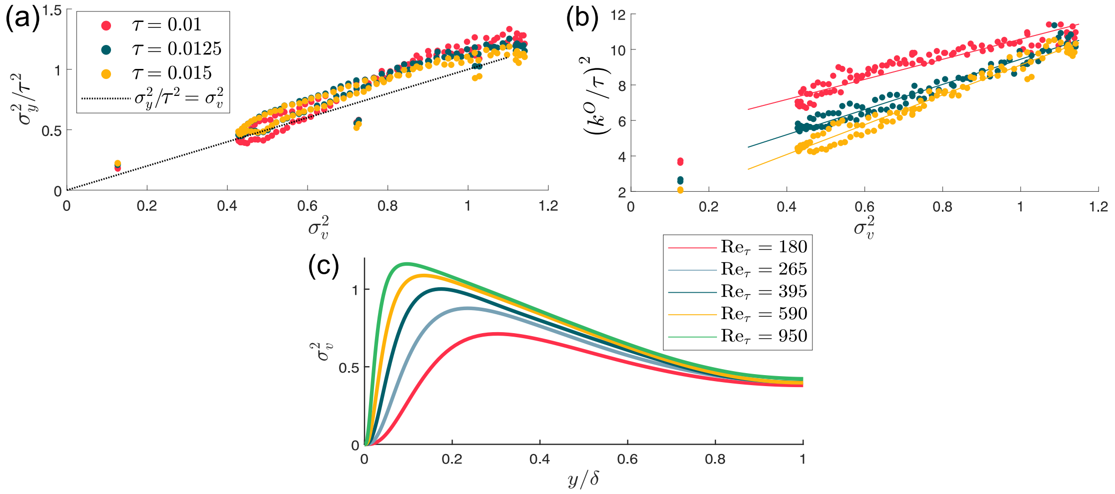

Figure 5.4: (a) Variance of the position of particles released from each node, divided by τ^2, versus the velocity variance at the release location, $\mathrm{Re}_\tau = 950$. (b) Squared outgoing degree $(k^O)^2$, ensemble-averaged and divided by τ^2, versus the velocity variance. (c) Wall-normal velocity variance profiles at all Reynolds numbers

The degree centrality for $\tau \ll T_L$ is determined uniquely by the local velocity field, in analogy to the behaviour of the position variance. Figure 5.4(b) shows how the squared outgoing degree is proportional, at different times, to the local wall-normal velocity variance. Differently to the y position variance, instead, proportionality to τ^2 is not achieved. The cause of this different behaviour is to be traced in the different sampling of the wall-normal amplitude of particle clouds. The position variance varies continuously, while the degree increases only in discrete steps. Furthermore, the difference between the two sampling approaches is wider for short times, when the distribution is narrower.

As the error between the two measures appears to decrease at longer times, we expect the two measures to be in good agreement for delays τ past the ballistic regime. Accordingly, we use the degree centrality to quantify the extent of dispersion and mixing between different levels of the channel at once.

We now aim to analyse the behaviour of the degree at longer times, in order to characterize dispersion. The inset of figure 5.5(a) shows the growth of the y- and ensemble-averaged degree $\langle k^{(n)}(\tau)$, which grows monotonically with τ. The growth of the mean degree is caused by the transition of the state of the channel from an ordered state, in which all particles are located close to their origin levels, to a fully mixed one. After some time, the rate of entrance and exit of tracers in each level reaches a balance, allowing the mean degree to achieve a stationary value. Recalling that at the fully mixed stage weights are Poisson distributed, also the value of the mean degree asymptote can be analytically determined as the expected number of nonzero weights from equation 5.2, that is,

$$\lim_{\tau\to\infty} \langle k^{(n)} \rangle = 1 - 1/\mathrm{e} \approx 0.63. \tag{5.4}$$

We also note that the mean outgoing and ingoing degree must be equal, since the total (and, thus, the average) number of connections leaving a node must enter other nodes, as tracers cannot escape the domain.

The degree centrality is also able to quantify the extent and spatial inhomogeneity of mixing across different levels of the channel and as a function of time. In particular, in figure 5.5(a), we show the fluctuation of the outgoing degree around its y-average, $k_i^{'}(b,\tau) = k_i(b,\tau) - k^{(n)}(b,\tau)$, ensemble-averaged at $\mathrm{Re}_\tau = 950$. By filtering out the average growth of the degree, we highlight the different properties of dispersion depending on y. Near the walls, the fluctuation of the degree is less than zero, indicating that in that region tracers disperse more slowly than in other parts of the channel. Furthermore, the area with negative fluctuation expands over time proportionally to $\sqrt{\tau}$ for $\tau < 1$, after which it occupies around one quarter of the channel height (for each wall) until the end of the transient phase (not shown in the plot, where fluctuations become negligible). The regions in which the fluctuation of the outgoing degree is positive indicate faster than average dispersion. Initially, two peaks of the fluctuation are present very close to the walls, which join in the middle of the channel at $\tau \approx 0.5$.

The dependency of the degree on the wall-normal coordinate also varies with time. As an example, we follow the ensemble averaged fluctuation of the degree $\langle k_i^{'}(\tau)\rangle$ of a level located at $y = \delta/4$ (marked in red in figure 5.5(a)). Its value is initially larger than zero, then decreases and becomes negative at around $\tau = 0.4$. After that, it remains negative until the transient phase ends. At that location the variance of the wall-normal component of the velocity is the highest of the entire channel, and yet the intensity of mixing shifts over time, also becoming less intense than in the rest of the channel.

After some time, particles that have moved towards the wall now diffuse more slowly than the average, thus causing a decrease of $\langle k_i^{'}(\tau)\rangle$ for the level considered. At the contrary, particles that are released around the center of the domain after some time reach regions of the channel with more intense wall-normal velocity fluctuations (which are, ultimately, the main driver for dispersion), so that the fluctuation of the degree for the levels close to the center grows with time.

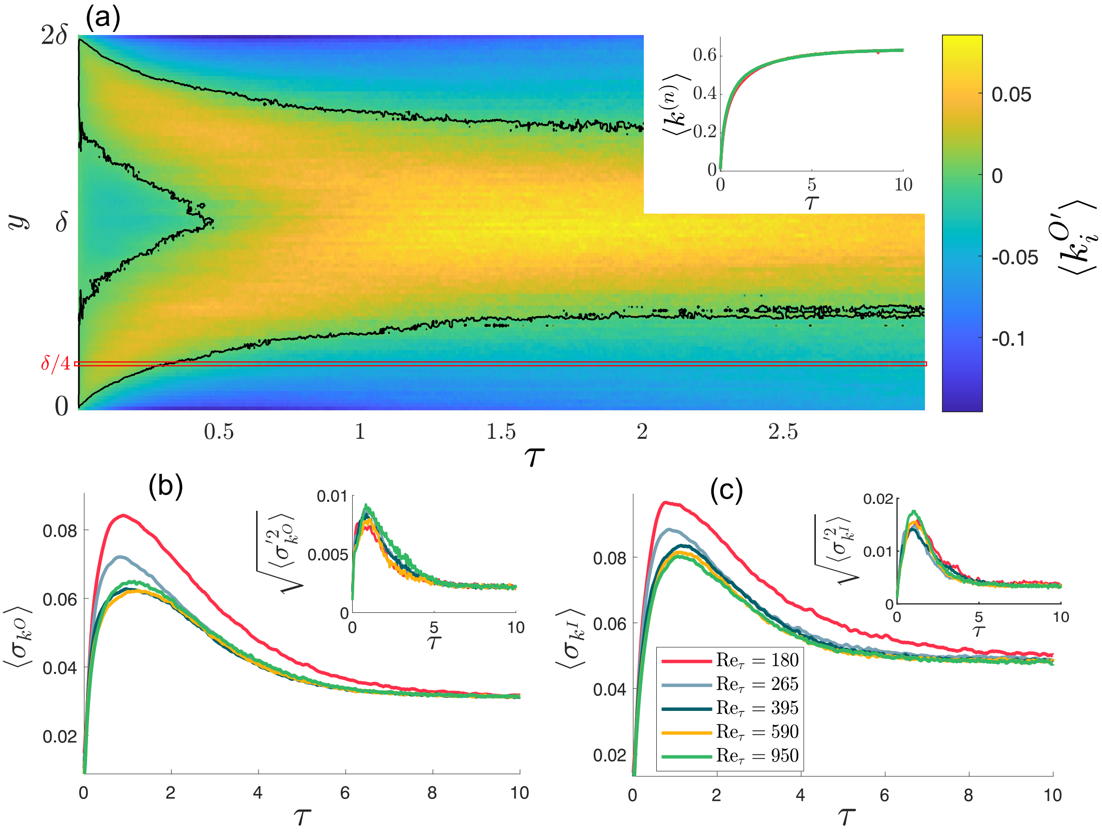

Figure 5.5: (a) Fluctuation of the outgoing degree around its y-average, ensemble-averaged at $\mathrm{Re}_\tau = 950$; the black contour shows $\langle k_i' \rangle = 0$. The inset shows the mean degree (across all nodes and realizations) at all five Reynolds numbers. Panels (b) and (c) show the ensemble-averaged standard deviation $\langle \sigma_k \rangle$ of the outgoing and ingoing degree, respectively. The insets show the standard deviation across different realizations of σ_k, *i.e.* $\langle \sigma_k'^2 \rangle^{1/2} = \langle (\sigma_k - \langle \sigma_k \rangle)^2 \rangle^{1/2}$.

To effectively compare the behaviour of the degree fluctuations at different Reynolds number, we calculate their root mean square

$$\sigma_k(b,\tau) = \sqrt{\frac{1}{N_l} \sum_{i=1}^{N_l} \left(k_i'(b,\tau) \right)^2}, \tag{5.5}$$

which quantifies the spatial inhomogeneity of mixing inside the channel. Figures 5.5(b)-(c) show the ensemble averaged values of the root mean square of the degree, *i.e.* $\langle \sigma_{k^O}(\tau) \rangle$ and $\langle \sigma_{k^I}(\tau) \rangle$, for the outgoing and ingoing degree at varying Re_τ. Independently of the Reynolds number, a common trend is found. The standard deviations of the ingoing and outgoing degree grow rapidly, reach a peak at approximately $\tau = 1$ and then slowly decrease towards an asymptotic value, reflecting the appearance and merging of the peaks of the degree fluctuation previously shown.

The standard deviations of the degree for $\mathrm{Re}_\tau \geqslant 395$ are almost independent of the Reynolds number. A collapse of the spatial inhomogeneity of the degree is observed if outer units are used to normalize time. On the other hand, $\langle \sigma_k(\tau) \rangle$ at $\mathrm{Re}_\tau = 180$ and $\mathrm{Re}_\tau = 265$ are significantly higher during the entire transient phase for both the ingoing and outgoing degree, indicating higher inhomogeneity inside the channel. We confirmed the independence between realizations at $\mathrm{Re}_\tau = 180$ and 265 and those at higher Reynolds numbers by applying the Kruskal-Wallis test, while at the same time we confirmed that realizations at $\mathrm{Re}_\tau \geqslant 395$ are not independent [107]. The main cause for the increased inhomogeneity of the degree at $\mathrm{Re}_\tau = 180$ is to be found in the near wall region, where the fluctuations of the degree are larger (in absolute value) than at the higher Reynolds numbers.

While the ingoing and outgoing degree mostly show a similar qualitative behaviour, the spatial standard deviation of the ingoing degree has in general higher values than that of the outgoing degree. The larger standard deviation of the ingoing degree with respect to the outgoing degree is caused by the fact that the ingoing degree is higher than the outgoing degree near the center of the channel, while it is lower towards the boundaries.

As the ingoing and outgoing degree centralities are connected to dispersion of particles backward and forward in time, the difference between $\langle \sigma_{k^I} \rangle$ and $\langle \sigma_{k^O} \rangle$ indicates a temporal asymmetry in the dispersion process. The presence of temporal asymmetries in particle dispersion is linked to the irreversibility of turbulence and to the dissipative flux of energy from large to small flow scales. A relation for the difference between the backward and forward in time variance of particle positions, which, as was demonstrated in the beginning of this section, shares some similarities with the ingoing and outgoing degree, can be obtained for short times τ. In particular, retaining terms of order $\mathcal{O}(\tau^3)$ in equation 5.3 yields $\sigma_y^2(y_0, \tau) = \tau^2 \sigma_v^2(y_0, 0) + \overline{v_y a_y}(y_0, 0)\tau^3 + \mathcal{O}(\tau^4)$, where v_y and a_y are the wall-normal components of particle velocity and acceleration. The difference between backward and forward dispersion (negative and positive delay τ) is

$$\sigma_y^2(y_0, -\tau) - \sigma_y^2(y_0, \tau) = -2\overline{v_y a_y}(y_0, 0)\tau^3 + \mathcal{O}(\tau^5), \tag{5.6}$$

which quantifies the temporal asymmetry of the dispersion of a cloud of tracers released at a wall-normal coordinate y_0 when tracked forward and backward in time [164].

We computed the value of $-2\overline{v_y a_y}(y_0, 0)$ from simulation data and found that it is larger than zero near the center of the channel and negative at distances from the wall lesser than $\delta/2$ (except for the near-wall region, where particles moving towards the wall have to decelerate and thus $-2\overline{v_y a_y}(y_0, 0) > 0$); this agrees with the difference between the ingoing and outgoing degree, which at short times is negative at wall distances $y \lesssim \delta/2$ and positive elsewhere. We expect a similar correlation to hold also after the end of the ballistic regime.

Finally, the insets of figures 5.5(b) and 5.5(c) show the standard deviation across realizations of σ_k, defined as $\sqrt{\langle \sigma_k'^2 \rangle} = \sqrt{\langle (\sigma_k - \langle \sigma_k \rangle)^2 \rangle}$, both for the outgoing and ingoing degree. This quantity represents the variability due to the differences between different realizations of the spatial inhomogeneity of the diffusion process, as reported by the degree centrality. The Reynolds number does not seem to play a significant role here, meaning that the intra-Reynolds variability is independent of Re_τ and rather reflects solely on the variance observed on the initial condition of the flow and its subsequent, unique, evolution.

5.3.3 Eigenvector centrality

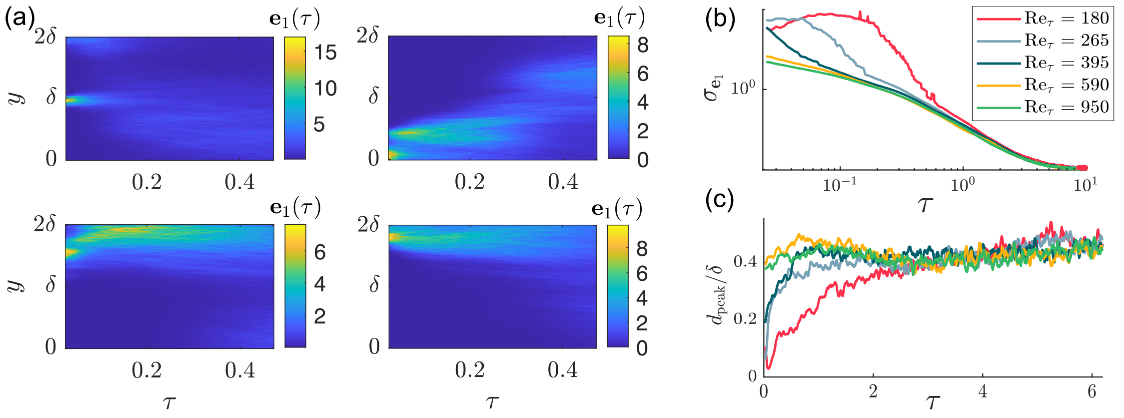

Figure 5.6: (a) Eigenvector centrality $\mathbf{e}_1(\tau)$ for four different realizations of the transport network evolution at $\mathrm{Re}_\tau = 950$. (b) Temporal behavior of the standard deviation of the node eigencentrality, averaged over realizations at the five Reynolds numbers considered. (c) Distance between the node with the highest eigenvector centrality and the nearest wall, averaged over realizations at the five Reynolds numbers.

To evaluate the cumulative effects of the flow field, we analyse the eigenvector $\mathbf{e}_1$ associated to the leading eigenvalue λ_1 of $\mathbf{W}^\intercal(\tau)$. The eigenvector $\mathbf{e}_1$ obtained from the transport network weight matrix represents the concentration along y that particles would attain if left indefinitely under the influence of the flow as represented by the network $\mathbf{W}(\tau)$ at a single time τ. In particular, the eigenvector $\mathbf{e}_1$ is the state of the system (*i.e.* the concentration of tracers) attained after infinite applications of the same process $\mathbf{W}(\tau)$ at a fixed time τ, which is unique and independent of the initial state. This measure is the eigenvector centrality of the transport network.

This can be shown by considering some properties of the transition probability matrix and, therefore, of the network here studied. Since in general the transport network is strongly connected, the network weight matrix $\mathbf{W}(\tau, b)$ is irreducible (in our case, having a reducible weight matrix would mean having the motion of particles confined to some subset of the domain, which is not the case). Also, since the weight matrix is row-stochastic (the sum of each row is one), Gershgorin's circle theorem prescribes that its leading eigenvalue is $\lambda_1 = 1$, while $|\lambda_k| < 1$ for $k > 1$. Considering that any initial state $\mathbf{s}(t_0)$ can be expressed in the eigenvector basis $\{\mathbf{e}_k\}$, n repeated application of the transition process yield a new state of the system, which can be expressed as

$$\left(\mathbf{W}^{\intercal}\right)^n \mathbf{s}(t_0) = \left(\mathbf{W}^{\intercal}\right)^n \sum_k c_k \mathbf{e}_k = \sum_k c_k \lambda_k^n \mathbf{e}_k = c_1 \mathbf{e}_1 + \mathcal{O}\left(\lambda_2^n\right), \tag{5.7}$$

which, for infinite applications, is

$$\lim_{n\to\infty} \left(\mathbf{W}^{\intercal}\right)^n \mathbf{s}(t_0) = c_1 \mathbf{e}_1, \tag{5.8}$$

i.e., the limit state, which is defined up to a constant anyway.

Analysing $\mathbf{e}_1$ allows us to isolate the effects of the flow in the time interval $[t_0,\, t_0 + \tau]$ and capture the trend of particle motion during that interval. The nodes in the transport network where the local value of the state $e_{i,1}$ is higher tend to attract tracers, even if the concentration given by $\mathbf{e}_1$ cannot be achieved, due to the time dependency of the weight matrix $\mathbf{W}(\tau)$. The analysis of the eigenvector $\mathbf{e}_1$ of networks $\mathbf{W}(\tau)$ as a function of time yields information about the presence or absence of specific levels in the channel that act as attractors for particles at different times τ.

The instantaneous flow field in which particles are released determines their initial velocity $\mathbf{v}(\mathbf{x}_0,0)$ and, thus, the initial evolution of their trajectories, at least for times shorter than the Lagrangian integral timescale. Since the initial velocity fields into which tracers are inserted are uncorrelated, also the resulting trajectories evolve differently in their initial phase, exhibiting a strong dependence on the initial velocity. Consequently, also the different realizations of the transport network $\mathbf{W}(\tau)$ are highly diverse, even at the same Reynolds number.

Figure 5.6(a) shows the eigenvector centrality $\mathbf{e}_1(\tau)$ of the nodes for four different realizations of the network at $\mathrm{Re}_\tau = 950$, as representative of the eigenvector centrality temporal behaviour: a clear peak, with a variable location depending on the realization, occurs at a time τ comparable with the integral timescale. A similar behaviour is found in all realizations. The attracting features of node with a high eigenvector centrality are therefore particularly relevant for times comparable with the Lagrangian velocity timescale, possibly because an attracting behaviour can arise after the correlation to the initial velocity field vanishes.

As time grows, the eigenvector centrality become more uniform across all nodes, as the effects of the inhomogeneities are smoothed out by the dispersion of tracers.

In the end, the eigenvector centrality becomes uniform across the channel height; indeed, the concentration of tracers becomes uniform in the wall-normal direction in the long run due to continuity and the well-mixed condition, and so does the limit state [182].

Figure 5.6(b) shows the spatial standard deviation of the eigenvector centrality, which was ensemble-averaged across realizations at the same Re_τ. In this way, we aim to represent its spatial structure concisely.

The high initial values are due to the presence of peaks, which then disappear as the non-uniform attraction of tracers vanes. Higher values of the standard deviation, as those found for the channel flow at $\mathrm{Re}_\tau = 180$, indicate a stronger imbalance the attracting strength of channel levels. In turn, this shows that at lower Reynolds number there are less attracting levels that attract more tracers, increasing the heterogeneity.

Additionally, we show in figure 5.6(c) the ensemble-averaged distance of the eigenvector centrality peak from the nearest wall of the channel, *i.e.* the spatial location of the highly attracting nodes. The eigenvector centrality peaks of different realizations at $\mathrm{Re}_\tau = 590$ and $\mathrm{Re}_\tau = 950$ do not have a preferential distribution over the interval $[0, \delta]$ (albeit slightly skewed towards the walls), thus their ensemble-averaged distance from the wall is approximately $\delta/2$; the same happens, after a short transient, at lower Reynolds number Re_τ. Instead, at $\mathrm{Re}_\tau = 180$, the average position of peaks is closer to the solid boundary. Thus, near wall levels of the channel act as sinks for tracers at $\mathrm{Re}_\tau = 180$, at least for some short time (the eigenvector centrality becomes almost uniformly distributed after $\tau \approx 2$). This is also the cause for the increased standard deviation found in figure 5.6(b).

5.3.4 Temporal properties of links

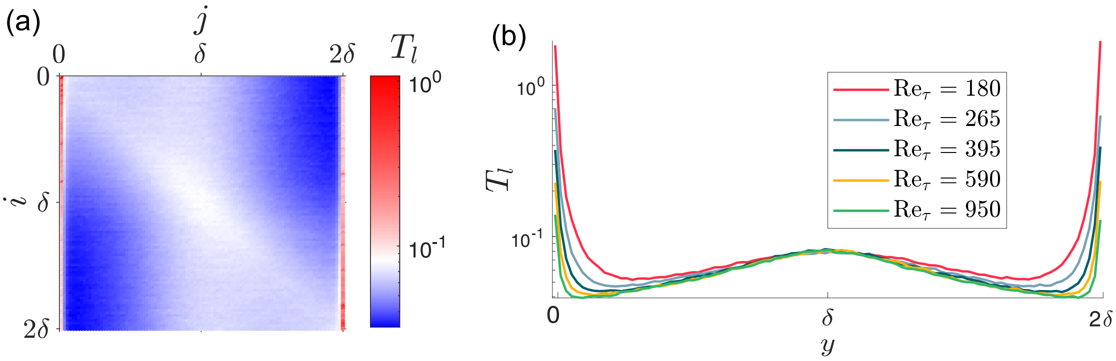

Figure 5.7: (a) Mean link duration for each pair of nodes (i, j), averaged over realizations at $\mathrm{Re}_\tau = 950$ (in the labels, the y coordinate of nodes is shown). (b) The same quantity shown in detail for links starting from the centreline level, averaged over realizations at all Reynolds numbers.

The peculiar effect of the walls on turbulent mixing is also evident from the analysis of the duration of links, *i.e.* the time that a particle moving from level i to level j of the channel (and thus activating a link $(i,\, j)$) spends in level j and maintains the link active. The temporal duration of links can be measured as the time a given link $(i,\, j)$ is continuously active in the evolving network $\mathbf{W}(\tau)$, not regarding changes of the value of its weight as long as it remains nonzero. In particular, we focus on the mean duration of links T_l, which we compute for each pair $(i,\, j)$ of nodes as the average temporal duration of the links connecting these two levels. T_l is shown in figure 5.7(a) for the channel flow at $\mathrm{Re}_\tau = 950$, where each entry $(i,\, j)$ of the plotted matrix displays the value of the mean duration of the corresponding link. The results were ensemble-averaged over realizations at $\mathrm{Re}_\tau = 950$.

It can be noticed that the mean duration of links depends more strongly on the spatial location of the ending node j than on that of the starting node. Indeed, links ending in the levels closest to the wall originate from particles with the largest permanence time in the same level (even an order of magnitude larger than in other regions of the channel). This behaviour is caused by particles becoming trapped in low-speed regions of the flow, which are more frequently located close to the walls (especially in the lowest level, of height equal to $2\delta/N_l$). Typical values of T_l in this region range from $T_l \approx 0.1$ at $\mathrm{Re}_\tau = 950$ up to $T_l \approx 1$ at $\mathrm{Re}_\tau = 180$.

The mean duration of links is also slightly larger than the minimum values of T_l for links ending near the centreline and for links originating between levels close in space; indeed, values of T_l larger than those obtained for other couples of connected levels are found near the diagonal of figure 5.7(a). As an example, links starting and ending near the center of the channel have a mean duration $T_l \approx 0.1$, independently of the Reynolds number. During this time a tracer moving with a velocity equal to that of the bulk flow moves a distance $\Delta x \approx 2.2\delta$ downstream at $\mathrm{Re}_\tau = 950$. The increased duration of links between nearby levels, which are the first to activate and are thus linked to the initial ballistic regime, highlights a dependence on both the ending and the starting level (although it is of lesser intensity than that on the ending level shown before). Indeed, since the link duration is increased if a tracer comes from a nearby level, indicating the possible presence of a memory effect.

Figure 5.7(b) shows the mean duration of links starting from the level located at the centreline $y = \delta$, with respect to the ending node j of the link, for all Reynolds numbers. The plots of figure 5.7(b) correspond to a single row of the matrix shown in figure 5.7(a). The duration T_l of links ending in levels near the center of the channel does not depend on Re_τ, indicating outer units scaling. Instead, the duration of links ending in the near-wall levels is higher for lower Reynolds number. Using wall-unit normalization, the link duration $T_l^+ = T_l u_\tau^2/\nu$ for the level nearest to the wall is nearly constant at the three higher Reynolds numbers, while it is almost three times larger at $\mathrm{Re}_\tau = 180$. Inner unit scaling in the near-wall region is present only at high enough Reynolds number.

5.3.5 Mean link length

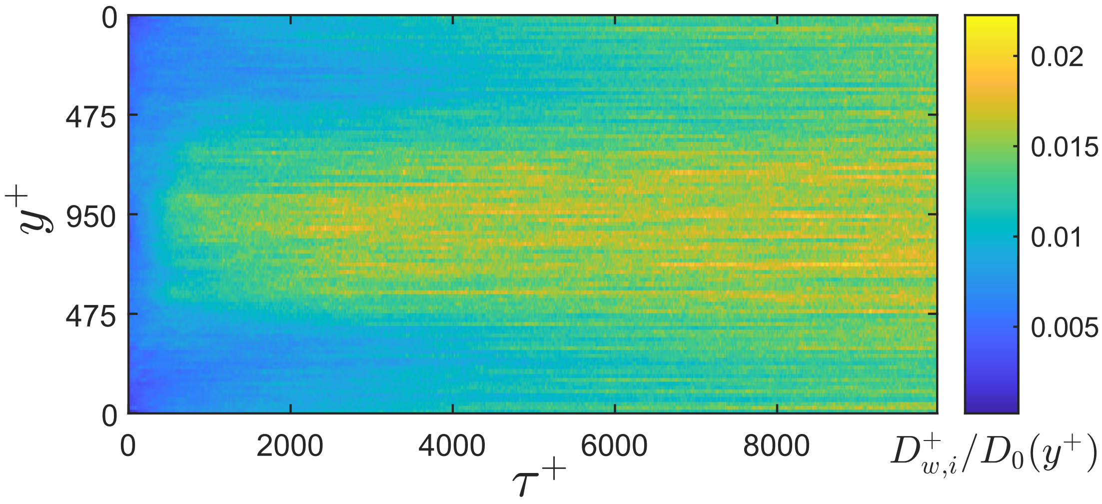

Figure 5.8: Weighted link length $D^O_{w,i}/D_0$, averaged for each node and corresponding to outgoing links.

Since the transport network is embedded in physical space, also the spatial position and relative Euclidean distances of nodes carry relevant information. In particular, the link connecting two nodes not only has a weight W_{ij}, but is also associated to a physical distance $l_{ij} = |i-j|2\delta/N_l$. The product between these two quantities $l_{ij}W_{ij}$ can be used to jointly represent the intensity and distance of a connection and highlight long distance connections that are generated by a significant number of tracers. To sum up weighted physical length information incident to a single node, we define the *mean weighted link length* D_w of the i-th node as

$$D^I_{w,i} = \frac{1}{k^I_i}\sum_{j\in\mathcal{V}} d_{ji}W_{ji}, \quad D^O_{w,i} = \frac{1}{k^O_i}\sum_{j\in\mathcal{V}} d_{ij}W_{ij}, \tag{5.9}$$

which is the average of all weighted link lengths incident to a node i, taken over ingoing and outgoing links separately.

We apply this measure to the transport network since we hypothesize that, while the majority of tracer exchanges happens locally, some infrequent events are present, in which a large number of particles moves between spatially distant levels. The use of $D^+_{w,i}$ is suitable to highlight this kind of extreme behaviour.

Figure 5.8 shows the outgoing and weighted link length $D^O_{w,i}$ of all the levels inside the channel from particle release to the start of the Taylor regime, computed for a single realization at $\mathrm{Re}_\tau = 950$. We did not perform ensemble averaging in this case since it would make impossible to detect extreme events. We normalized the value of the link length of each level with a factor D_0 dependent on the y^+ value of that level and equal to

$$D_0(y^+) = \frac{1}{2\delta}\int_0^{2\delta} |s - y^+| \mathrm{d}s = \delta - y^+ + \frac{(y^+)^2}{2\delta}. \tag{5.10}$$

By doing so we divide the value of $D^O_{w,i}$ by the average physical distance between the i-th level and the rest of the channel; by doing so, we can account for the fact that near-wall levels have higher $D^O_{w,i}$ due to their position (since they are able to form longer distance links). Figure 5.8(a) shows that $D^O_{w,i}/D_0$ rises faster in the core region and exhibits a distinction between the near-wall and the external region. The central region is found to be more active in the mixing process, similarly to what was found using the degree centrality, with the added finding that longer distance links are also formed there.

As time grows, it can be noted that some nodes have a larger $D^O_{w,i}/D_0$ than their closest neighbours and that this behaviour is quite persistent in time. This determines the presence of streaks in figure 5.8(a), especially for large times, whose duration is of the order of unity in outer units ($1000\nu/u_\tau^2$ at $\mathrm{Re}_\tau = 950$). Trapped tracers that contribute to the formation of long duration links are therefore also highlighted by the mean link length.

5.3.6 Communities

The degree centrality and the weighted link length hint at the presence of separate regions inside the channel, with different mixing properties. We exploit the capabilities of complex networks to partition the turbulent channel into regions which exchange a reduced number of tracers between themselves. To do so, we use the algorithm introduced by Girvan and Newman [74], which was described in chapter 4.

This algorithm, applied to networks built at different times τ for a single batch of particles at $\mathrm{Re}_\tau = 950$, identifies two long lasting communities located near each of the channel walls; also, some smaller communities are found at the centreline, which rapidly break up and disappear. Figure 5.9(a) shows the modularity of the network at different delays, decomposed into the contribution given by the two partitions located attached to the solid boundary and all the other communities. Recalling that the modularity can be thought of as the sum of the individual contributions of single community, we note that in the case of the transport network the largest contributions comes from the two near wall communities until $\tau^+ \approx 4000$ (around $\tau = 4$ in outer units). After this time these partitions dissolve and no modular structure can be identified any more, which is when also the degree becomes more homogeneous across the channel height as the transient phase of mixing ends and Taylor's regime begins.

The spatial organization of the communities during different phases is shown in figure 5.9(b). The central communities are small and possibly related to the local,

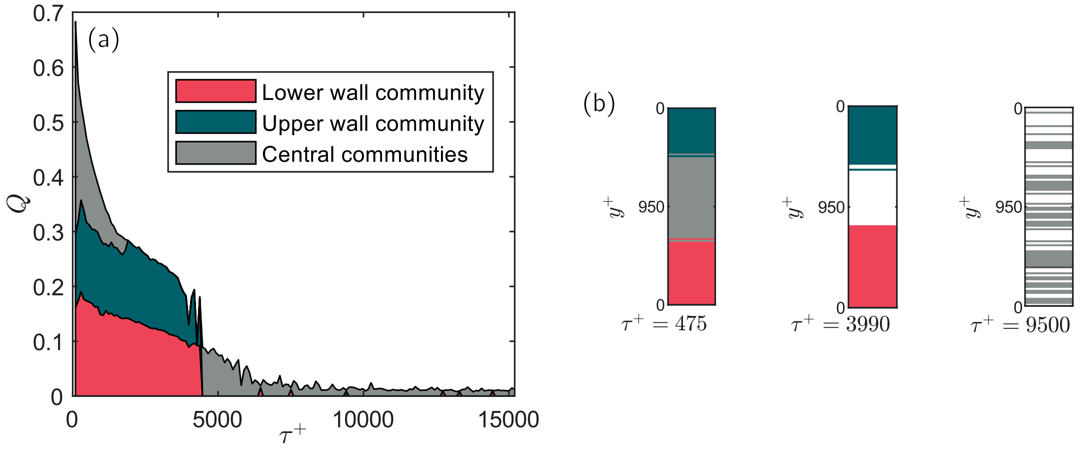

Figure 5.9: (a) Modularity of the network is shown at different delays τ and decomposed into the contributions given by the near-wall (top and bottom) and all the central communities together; (b) Community organization for three different times is shown: for very short times, two near-wall regions are present, while in the channel core there is a large number of small communities, which we all indistinctly show in gray; for intermediate times, only the near-wall communities remain (the center region presents no community structure and is shown in white); in the end, all communities dissolve and no modular structure can be identified (only small communities are present, shown in gray; still, their contribution to the modularity is negligible).

small-scale features of turbulent motion near the centreline. Instead, the top and bottom communities are coherent in time and space and indicate the presence of two secluded regions, that is regions at y coordinates lower than about $\delta/2$, which exchange a reduced number of particles with the central region of the channel. The communities located in the core region are small (we show all of them indistinctly in grey in figure 5.9(b)) and quickly dissolve.

We also aim to provide a brief characterization of the structure of communities in the network through the spectral properties of the Laplacian matrix, as was defined in chapter 4. This is an alternative approach to network partitioning, which has been employed in geophysical problems. By doing this, we provide a comparison with the modularity approach in the specific case of channel flow particle dispersion. Since the flow network is weighted other than directed, the definition of the Laplacian matrix will be extended [202]. First, the directed incidence matrix $\mathbf{B} \in \mathbb{R}^{N\times K}$ is defined as

$$B_{ij} = \begin{cases} 1 \text{ if } v_i \text{ is the starting vertex of } l_j \\ -1 \text{ if } v_i \text{ is the ending vertex of } l_j \\ 0 \text{ otherwise} \end{cases} \tag{5.11}$$

Subsequently, a diagonal weight matrix $\mathbf{W}^d \in \mathbb{R}^{K\times K}$ is introduced, defined as

$$W^d_{ii} = W(l_i) \tag{5.12}$$

where $W(\cdot)$ is the weight of the i-th and the edges l_i are ordered in the same way as the directed incidence matrix $\mathbf{B}$. The weighted Laplacian is then defined as

$$\mathbf{\Lambda}^w = \mathbf{B}\mathbf{W}^d\mathbf{B}^\intercal \tag{5.13}$$

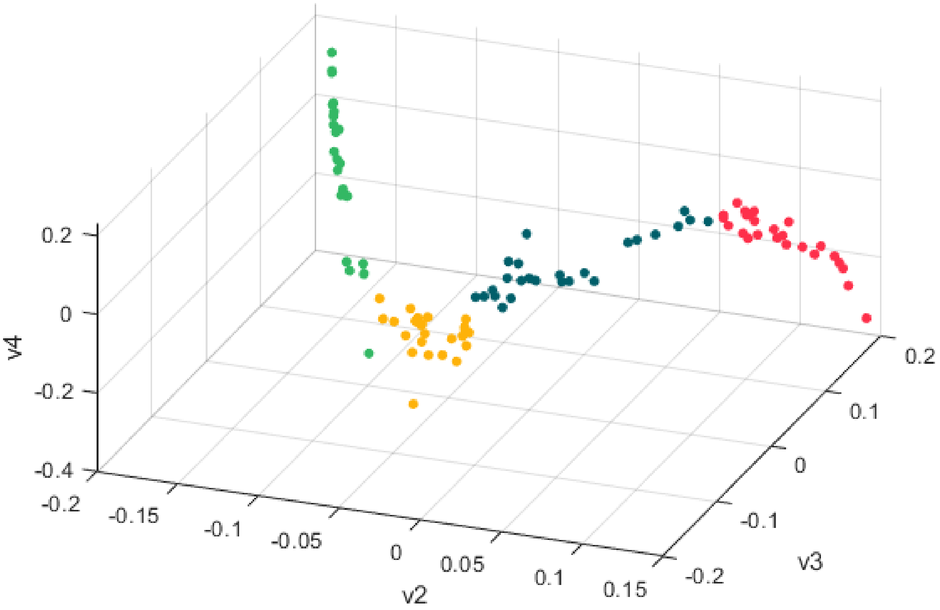

Figure 5.10: Eigenvector plot, non cumulative flow network at $\tau^+ = 712$. The colouring identifies the origin zones; red: $0 < y < \delta/2$, blue: $\delta/2 < y < \delta$, yellow: $\delta < y < 3\delta/2$, green: $3\delta/2 < y < 2\delta$

Figure 5.10 shows the distribution of the components of the first three non trivial eigenvectors of $\mathbf{\Lambda}^w$, whose mutual position in euclidean space is a proxy for their community organization. Some grouping takes place, especially between the levels of the upper wall region (green dots). The eigenvector entries corresponding to levels close in space appear grouped together in eigenvector space. We note that the number of eigenvectors showing nontrivial information is rather small and that grouping levels based on their distance in eigenvector space is more difficult due to the need of defining a grouping strategy. Accordingly, the approach based on modularity optimization appears more robust, as it is able to clearly identify separate communities without having to resort to grouping the eigenvector components.

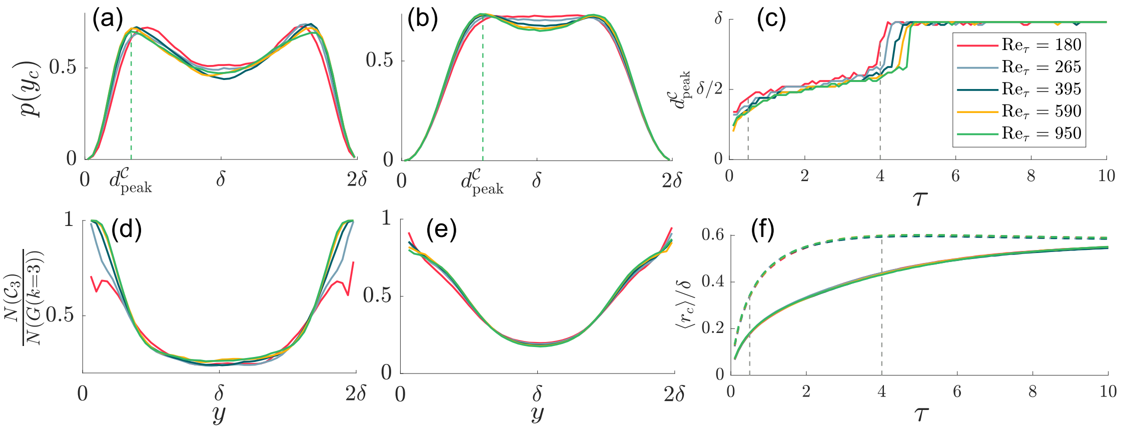

Figure 5.11: (a)-(b) Concentration of cycles' centroids in the transport networks $\mathbf{W}(\tau = 0.5)$ and $\mathbf{W}(\tau = 4)$, ensemble averaged at five different Reynolds numbers. (c) Distance of the peaks of the concentration of cycles from the wall, as a function of time. (d)-e) Prevalence of cycles in the same networks as the previous panels, computed as the ratio between the number of cycles and the number of all subgraphs with three nodes. (f) Mean radius of cycles (solid lines) and of subgraphs that are not cycles (dashed lines), as a function of time; the vertical lines show the two time instants of figures 5.11(a) and (b).

5.3.7 Cycles

The dispersion of tracers is also influenced by the organized motions present in wall-bounded flows at a large range of scales, which are present at all Reynolds numbers. The flow structures associated with the near-wall cycle determine the presence of intense wall-normal motions that eject low speed fluid (and the tracer particles contained therein) into the outer flow and the *vice versa* [194].

The motion of tracers, which sample the underlying velocity field, is reflected into the network properties. The spreading of particle clouds influences the scale of the flow structures with which they interact.

Small subsets of tracers that are close in space may become entrained in coherent structures, and in turn inherit their common and recognizable features. This translates, in the spatially coarse perspective employed in this work, into recognizable patterns of fluid exchange between levels of the channel. Tracers trapped in a wall-normal cyclic motion will move between a subset of the levels of the channel in a loop, at least for the time in which the underlying flow structure remains coherent.

As an example, a looping pattern involving three nodes i, j and k inside the transport network (formally, a cyclic subgraph of $\mathbf{W}(\tau)$), is generated when some tracers released from level i reach level j at time τ, while at the same time tracers leaving j and k reach levels k and i, respectively. In the transport network framework, the analysis of cyclic subgraphs has been used to uncover periodic trajectories in steady or periodic flows and cyclic motions in unsteady flows [170]. We extend this kind of pattern analysis to search for motifs, that is statistically significant patterns of node interconnection, which were introduced in chapter 4.

We identified motifs using a depth-first search at different values of Re_τ and for all realizations of the network. In particular, we searched the network for cyclic subgraphs with three nodes, *i.e.* a subset of three nodes of the network that are connected in a directed loop.

To determine whether the cyclic subgraphs found with the aforementioned procedure are indeed motifs, *i.e.* they contribute significantly to the behaviour of the network, we analysed their statistical relevance using as a null model a random network. Since standard random graph models do not apply to the transport network we randomly generated a network in which nodes have the same number of connections of the nodes of the real transport network $\mathbf{W}(\tau)$. Afterwards, we computed cycles of three nodes in this random network, using the same depth-first search algorithm.

We found that in the real transport network cycles occur more frequently and are also distributed differently across the height of the channel. Specifically, cycles in the random network are more frequent near the center of the channel than near the walls, while this is not the case for the real network.

Figures 5.11(a) and 5.11(b) show the spatial distribution of the centroids of cyclic subgraphs in $\mathbf{W}(\tau = 0.5)$ and $\mathbf{W}(\tau = 4)$, respectively. Ensemble averaging between realizations at the same Re_τ was performed. We computed the centroid coordinate y_c by averaging the spatial coordinates y_i of the three network levels involved in each cyclic subgraphs. The concentration of cycles has a peak near $y = \delta/2$ and decreases to zero close to the wall, because of the finite size of cycles. With increasing time, the peaks of the distribution move towards $y = \delta$, eventually joining abruptly in the middle of the channel at about $\tau = 4$. The shift of the peak location in time occurs almost independently of the Reynolds number, although at $\mathrm{Re}_\tau = 180$ and 265 peaks are somewhat closer to the center of the channel and they join in the center slightly earlier. The distance of the peaks from the wall d^c_{peak} as a function of time τ is shown in figure 5.11(c). Shortly after release, cyclic interconnection patterns between nodes are more likely to be found near the wall, where the local vortical motions are more likely to impress swirling patterns on the collective motion of tracers.

Because of the way the transport network is built, one needs only temporally sparse position data of particles to explore the existence and effects of swirling motions of tracers, thus easing the computational requirements and the need for additional data (*i.e.* particle velocities and accelerations or vorticity fields).

Figures 5.11(d) and 5.11(e) show the ratio between the number of cyclic subgraphs and the number of all subgraphs with three nodes, across the height of the channel and at the same times τ as used for figures 5.11(a) and 5.11(b). Close to the walls, cyclic subgraphs form the largest contribution to three-node patterns, while their relative concentration diminishes away from the walls. Thus, cyclic motions of particles are dominant near the walls of the channel. This happens at all Reynolds numbers, even though at the lowest one ($\mathrm{Re}_\tau = 180$) the prevalence of cycles is not as high as in the other cases.

In figure 5.11(f) we show the mean radius of cycles r_c, computed as the average distance between each node involved in the cycle and its centroid $r_c = \frac{1}{3}\sum_{i=1}^{3}|y_i - y_c|$. The mean radius of cycles (solid lines) grows more slowly than the mean radius of subgraphs with three nodes that are not cycles (dashed lines). This happens independently of the Reynolds number, even at the lower Reynolds numbers. The slower growth of the size of cycles implies that the diffusion of clouds of particles entrained in cyclic motions is impeded, since their size in average grows more slowly than that of clouds of tracers that do not take part in cyclic motions. While the effectiveness of single cycles in retaining tracers is unchanged across different Reynolds numbers, the stronger prevalence of cycles at the higher Reynolds numbers indicates a stronger inhibition of dispersion caused by vortical flow structures.

5.3.8 Sensitivity of the network to resolution

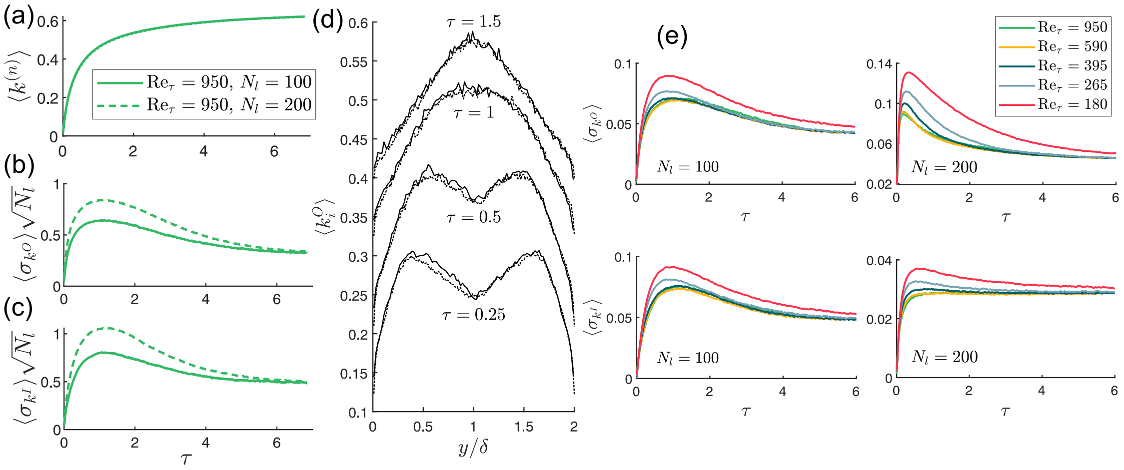

Figure 5.12: (a) Mean degree at $\mathrm{Re}_\tau = 950$, simulations with $N_l = 100$, $N_p = 10\,000$ and $N_l = 200$, $N_p = 40\,000$. (b) outgoing and (c) ingoing degree standard deviation, normalized by $\sqrt{1/N_l}$, same flow cases as in (a). (d) ensemble averaged outgoing degree versus the y coordinate and at different times (solid lines: $\mathrm{Re}_\tau = 950$, $N_l = 100$, $N_p = 10\,000$; dashed lines: $\mathrm{Re}_\tau = 950$, $N_l = 200$, $N_p = 40\,000$). (e) outgoing and ingoing degree standard deviation (top and bottom panels, respectively); left panels show all Reynolds numbers with $N_l = 100$ and $N_p = 10\,000$, while right panels show all Reynolds numbers with $N_l = 200$ and $N_p = 10\,000$.

Finally, in order to characterize the influence of the wall-normal partitioning of the channel on the results, the sensitivity of the network representation of dispersion with respect to the number of network levels N_l is analysed. By doing so, we explore the influence of the spatial scale used to build the network (recall that fluid features smaller than the level size are not explicitly accounted for in the network representation). To investigate the effects of the number of levels, and thus the spatial size of the discretisation employed to build the network, we released another set of $N_b = 60$ batches of particles in the channel flow at $\mathrm{Re}_\tau = 950$. Differently from the simulations employed before, we used a release grid composed of $N_l = 200$ levels, each one with 200 particles, for a total of $N_p = 40\,000$ particles. Keeping the ratio N_p/N_l^2 unitary allows us to have the same asymptotic value of the mean degree normalized by N_l, *i.e.* $1 - 1/\mathrm{e}$, found for the $N_l = 100$ case. This property was derived from the assumption that for long times τ network weights are Poisson distributed. Accordingly, the degree is binomially distributed with a success (link existence) probability of $1 - 1/\mathrm{e}$ and a number of trials equal to N_l. The mean degree $\langle k^{(n)} \rangle$ is shown in figure 5.12(a); the two cases with different N_l exhibit perfect collapse (note that in each case the degree is normalized with the number of levels N_l, which is also the number of nodes).

Figures 5.12(b) and 5.12(c) show the values of $\langle \sigma_k \rangle$ normalized by $\sqrt{1/N_l}$. Indeed, the asymptotic value of the degree, which is binomially distributed, has a standard deviation proportional to $\sqrt{N_l}$; since we normalize the degree by N_l, similarly we divide the degree standard deviations by $\sqrt{1/N_l}$. Figures 5.12(b)-(c) show that, before the asymptote, the ingoing and outgoing degree in the case with $N_l = 200$ are more heterogeneous, resulting in larger values of the standard deviations. The increased heterogeneity of the degree is a result of the inclusion of finer scales of motion in the network dynamics. Still, the main features are retained, such as the presence and time of a peak and the imbalance between ingoing and outgoing degree. Furthermore, the spatial structure of the degree is left mostly unchanged, as can be seen in figure 5.12(d), where the ensemble averaged outgoing degree $\langle k_i^O \rangle$ is plotted against the channel y coordinate for several times. Differently from figure 5.5(a), the mean degree $\langle k^{(n)} \rangle$ was not subtracted to enhance readability.

To further explore the relationship between the discretization and the Reynolds number scaling, we reused the particle trajectory data used before, comprising of several batches of $N_p = 10000$. We defined a larger ($N_l = 200$ and above) number of levels. We used as initial time for the simulation a time after the actual release of particles. Indeed, at $t = 0$ particles are orderly distributed and would not fill all $N_l > 100$ levels. Instead, in this way, all levels are filled (although by a non constant number of tracers). Since in this case $N_p/N_l^2 \neq 1$, the asymptotic values of the degree statistics are not conserved. Furthermore, the degree (especially the outgoing one) appears to be more inhomogeneous due to the uneven initial distribution of particles.

However, since in any case the degree of each node is normalized with its maximum attainable value, it is possible to compare the evolution of the degree standard deviation at different Reynolds numbers in the cases with increased N_l. Figure 5.12(e) shows the ensemble-averaged standard deviations of the outgoing (top panels) and ingoing (bottom panels) degree centralities. In the left panels, the original configuration with $N_l = 100$ computed with the aforementioned procedure is shown. These left panels demonstrate that, similarly to the network generated from the regular grid of particles, curves at Re_τ greater than 395 collapse exhibiting Reynolds number independence when scaled with outer units. Increasing the number of levels to $N_l = 200$ (right panels) leads to the appearance of a slight separation between the degree standard deviation at $\mathrm{Re}_\tau = 395$ and those at higher Reynolds numbers, which in turn remain collapsed. We found that increasing the number of levels even further (up to $N_l = 500$, not shown here) a similar structure is retained, with the standard deviations at $\mathrm{Re}_\tau = 590$ and 950 collapsed and that at $\mathrm{Re}_\tau = 395$ slightly separated.

The spatial resolution increase of the network introduces the effects of smaller scales of motion, which are particularly important in the near wall region and contribute to the differentiation of the network evolution at lower Reynolds numbers. Still, we found that the scaling at the two higher Reynolds numbers employed in this work is rather insensitive to the increase of the number of spatial levels. Only the point at which the Reynolds independent behaviour starts is slightly modified by the increase of resolution. The sensitivity analysis shows that, even increasing the spatial resolution of the discretisation, the main features of dispersion are unchanged. The increase of resolution allows the network representation to account for smaller scales of fluid motion. While this effect is somewhat important at the lower Reynolds numbers, it is negligible at the higher Re_τ employed here, indicating that outer flow structures are most important in determining the evolution of dispersion.

5.4 Discussion

Using the different network features analysed in the previous sections, we are able to provide a multifaceted perspective on the dispersion process. While some features of dispersion appear in the network at all Reynolds numbers, we found that some properties are exclusive to higher or lower Reynolds number flows. Most notably, while dispersion of tracers near the walls is reduced in any case, different mechanisms come into play depending on the Reynolds number. Moreover, through the network we found that above $\mathrm{Re}_\tau = 395$ many network properties exhibit Reynolds number independence if scaled with outer units (with the spatial resolution $N_l = 100$).

The number of connections established by a node via particle motion, *i.e.* its degree centrality, is a concise measure of the local dispersion of particles in that node.

Owing to the non-homogeneous nature of channel flow, we found the growth of the degree to be highly dependent on both the spatial location of nodes and the time τ from the release of particles. At very short times $\tau \ll T_L$, the degree centrality of each node grows proportionally to the wall-normal velocity variance in that node. Indeed, when groups of particles are still confined to a small spatial region, their dispersion is solely dominated by the local velocity fluctuations. As such, the initial evolution of the degree (figure 5.5(a)) shows how initially dispersion grows faster in the near-wall region, coherently with the y location of the wall-normal velocity fluctuations peak. Differently, for times comparable or longer than the Lagrangian integral timescales of the flow, the wall-normal velocity variance cannot alone explain the observed dispersion of particles. We observe that the dispersion becomes stronger near the centreline of the channel and weaker near the walls; therefore it appears that phenomena other than the wall-normal velocity fluctuations come into play, resulting in an inhibition of near-wall dispersion. Moreover, at short (but comparable with T_L) times, the high values of the eigenvector centrality in a few close nodes of the network shows the presence of a localized attractor, *i.e.* a zone in the channel that transiently attracts tracers. This attractor influences the dynamics of the entire set of particles, even those that are distant from the high eigenvector centrality nodes. Therefore, the attractor characterizes the shift from a regime in which only local velocity fluctuations determine the evolution of dispersion to a stage when the entire range of scales of motion in the channel flow affects the dispersion of groups of particles.

The shift of peak dispersion from the near-wall region of the channel to the centreline is also associated with the time at which the spatial non-homogeneity of dispersion is the highest, as is shown by the peak at $\tau \approx 1.5$ of the degree standard deviation σ_k. Only after a rather long (compared to the integral timescale) transient, the inhomogeneities of the degree are smoothed out, as wall-normal mixing is complete and dispersion has entered an asymptotic phase similar to Taylor's regime in homogeneous flows.

The network analysis enables us to pinpoint the causes for the inhibition of near-wall dispersion: the very low intensity of near wall velocity fluctuations and the presence of cyclic motions of particles, each one with its varying relative importance at different Reynolds numbers. First, wall-normal velocity fluctuations near the wall have a reduced intensity with respect to the rest of the channel, so that particles that move towards the wall are less prone to being vertically displaced by turbulent velocity fluctuations. This is also evident, in the network perspective, from the increased duration of links ending near the wall, which is linked to the residence time of particles in those levels. The second mechanism, highlighted by the analysis of motifs, is linked to the presence of cyclic patterns of motion of particles between channel levels. We have shown with the analysis of communities present in the network, that there is a clear partitioning of tracer motion, which confines (at least for short and intermediate times) near-wall located particles to the immediate whereabouts of their release position.

Tracers that move persistently in cyclic paths are effectively prevented from reaching other levels since, even if there is an exchange of tracers as in the other regions of the channel, this happens between nodes interconnected in loop-like paths that do not promote the diffusion of tracers towards other nodes. Thus, the significant increase in the concentration of cycles found towards the wall is an obstacle to particle dispersion. Cyclic motion, which results from the action of vortical flow structures hosted in the near wall region, is highly important near the walls; additionally, the slower growth of the radius r_c of cyclic motifs than other non-cyclic structures indicates that the embedding of particles in such motion patterns contributes to the inhibition of their dispersion for an extended period of time.

While at the higher Reynolds numbers analysed in this work ($\mathrm{Re}_\tau = 395$, 590, and 950) cyclic motifs are highly prevalent near the walls and constitute nearly the entirety of the network structure, we found the cycles at lower Reynolds numbers to be less frequent, both absolutely and with respect to the totality of link patterns. Even if cycles have a role in slowing down dispersion, the reduction of the prevalence of cycles is not associated to an increase of dispersion at the lower Reynolds numbers, where instead dispersion is even more inhibited. The slower near-wall dispersion results in an increased heterogeneity of the degree at $\mathrm{Re}_\tau = 180$ and 265 and greatly increases the temporal duration of links ending in the near-wall region, indicating prolonged residence of tracers in those regions. Also, attractors in the channel at lower Reynolds numbers are predominantly located near the walls (see figure 5.6), indicating that the near wall levels greatly influence the overall dynamics inside the channel and that particles entering these levels tend to remain there for prolonged times.

At lower Re_τ the main cause for the inhibited dispersion seems to be the reduced wall-normal velocity fluctuations near the walls, which result in longer link durations and increased presence of attractors in that region. Cyclic paths, instead, are less prevalent and their peak concentration is located farther from the wall. As the Reynolds number grows larger, the near-wall effects become confined to a smaller portion of the channel and cyclic structures acquire a dominant role in slowing down dispersion of tracers. It is also possible that a larger prevalence of near-wall vortices such as that found at higher Reynolds numbers, while being detrimental to dispersion across long timescales, is beneficial in lifting particles away from the near wall region.

At the higher Reynolds numbers ($\mathrm{Re}_\tau = 395$, 590, and 950) we found that many network properties are independent of the Reynolds number, if outer flow variables are used to normalize the time τ. The reason is that the mixing process involves ever growing scales of motion inside the flow, as the clouds of tracers released inside each level grow larger. Additionally, the discretisation employed to create the network divides the channel into levels whose height is independent of Re_τ when scaled in outer units (since it is always equal to $2\delta/N_l$). The discretisation effectively filters out from the network representation scales smaller than $2\delta/N_l$. The importance of the filtered scales was analysed section 5.3.8. Accordingly, the network evolves independently of the Reynolds number as outer flow scales are dominant in the overall mixing process and in its network representation.

The outer-scale collapse happens to both global properties of the network, such as the degree y-average and standard deviation, and to local properties like the spatial concentration of cyclic motifs, with the notable exception of the temporal duration of links which scales with inner variables in the near-wall region. Indeed, local properties of network nodes, even those located inside the near wall region, are influenced by the links entertained by these nodes. For short times these links only connect nodes which are very close in space, and thus node properties reflect the local flow features (*i.e.* the velocity fluctuations as shown in figure 5.4). For longer times instead links connect more distant nodes, so that no network property is truly local. On the contrary, as was shown in figure 5.7(a), the temporal duration of links depends almost exclusively on the end level, so that near the wall the inner scaling appears.

Instead, at lower Reynolds numbers ($\mathrm{Re}_\tau = 180$, 265 and, to a lesser extent, 395) the scaling by outer variables observed at higher Reynolds numbers does not hold. While the asymptotic phase of dispersion (approximately $\tau > 6$) is the same at all Reynolds numbers (since asymptotic network properties reflect a fully random state), during the transient stage dispersion at low Reynolds numbers appears to be more spatially inhomogeneous and linked to a different underlying mechanism than those bound to the action of outer scales at higher Re_τ. While wall-normal velocity fluctuations continue to grow in the Reynolds number interval considered in this work, transport network features, and thus global dispersion properties, achieve Reynolds independence above a certain threshold, which is approximately between $\mathrm{Re}_\tau = 395$ and 590. We hypothesize that above this threshold the effects induced by the wall, especially the presence of a region with very low wall-normal velocity variance that traps particles and hence inhibits dispersion, become confined to a portion of the channel half-height δ that is negligible. Therefore, the contribution of the outer flow in determining the evolution of dispersion becomes dominant, the interaction between cyclic structures and local velocity fluctuations becomes Reynolds-independent, and outer flow scaling is achieved.

Chapter 6

Inertial particle mixing in turbulent channel flow

Some of the contents presented in this Chapter have been previously published. Below are provided the references:

D. Perrone, J.G.M Kuerten, L. Ridolfi, S. Scarsoglio, "Investigating the magnitude and temporal localization of inertial particle mixing in turbulent channel flows", in *Int. J. Multiph. Flow.* **165**, 104489 (2023)

6.1 Rationale

In this chapter, the mixing of inertial particles coming from pair of sources in a turbulent channel flow is analysed by means of particle tracking numerical simulations. The interactions between particles released from distinct sources depends, first and foremost, on the position of the sources, both with respect to the channel and to each other. Indeed, while in homogeneous and isotropic turbulence only the mutual distance may be of relevance, in a channel flow the properties of turbulence vary strongly depending on the distance from the wall. Also, as there is a mean shear, the alignment of sources makes so that some source pairs may experience greatly varied mixing properties.

Other than source position, the other relevant factor is the inertia of particles. Indeed, as non-tracer particles experience inertial clustering, their mixing is expected to be influenced by their organization into an intermittent spatial distribution, which may in some cases hinder and in some cases enhance mixing.

To quantify mixing of inertial particles, we perform a direct numerical simulation of channel flow at $\mathrm{Re}_\tau = 950$. We release inertial particles with different diameters, resulting in four distinct Stokes numbers $\mathrm{St}^+ = \tau_p^+ = \mathrm{St}_K \tau_\eta^+ = 0.2, 1, 5, 25$. We note how the Stokes number based on the Kolmogorov units is not constant across the channel height as τ_p depends on wall distance. By varying the position of the two sources, we provide a description of the effect of the position with respect to the channel walls and of the influence of mutual distance and alignment.

In the following, section 6.2 contains an overview of the methods employed, section 6.3 shows the results obtained and section 6.5 provides a discussion and an interpretation of the results.

6.2 Methods

Similarly as in the previous chapter, the Lagrangian data were obtained through the numerical integration of trajectories of tracer particles. The same pseudospectral method was employed, performing a simulation at $\mathrm{Re}_\tau = 950$. To provide additional results regarding Reynolds number scaling, also simulations at $\mathrm{Re}_\tau = 590$ were performed. The parameters used for the two simulations, that is, the box size $L_x \times L_y \times L_z$, the number of polynomials employed in the discretization $N_x \times N_y \times N_z$ and the time-step in outer units Δt are given in table 6.1.

Table 6.1: Main parameters for the direct numerical simulations at $\mathrm{Re}_\tau = 950$: domain size $L_x \times L_y \times L_z$, number of polynomials used for the simulation $N_x \times N_y \times N_z$ and time step of the trajectories Δt^+

Re_τ	$L_x \times L_y \times L_z$	$N_x \times N_y \times N_z$	Δt^+
950	$2\pi\delta \times 2\delta \times \pi\delta$	$768 \times 385 \times 768$	0.095
590	$2\pi\delta \times 2\delta \times \pi\delta$	$768 \times 385 \times 768$	0.07375

We integrated the trajectories using the finite-Reynolds correction introduced in chapter 3. The density ratio ρ_p/ρ between the particles and the carrier fluid is 769.23; the Stokes number is varied by changing the diameter of particles, thus resulting in diameters ranging from $d_p^+ = 0.068$ at $St^+ = 0.2$ to $d_p^+ = 0.764$ at $St^+ = 25$. Collisions with the wall are treated elastically. Gravity effects were not included in order to focus only on turbulence-induced features of particles dynamics, which are easily overwhelmed by settling effects if gravity is included. Particles are released in a puff at once only to accelerate the computation of statistics, as we are not interested in the proximity of particles coming from the same release location. We do not consider the mutual interaction between particles nor their back-reaction on the carrier flow, as we aim to consider dilute flows.

The main goal of this work is to quantify the mixing of clouds of tracers released from different sources and the rate at which they encounter. To do so, we introduce inertial particles from spherical sources whose size is finite and of the order of the smallest flow features. The radius of spherical sources is equal to unity in wall units, which is of the same of order of magnitude of the Kolmogorov length scale (which, instead, is not constant and depends on y). Each source releases $N_p = 256$

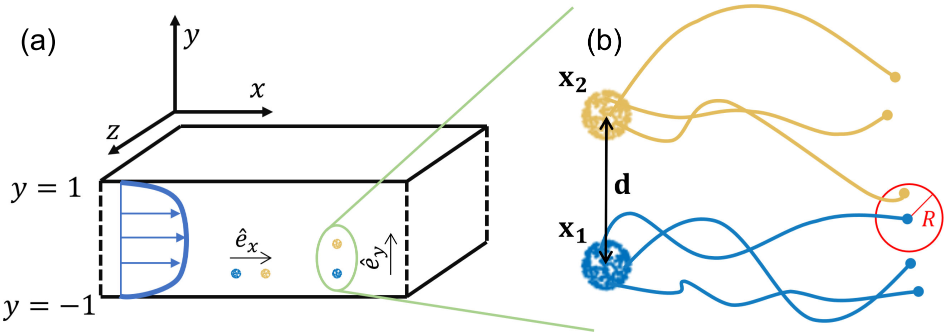

Figure 6.1: a) Channel geometry and coordinate system; two pairs of sources are represented, one aligned along the streamwise direction, the other along the wall-normal one. b) Schematic depiction of how encounters are determined starting from particle trajectories.

particles at once. In this way, the evolution of trajectories reflects the properties of a local region while avoiding that particle velocities remain correlated for very long times, as would instead happen if all particles were released in the same point.

We introduce an *ad-hoc* quantity, the encounter probability E, to measure mixing between two distinct sources. In particular, we compute the number of particle pairs coming from the two plumes that are closer than a threshold distance R, as shown in figure 6.1(b). This value, normalized by its largest possible value N_p^2, is the encounter probability. As an example, $E = 1$ would be obtained only after perfect mixing of particles coming from two sources, that is, if all particles released from both sources become located in a small (of the order of the threshold R) region of space.

For two plumes released from two distinct locations $\mathbf{x}_1$ and $\mathbf{x}_2$, the encounter probability, which is a function of time, can be computed as

$$E_{\mathbf{x}_1,\mathbf{x}_2}(t) = \frac{|\{\|\mathbf{x}_i(t) - \mathbf{x}_j(t)\| \leqslant R : \mathbf{x}_i(0) = \mathbf{x}_1 \wedge \mathbf{x}_j(0) = \mathbf{x}_2\}|}{N_p^2}. \tag{6.1}$$

$\mathbf{x}_{i/j}(t)$ is the trajectory of the i/j-th particle of the plume starting from $\mathbf{x}_{1/2}$ and $\|\cdot\|$ is the Euclidean norm. From the definition it follows that $E_{\mathbf{x}_1,\mathbf{x}_2}(t) = E_{\mathbf{x}_2,\mathbf{x}_1}(t)$.

The choice of the threshold distance R is non-trivial. Large values would lead to inaccuracy in the description of clusters, as grouping of particles that are not relevant to the flow physics would be captured. Instead, if the effects of turbulence and particle inertia are to be accounted for, the threshold distance R should be shorter than the typical scales at which this phenomena take place. Since inertial clustering takes place on typical length scales of the order of tens of wall units (as it is in turn a result of the action of small-scale flow features), we chose a threshold size $R^+ = 2$. An analysis of the sensitivity of our results with respect to the value of R is reported in the following.

As the position of the two sources has the greatest influence on the evolution of the encounter probability, we thoroughly vary $\mathbf{x}_1$ and $\mathbf{x}_2$ across the channel. We report the absolute position of one of the two sources, *e.g.* $\mathbf{x}_1$, and the mutual distance between the two sources $\mathbf{d} = \mathbf{x}_2 - \mathbf{x}_1$. As channel properties are statistically homogeneous along the x and z directions, only the wall-normal component of the position $y_1 = \mathbf{x}_1 \cdot \hat{\mathbf{e}}_y$ is relevant and will be considered hereafter. Instead, considering all three components of $\mathbf{d}$ is necessary, since channel flow is anisotropic and mixing properties depend on the relative orientation of the two sources. Meaningful values of the distance modulus $d = ||\mathbf{d}||$ are bounded by the constraint that at least some particles interact and contribute to the encounter rate. Accordingly, the admissible values of d are bound to that of R, since if $d \gg R$ the encounter probability becomes negligible. In the following, we analyse mixing with a distance between sources comprised between $d^+ = 4$ and $d^+ = 32$ (at which the encounter probability is already vanishing independently of time).

Finally, as particles are released into fully developed turbulent flow, their initial velocities have different properties depending on the local instantaneous flow field, and accordingly also encounter properties show the same dependence. In order to achieve statistical significance, for each set of parameters (y_1, $\mathbf{d}$, St) we analyse multiple pairs of sources, positioned at different x and z coordinates and at different times, choosing appropriate spatial and temporal spacing so that their evolution is uncorrelated. Subsequently, we average the results to obtain a final value of the encounter properties, since channel properties are statistically homogeneous along the streamwise and spanwise directions and are statistically steady through time. For each set of parameters we analyse $N_r = 384$ independent pair of sources.

6.3 Results

6.3.1 Evolution of the encounter rate

After release, a transient growth of the encounter probability is observed due to turbulent diffusion and, for y-aligned pairs, the action of local shear. Both these phenomena have the effect of increasing (on average), the size of puffs over time. The encounter probability rises because large puffs coming from distinct sources eventually collide with each other and because, locally and on short timescales, distant groups of particles are brought together by the local action of turbulence. After E reaches a peak, turbulent diffusion takes over and particles do not come any more in close proximity to each other, resulting in a vanishing encounter probability at long times.

Figure 6.2 shows the typical evolution of the encounter probability for some pairs of sources, that are releasing particles whose Stokes number is 0.2 (panels (a) and (b)) and at varying Stokes number (panel (c)). In particular, we chose source pairs at two different wall-normal coordinates $y_1^+ = 20$ and $y_1^+ = 950$ in

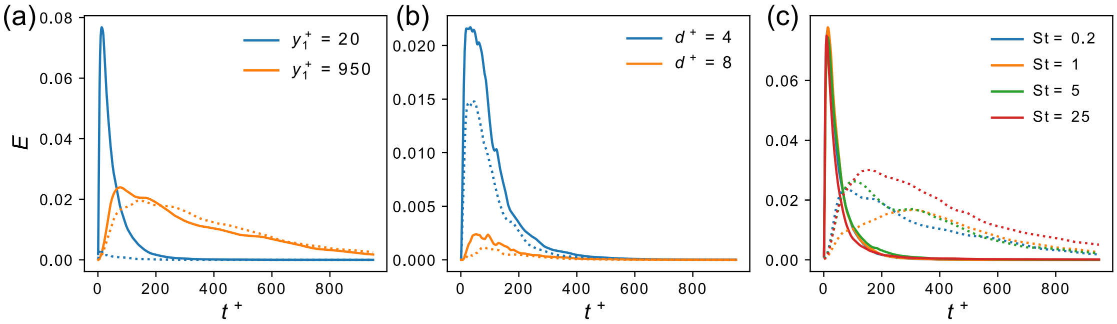

Figure 6.2: a) Evolution of the encounter probability for pairs of sources at two different wall-normal locations, fixed $d^+ = 4$ and $St^+ = 0.2$ (solid lines indicate mixing of streamwise-aligned sources, dashed lines indicate mixing of sources aligned along y); b) $E(t)$ for source pairs at two different distances, $y_1^+ = 100$, $St^+ = 0.2$ (solid lines indicate mixing of streamwise-aligned sources, dashed lines indicate mixing of sources aligned along y); c) $E(t)$ for pairs of sources at fixed $\mathbf{d} = d\hat{\mathbf{e}}_x$, $d^+ = 4$ and varying Stokes number (solid lines are for source pairs at $y_1^+ = 20$, dashed lines at $y_1^+ = 950$.

order to highlight the different properties of mixing found near the wall and at the center of the channel. Figure 6.2(a) shows the encounter probability for two cases. In the first case we set the distance between sources to be $\mathbf{d} = d\hat{\mathbf{e}}_x$, *i.e.* sources are streamwise-aligned, while in the second case the distance is $\mathbf{d} = d\hat{\mathbf{e}}_y$ and, so, sources are y-aligned; in both cases the modulus of the distance between sources is $d^+ = 4$. The figure shows how the encounter probability along the streamwise direction achieves higher values near the wall, while it is weaker away from it. Mixing of sources aligned along the wall-normal direction ($\mathbf{d} = d\hat{\mathbf{e}}_y$) is negligible near the wall (where intense mean shear is present, which drives particle clouds apart) and increases towards the center.

Owing to the quasi-homogeneity of turbulent properties near the center of the channel, the encounter probabilities away from the wall become less and less dependent on direction $\hat{\mathbf{e}}$. On the other hand, the effect of shear towards the walls causes strong mixing of streamwise-aligned sources. Indeed, as these sources have finite size, their shape is sheared and its particles come close to those of the other x-aligned sources.

In order to isolate the influence of mean shear from those of turbulent fluctuations, we also integrated the trajectories using a flow field deputated from all velocity fluctuations and containing only the mean streamwise component $U(y)$, effectively computing encounter properties that are only due to mean shear. Trivially, the encounter probability for y-aligned never becomes nonzero (as particles travel along straight parallel lines). Instead, in the case of streamwise-aligned sources, a peak encounter value approximately equal to $E_{peak} = 0.2$ (with $d^+ = 4$, as is for figure 6.2(a)) is found independently of the y coordinate of release. This is valid across the entire channel height, except the centreline where shear is absent. We note how the time at which the peak is reached depends instead on y. In particular, the larger the shear, the faster the peak is reached. Turbulent velocity fluctuations are the root cause for particle dispersion, thus overall reducing the encounter rate, although this behaviour is also a function of the intensity of mean shear and the size of sources. We note how the effect of mean shear is present at short times because of the finiteness of sources. Its effect would be present at longer times for smaller sources, as they would become enlarged only later by the diffusive action of turbulence.

Figure 6.2(b) shows the effect of the value of d on the encounter probability, at a single y_1 value. Both in the case of streamwise and wall-normal mixing, the larger the distance between sources the smaller is the encounter probability on average. Figure 6.2(c) shows instead the streamwise ($\mathbf{d} = d\hat{\mathbf{e}}_x$, $d^+ = 4$) encounter probability at different Stokes numbers. While near the wall the encounter probability evolves almost independently of the Stokes number (solid lines), near the center of the channel (dotted lines) the effects of particle inertia affect strongly the mixing of particles. Near the wall the short typical timescale of encounters is so short that inertial clustering bears no effect on mixing and, accordingly, no influence of the Stokes number is highlighted. Moreover, particles released near the wall tend to organize in elongated, streamwise-aligned streaks, that exert a predominant influence on mixing.

On the other hand, near the center of the channel (dotted lines) the encounter probability appears to be stronger at $St^+ = 25$ and lower at $St^+ = 1$, with $St^+ = 0.2$ and $St^+ = 5$ having an intermediate behaviour. A different trend is found in the case of y-aligned sources (not shown in the figure), where the encounter probability at $St^+ = 5$ reaches a lower peak than those at the other Stokes numbers. Inertial particles organize into small clusters also near the center of the channel, albeit not in elongated streaks.

The presence of competing phenomena, which initially reduce the mutual distance between particles and later disperse them across wider regions of the domain, results in the encounter probability behaviour. At short time and length scales, the flow features sampled by particle clouds may result in trends opposite to the general one, which is dispersive. Indeed, the short-term action of turbulence makes so that the range between particles shorten, which in turn determines an increase of the encounter probability E. Converging motions inside the flow that drive particles together are only effective locally in reducing overall dispersion, which remains the prevailing mechanism. The peak achieved by the encounter probability during its time evolution is the point when these competing phenomena are in balance, for each pair of sources. Higher peak values E_{peak} indicate that the local action of the flow is able to overcome, at least for a finite amount of time, the long time effects of dispersion which ultimately brings the encounter probability to zero. Similarly, the time t_{peak} at which the peak happens is tightly linked to typical timescales of mixing and dispersion.

6.3.2 Spatial properties of encounters

Owing to the importance of spatial heterogeneity in channel flow, the following section will be devoted to the analysis of spatial properties of encounters.

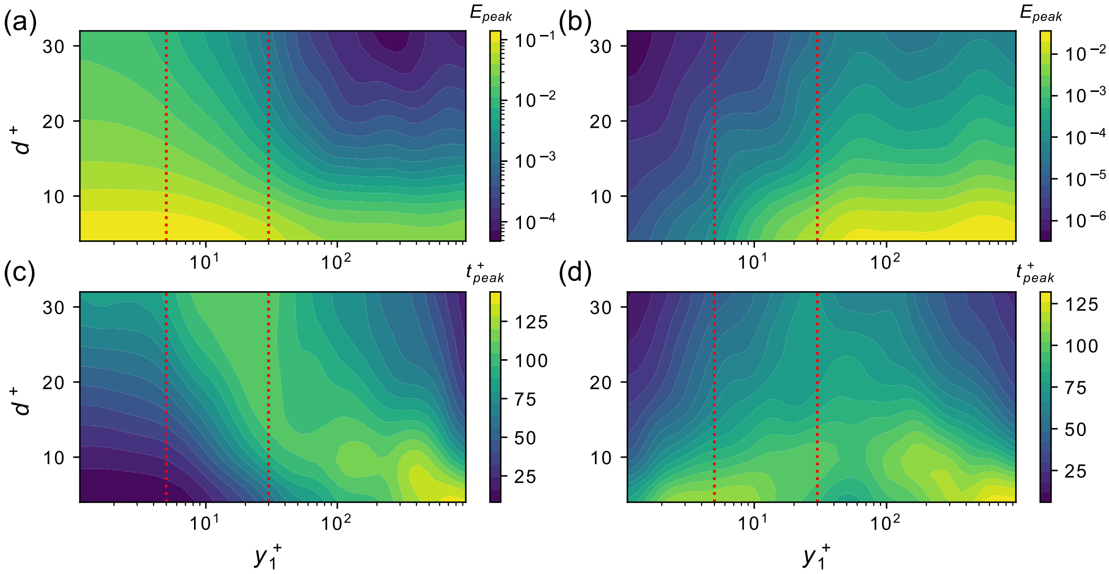

Figure 6.3: Peak encounter probability for streamwise (a) and wall-normal (b) aligned sources as a function of y_1^+ and d^+ at $St^+ = 0.2$; the red lines mark the end of the viscous sublayer at $y^+ = 5$ and of the buffer layer at $t^+ = 30$. Peak time for streamwise (c) and wall-normal (d) aligned sources as a function of y_1^+ and d^+ at $St^+ = 0.2$.

The encounter probability rate (and in turn the peak time) are dependent to both the wall distance of sources y_1^+ and the mutual distance of sources d^+. In figures 6.3(a)-(b) we show the y_1^+ dependence of the streamwise and wall-normal peak encounter probabilities, which we define as the encounter probabilities of sources aligned along $\hat{\mathbf{e}}_x$ and $\hat{\mathbf{e}}_y$, respectively. Mixing of streamwise-aligned sources is stronger near the wall, while mixing of sources aligned along y increases away from it.

Inside the viscous sublayer, where the dispersing action of turbulence is reduced and the mean shear is at a maximum, the streamwise peak encounter is the highest, reaching values of the order of 0.2 for nearby sources. Instead, the wall-normal encounter probability is weaker (the highest peak values are of the order of 0.02), but the region experiencing stronger mixing occupies a large portion of the channel, from the upper limit of the logarithmic region ($y/\delta = 0.1$) up to the centreline.

The mixing of sources aligned along x is hindered only by turbulent diffusion, especially at short times. Instead, for source pairs aligned along $\hat{\mathbf{e}}_y$ also mean shear is present, thus lowering the overall values achieved by E.

Particles released from near wall sources which are aligned along $\hat{\mathbf{e}}_y$ have strongly different mean velocity and are rapidly driven apart, resulting in almost non-existent peak encounter probability. The flatness of the turbulent velocity profile has the effect that outside of the logarithmic region this factor is of reduced importance. Furthermore, E_{peak} is negatively influenced by the distance between sources, which poses an obstacle to particle mixing. Indeed, even if turbulence enables the initial growth of the encounter probability (as particles are dispersed and a fraction of them is driven close together), velocity fluctuations also disperse particles in all directions, thus the distance between sources tends on average to decrease the encounter probability (although it is still possible that some distant particles come in close proximity due to the local features of the velocity field).

The time t_{peak} at which the encounter probability reaches a maximum is shown in figures 6.3(c) and 6.3(d), for streamwise and wall-normal aligned sources, respectively. In the case of sources aligned along x and especially for nearby sources (short d), the stronger intensity of mixing achieved in the near-wall region also corresponds to short peak times. The high intensity mixing taking place near the wall is achieved rapidly by particles that become entrained together in the elongated structures typical of the near-wall region. As the distance between sources increases, longer peak times are observed for pairs of sources located in the buffer layer, although results may be skewed by the small number of encounters taking place.

In the case of y-aligned sources, the peak time is higher near the center of the channel, where also the highest values of E_{peak} are found. Nonetheless, peak times for pairs of sources near the wall are not negligible (especially at higher Stokes numbers as will be detailed in the following). The Lagrangian integral timescale is in general higher at the channel centreline, which in turn influences the encounter peak times The typical timescales of particle motion are higher near the center of the channel, thus resulting in increased peak times for the mixing of both streamwise and wall-normal aligned sources. In general, high values of the peak encounter probability can only be achieved at short times, as otherwise the dispersing action of turbulence would inevitably drive particle apart and avoid the occurrence of short range encounters.

6.3.3 Stokes number effects

Among the main features of turbulence that in our flow case drive particle together (at least locally in space and time) there are the clustering effects linked to particle inertia.

Particle inertia has an effect on the encounter probability, as was shown before

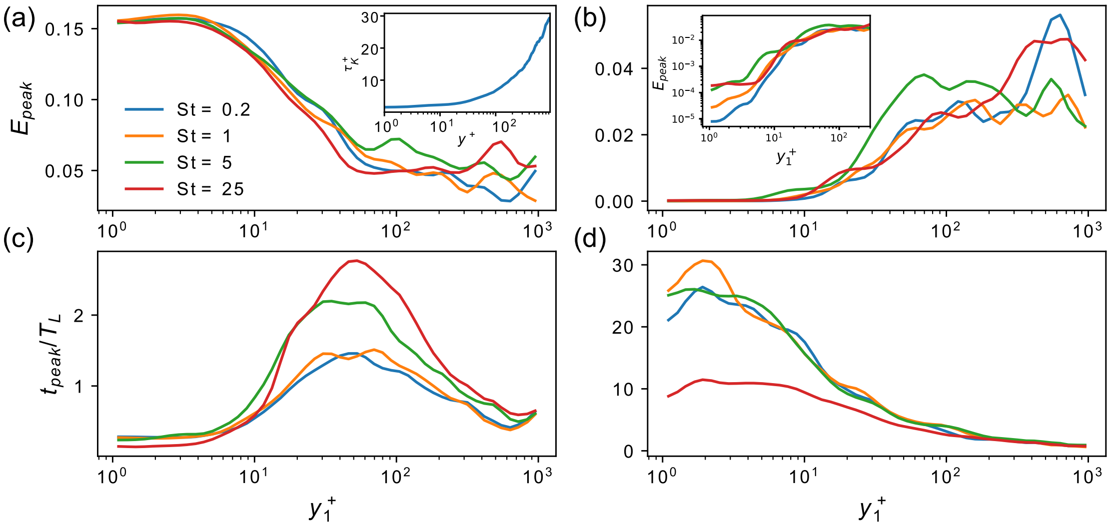

Figure 6.4: Peak streamwise (a) and wall-normal (b) encounter probability E_{peak} with $d^+ = 4$ at different Stokes numbers. The inset in the left panel shows the value of Kolmogorov time τ_p^+ across the channel height, while the inset of the right panel shows a zoom of the data in figure 6.4(b) with logarithmic vertical axis. Peak time of the streamwise (c) and wall-normal (d) encounter probability t_{peak} with $d^+ = 4$ at different Stokes numbers.

in figure 6.2(c), since it affects clustering properties which determine the rate at which subsets of particles become confined to a smaller region of the fluid domain. Figure 6.4 shows a comparison of the peak encounter probability E_{peak} and of its time t_{peak} for different Stokes numbers (at a fixed distance $d^+ = 4$, which is also typical for the behaviour at higher values of d).

The peak encounter rate of source pairs located inside the viscous sublayer is independent of the Stokes number in the streamwise alignment case. On the other hand, farther away from the wall, streamwise-aligned sources (figure 6.4(a)) have slightly stronger peaks at higher Stokes numbers. A noticeable increase of E_{peak} can be identified for particles with $St^+ = 5$ near $y^+ = 100$, while near the center of the channel the same is noticeable for particles with $St^+ = 25$. This behaviour was identified considering the average of several, uncorrelated particle simulations and is therefore not the result of the initial condition imposed on particle velocities.

The encounter probability of sources aligned along y (figure 6.4(b)) depends weakly on the Stokes number at low y_1^+ values, where particles with higher Stokes numbers St^+ also have higher peak encounter rates. The near wall behaviour is shown in the inset of figure 6.4(b) using logarithmic scaling because of the very small values of E attained by y-aligned sources. Higher values of E_{peak} are instead achieved towards the center of the channel for particles with $St^+ = 0.2$ and

$St^+ = 25$. Particles at $St^+ = 5$ show instead higher than normal peak encounter probability at a lower wall-normal coordinate (again $y^+ = 100$).

We recall that particles with values of St_K of the order of unity tend to experience stronger clustering phenomena, and that the values of the Stokes number in Kolmogorov units is related to that in wall units by means of the Kolmogorov timescale expressed in wall units τ_η^+. The inset of figure 6.4(a) shows the value of τ_η^+ across the channel height. It is significant to note that values of the Kolmogorov timescale range from $\tau_\eta^+ \approx 5$ at around $y^+ = 100$ to $\tau_\eta^+ \approx 25$ at around $y^+ = 900$. We can therefore compute the Stokes number scaled with Kolmogorov units, obtaining $St_K = St^+/\tau_\eta^+ \approx 1$ for particles with $St^+ = 5$ located at around $y^+ = 100$. At the centreline again $St_K = St^+/\tau_\eta^+ \approx 1$, but this time for particles with $St^+ = 25$. It is thus very likely that the two slight increases of E_{peak} found at $y^+ = 100$ for particles with $St^+ = 5$ and at $y^+ = 900$ for particles with $St^+ = 25$ can be attributed to inertial clustering (see figures 6.4(a)-(b)). This is only true away from the wall, whereas close to it the organization of particles into elongated structures aligned with the mean flow is the predominant effect leading to encounters (or the absence thereof). Indeed, no effect of particle inertia on the encounter properties is found for source pairs located close to the wall.

Enhanced encounter rates are also present near the center of the channel for particles with $St^+ = 0.2$, even if in this case particles are more akin to tracers given their very low inertia ($St_K \approx 10^{-2}$) and should not experience inertial clustering. After performing additional simulation where the same behaviour was found, we can confirm that the observed increased clustering of low-inertia particles is not due to small sample size. The exact mechanism behind the increased peak encounter probability of particles with $St^+ = 0.2$ at the center of the channel is therefore not associated with inertial clustering and neither with mean shear (which is absent at the centreline).

In order to better represent the relation between the Lagrangian integral timescale of particles and the typical peak times of the encounter probability we show the peak time t_{peak} of the encounter rate for x- and y-aligned sources in figures 6.4(c) and 6.4(d), respectively. The timescale T_L was computed from the streamwise velocity in the case of x-aligned sources and from the wall-normal velocity in the case of y-aligned sources, using

$$T_{L,i}(y) = \int_0^\infty \rho(y,\tau)\mathrm{d}\tau = \int_0^\infty \frac{\langle u_i(y,0)u_i(y,\tau)\rangle}{\sqrt{\langle u_i(y,0)^2\rangle\langle u_i(y,\tau)^2\rangle}}\mathrm{d}\tau, \tag{6.2}$$

where the ensemble average $\langle\cdot\rangle$ is taken over particles released from the same y coordinate, the i-th component of the velocity fluctuation u_i is used and the integral is performed up to the first zero-crossing of the autocorrelation function ρ because of the finiteness of the data.

The very short typical timescale of encounters between streamwise-aligned sources explains the reduced dependence of the encounter peak value E_{peak} on the Stokes number. Indeed, the timescale of encounters is so short that clustering phenomena are yet to gain importance in this case, while a stronger influence is exerted by the initial condition, as particle trajectories are still well into the ballistic regime (*i.e.*, their velocity is strongly correlated with that at release) at the time of peak encounter. The organization of clusters into elongated streaks also plays a role, as the strong trapping of particles into these structures makes so that other forms of clustering become less relevant with respect to the overall mixing process.

The peak time becomes longer than the Lagrangian timescale in the log layer, possibly due to the weaker mean shear which causes slower mixing of streamwise-aligned sources. Towards the center of the channel instead, peak encounters happen on a timescale shorter than the Lagrangian one, even if shear is at a minimum there; accordingly, a more important role in this case is played by turbulent velocity fluctuations and inertial clustering effects. In the case of y-aligned sources instead, mixing near the wall happens on a timescale which is up to two orders of magnitude longer than for x-aligned sources. Indeed, here mean shear strongly inhibits encounters and only turbulent fluctuations may drive particles together (in very small quantities, as shown by the low values of E_{peak} in figure 6.4(b)). The peak time diminishes monotonically towards the center of the channel following the reduction of mean shear. Overall, mixing happens on short timescales whenever the initial velocity of particles already facilitates mixing (as is the case for finite-size, x-aligned sources).

6.3.4 Reynolds number dependence

We now aim to analyse the dependence of the results on the Reynolds number. In order to do so, we performed the same analysis at $\mathrm{Re}_\tau = 590$. To do so, we performed a direct numerical simulation of the same channel flow geometry, integrating the trajectories of particles at different Stokes numbers using the same release configuration as before. The simulation details were given in table 6.1.

Figure 6.5 shows the effects of the lower Reynolds number on main features of particle encounters analysed previously, namely the peak encounter probability E_{peak} and the time at which it happens t_{peak}. We normalize the wall-normal coordinate using the value of δ (the channel half-height). By doing so both configurations are compared in outer units. The almost negligible influence on the value of E_{peak} of the Reynolds number Re_τ can be seen in figures 6.5(a) and 6.5(b), that show the streamwise and wall-normal peak encounter probability, respectively

On the other hand, the peak (see figures 6.5(c) and 6.5(d)) occurs at an earlier time (in wall units) at the lower Reynolds number, both in the case of streamwise mixing for sources located away from the wall and everywhere in the channel in the case of wall-normal mixing. If outer units are used for time (i.e. $t = t^+ u_\tau/\nu$), no Reynolds independence is observed either, and t_{peak} occurs at a later time instead at $\mathrm{Re}_\tau = 590$. Therefore there is no clear scaling of peak times with respect to the

Reynolds number in the range here considered.

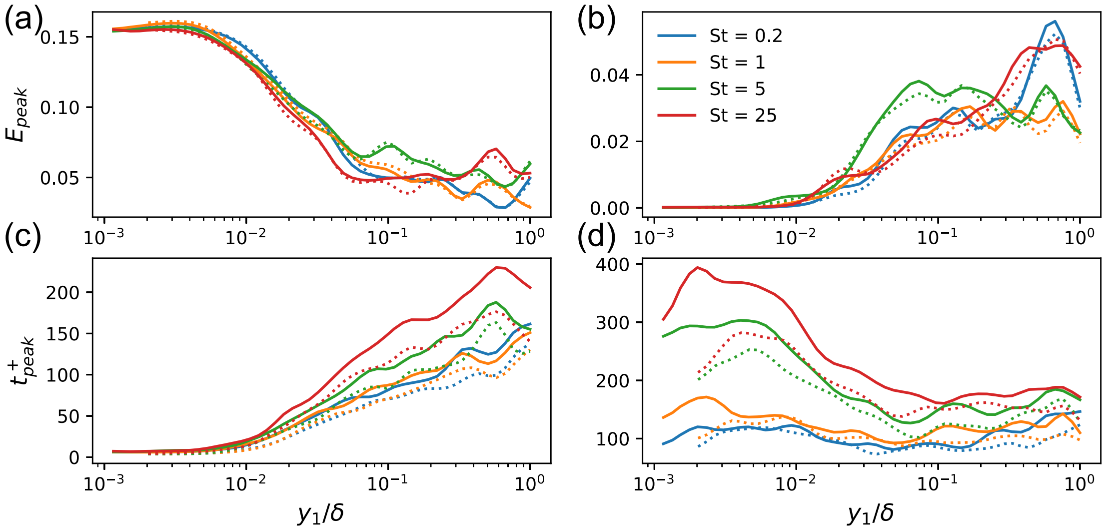

Figure 6.5: Streamwise (a) and wall-normal (b) peak encounter probability at $\mathrm{Re}_\tau = 950$ (solid lines) and $\mathrm{Re}_\tau = 590$ (dotted lines). $d^+ = 4$ in all cases. Peak time of the streamwise (c) and wall-normal (d) encounter probability at $\mathrm{Re}_\tau = 950$ (solid lines) and $\mathrm{Re}_\tau = 590$ (dotted lines).

6.4 Effects of the threshold distance R

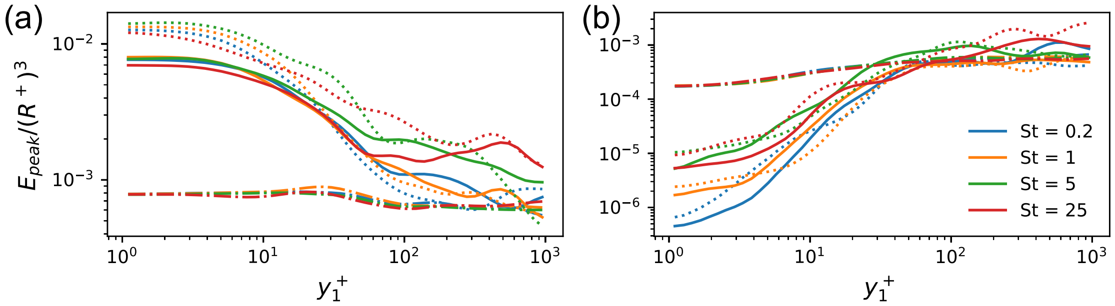

Figure 6.6: Streamwise (a) and wall-normal (b) peak encounter probability at varying Stokes number and $d^+ = 20$. In all panels, solid lines indicate $R^+ = 2$, dotted lines $R^+ = 1$, and dash-dotted lines $R^+ = 8$ (a logarithmic scale is used on the vertical axis).

The value of the threshold is the key sensitivity parameter of the method used in this Chapter to study mixing of inertial particles in channel flow. Accordingly, its value, especially in relation to the length scales typical of inertial clustering of particles with $St > 0$, is instrumental in describing the key interactions between particles.

Therefore, we evaluated the influence of the value of the threshold R by analysing the encounter probability computed using $R^+ = 1$ and $R^+ = 8$, together with the previous results at $R^+ = 2$. Figures 6.6(a) and 6.6(b) show the peak encounter probability normalized by $(R^+)^3$. In all cases, d^+ has been chosen equal to 20 in order to avoid that sources have a nonzero encounter probability at the time of release. Indeed, it can *a priori* be assumed that the encounter rate is proportional to the volume of the sphere of influence surrounding each particle. The larger the volume of the sphere, the larger the number of interactions that will be experienced by each particle.

In reality, the scaling of the peak encounter value with respect to the volume of fluid encompassed by the threshold value is independent of R only in some cases. In the case of streamwise mixing, the scaling is achieved weakly in the center of the channel (where differences between mixing at different St are minimal and appear amplified by the logarithmic scale). Instead, near the wall up to $y^+ = 200$ the encounter probability is not proportional to the cube of R and instead grows more slowly. On the other hand, the collapse of the peak encounter probabilities with different values of the threshold distance is stronger in the case of wall-normal mixing and is attained for source pairs at a lower y^+ coordinate. Furthermore, the peak encounter probability grows faster than R^3 when R is increased, in contrast to what happens for streamwise mixing.

The intense anisotropy of turbulence in the near-wall region and the presence of the wall highly skew mixing processes in certain directions. This may cause in turn a non-homogeneous growth of the encounter probability with respect to the threshold distance R, which grows faster than expected along $\hat{\mathbf{e}}_y$ and slower along $\hat{\mathbf{e}}_x$.

Finally, we recall that, when first defining the threshold distance, we chose a value smaller than the typical features of particle motion we aimed to investigate, most importantly the clusters of inertial particles. Retrospectively we can confirm this choice by noticing that at $R^+ = 8$ the differences between peak encounter probabilities at different Stokes numbers are vanishing, which is a sign that the threshold is larger than the length scales typical of inertial clustering and thus differences due to inertia are not resolved any more. Indeed, this indicates that mixing processes involving particles with larger inertia are not always influenced by inertial clustering, only those happening at sufficiently small length scales. Overall, similar trends are observed across this range of threshold values, although the sensitivity to inertial clustering decreases with increasing values of R.

6.5 Discussion

Through the analysis of short range interactions between inertial particles, carried out by defining an encounter probability, we have shown how mixing is a result of the competing interaction of processes that bring particles together and disperse them, acting on a range of flow scales. The highly anisotropic properties of turbulence near the channel walls reflect onto those of particles. Indeed, mixing of streamwise-aligned sources is far larger than that of wall-normal aligned ones. We correlated this behaviour to the tendency of particles released very close to the wall to organize themselves into elongated streaks aligned with the direction of the mean flow. This kind of organization, which remains coherent for long times, favours the directional imbalance of mixing.

Away from the wall, the encounter probabilities tend to become independent, at least at the lower Stokes numbers, of the direction of alignment of sources, as channel properties also tend to recover isotropy. This is not fully the case for larger inertia particles, where mixing of sources aligned along $\hat{\mathbf{e}}_y$ remains hindered We also computed encounter properties for pairs of sources aligned along the spanwise direction, obtaining results that are quite similar to those obtained from y-aligned sources (although encounter rates near the wall are higher due to the absence of mean shear).

Particle mixing properties do not exhibit a monotonic dependence on inertia, but rather are strongly influenced by the matching between the particle timescale τ_p and the local Kolmogorov timescale. For particles with fixed diameter and density, this matching is achieved on a local basis, as the Kolmogorov timescale is y-dependent. The value of τ_η ranges from values of around $\tau_\eta^+ = 2$ near the wall to around 30 at the center of the channel. As the effects of inertial clustering are the most intense when $St_K = St^+/\tau_\eta^+$ is of order unity, particles experience clustering not only depending on their inertia, but also on their position inside the channel. Indeed, a particle experiencing strong inertial clustering near the center of the channel could move towards the wall and start reacting weakly to turbulent fluctuations as its (local) Stokes number St_K increases. Furthermore, the effects of inertia are different when considering streamwise and y-aligned source pairs. The encounter rate and the medium- to long-term evolution of the mixing appear to be affected by the formation of small-scale clusters, which happens on a short timescale [121].

Near the wall, peak encounter rates of streamwise-aligned sources are achieved in such short times (compared to the integral velocity timescale of particles) that no differences due to the Stokes number arise. On the other hand, for wall-normal-aligned sources, values of E_{peak} are slightly higher at higher Stokes numbers, albeit still very small. Moving farther away from the wall, particles with $St^+ = 5$ first and $St^+ = 25$ afterwards experience the effects of inertial clustering as their typical timescale matches locally that of the flow, possibly resulting in the increases of the peak encounter rate seen near $y^+ = 100$ at $St^+ = 5$ and $y^+ = 900$ at $St^+ = 25$.

Accordingly, two different processes emerge as the cause of the observed trends of the encounter rate. The highly anisotropic features of near-wall turbulence, which result in elongated and highly persistent streaks of particles, determine strong mixing of streamwise-aligned sources (and weak mixing of wall-normal-aligned sources) on timescales so short that inertial effects caused by the matching between the particle response time, τ_p, and the smallest timescales of the flow are negligible. Here it is possible that the relevant timescale of the encounter rate evolution is linked to the Lagrangian integral timescale, highlighting the importance of the initial condition that determines the very-short term evolution of particle motion. On the other hand, away from the wall the properties of the encounter rate are clearly influenced by inertial clustering, with encounter rates increasing where the particle timescale locally matches that of the flow. Therefore, both the Kolmogorov timescale of the flow and the Lagrangian integral timescale of particles influence the encounter rate and, by consequence, mixing.

In order to test the sensitivity of results on the Reynolds number, we simulated mixing at $\mathrm{Re}_\tau = 590$. We observed that the measures presented previously have a reduced sensitivity on the Reynolds number (at least in the range of Re_τ considered), except the fact that the evolution of the encounter probability takes place on a slightly longer timescale. Furthermore, we tested our choice of the threshold value R showing that it is appropriate to capture the organization of particles into clusters due to their inertia. Indeed, at larger values of R most of the differences between particles at different Stokes numbers disappear. Conversely, the variation of the threshold value is a simple way to investigate the typical scale at which inertial clustering effects are relevant for mixing processes.

Chapter 7

Visibility analysis of boundary layer transition

Some of the contents presented in this Chapter have been previously published. Below are provided the references:

D. Perrone, L. Ridolfi, S. Scarsoglio, "Visibility analysis of boundary layer transition", in *Physics of Fluids* **34**, 104104 (2022)

7.1 Rationale

The aim of this Chapter is to outline a method to systematically investigate the properties of time-series extracted from complex flow fields and obtain, through a parametrization comprising of a few key features, the relevant features of such time-series. We study bypass transition to turbulence in a numerically simulated flat plate, zero pressure gradient boundary layer. The numerical data was made available on a publicly accessible online database [120, 159].

Differently from the other studies contained in this thesis, this work does not rely on the Lagrangian viewpoint of fluid dynamics and is instead concerned with fixed point data. Instead, it is linked from a methodological standpoint to the other works which use graph theory as an interpretation framework. In this regard, the aim of this work is to extend the network-based tools developed in this thesis to a wholly different subject and showcase their properties. In a broader sense, the intermittent features of transitional flow that will be the subject of analysis in this chapter will emerge again in the next one, where their influence on particle motion will be addressed.

Several key problems lie in the study of boundary layer transition, some of which we aim to address in this study. The complexity of free-stream transition follows from the large number of flow features that influence the onset of turbulence. A closely related problem to that of predicting transition is that of identifying accurately the separation between the turbulent and the laminar regions, *i.e.* the *turbulent-non turbulent interface* (TNTI). Although we outlined some approaches to the identification of the TNTI in Chapter 2, we aim for a method which does not require the imposition of *a priori* threshold values dependent on the distance from the wall.

We do so by using the visibility graph approach introduced in Chapter 4, which we use to transform the time-series into a graph which, through its key properties, reflects their geometrical features. Because the visibility graph is a tool to investigate the geometry of the time-series, rather than the underlying physical processes, it is of paramount importance to relate the visibility graph properties to the physical nature of the underlying flow, which is done in the context of transitional, highly intermittent flows.

7.2 Methods

7.2.1 Transitional boundary layer flow

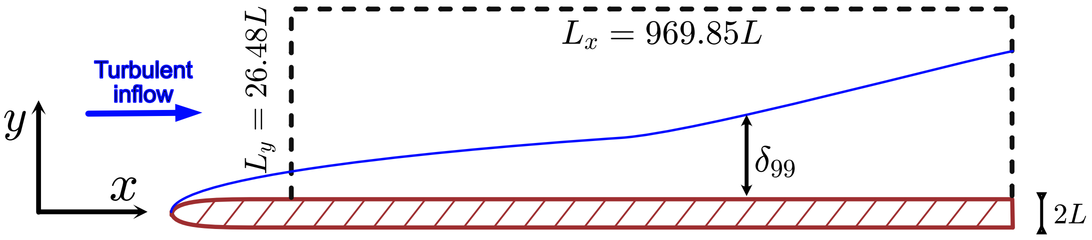

Figure 7.1: Sketch of the fluid domain. The region bounded by the dashed line indicates the stored portion of the domain.

We apply the visibility graph analysis to velocity time-series extracted from a numerically simulated transitional boundary layer. The velocity fields have been made available through the John Hopkins Turbulence Database. The data is obtained via a direct numerical simulation of the flow over a flat plate of thickness $2L$ with an elliptical leading edge and a zero mean pressure gradient across the streamwise x direction. The origin ($x = 0$) of the domain is located at the leading edge of the plate; this location is excluded from the stored dataset, which instead starts at approximately $x = 30L$. A sketch of the simulation domain is shown in figure 7.1. The Reynolds number Re_L based on the half-thickness of the plate, the free-stream velocity U_∞ and the fluid viscosity ν is $Re_L = U_\infty L/\nu = 800$. The flow at the inlet, outside of the boundary layer, is fully turbulent and is generated from a distinct simulation of homogeneous turbulence. The turbulence intensity at the inlet is about 3%, which is enough to trigger bypass transition. At the lower boundary, which is a solid wall, the no-slip condition is imposed, while along the spanwise direction periodicity is used. At the top of the domain the boundary condition is actively controlled to satisfy continuity and keep the zero pressure gradient. The size of the domain, with respect to the plate half-thickness is $L_x \times L_y \times L_z = (969.8465 \times 26.4844 \times 240)\,L$, with y and z being the wall-normal and spanwise directions, respectively. The number of grid points in physical space at which the solution is stored is $N_x \times N_y \times N_z = 3320 \times 224 \times 2048$. Each time series is composed of $N_t = 4701$ time-steps for a total time stored $T = 1175L/U_\infty$; the resulting time step is $\Delta t = 0.25L/U_\infty$. A snapshot of the streamwise velocity field at $y = 0.43$ is shown in figure 7.2. The main features of bypass transition are clearly identifiable, namely the streamwise-aligned streaks, the formation of turbulent spots and the general onset to turbulence, whose location varies with time. Further details on the numerical procedure employed can be found elsewhere [230, 120, 159].

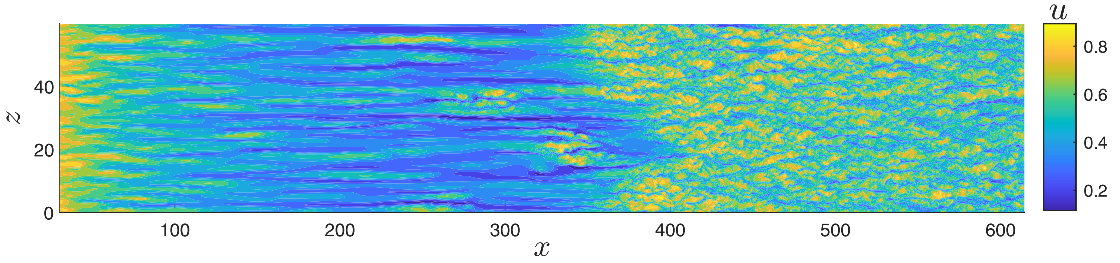

Figure 7.2: Top view of the boundary layer at $y = 0.48$, $t = 0$, streamwise velocity.

7.2.2 Visibility analysis of time-series

The application of the visibility graph formalism to time-series is known to preserve their geometrical structure, in the sense that a relation between time-series properties and those of the visibility graph can be found. As an example, periodic time-series result in regular visibility graphs, random series in random graphs, and fractal series result in graphs where scale-free features are present. The main rationale behind the application of the visibility graph to fluid dynamics stems from the need to provide a treatable insight on turbulent or transitional time-series, which are highly complex and need a very fine temporal resolution to be adequately represented (especially at high Reynolds numbers). By construction, the visibility graph is invariant under horizontal and vertical rescaling of the time-series; as such, the overall amplitude of the time-series has no effect on the derived network measures. On the contrary, the visibility analysis is highly sensitive to the interplay of different scales inside the time-series. As will be detailed in the following, the network measures applied to the visibility graph have the ability to convey the entity of this interplay.

Aiming to understand the influence of time-series features onto the visibility

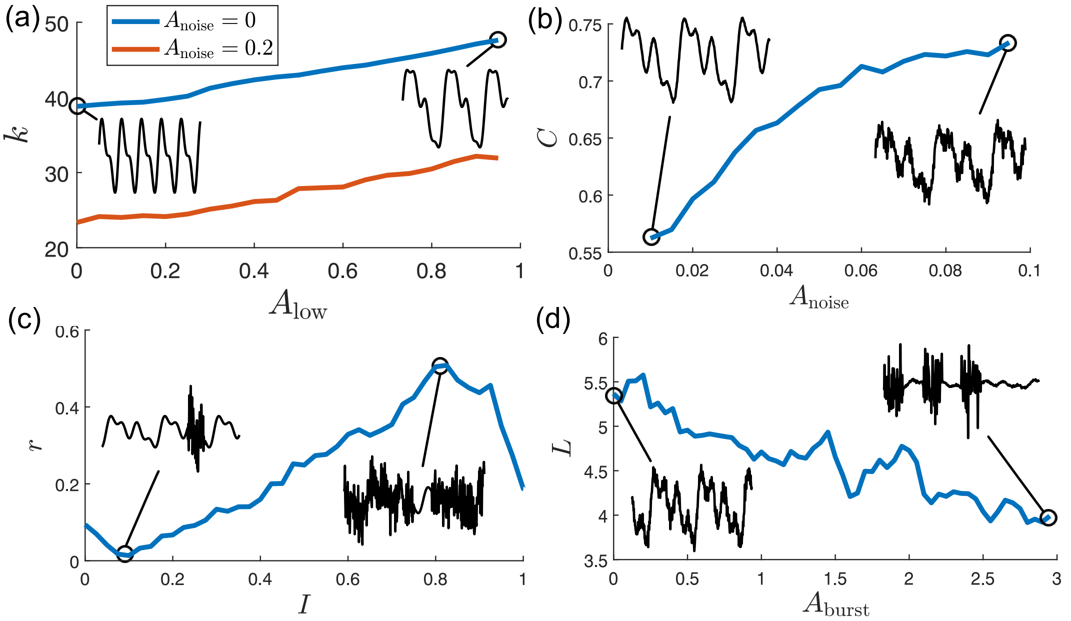

Figure 7.3: Visibility parameters of the synthetic time-series: a) average degree K with respect to the amplitude of the lowest frequency component of the time-series A_{low}; b) clustering coefficient C with respect to the amplitude of noise A_{noise}; c) assortativity r with respect to the intermittency I; d) average path length L with respect to the amplitude A_{burst} of localized bursts ($I = 0.33$). Relevant time-series are plotted as insets.

graph, we generated a synthetic time-series which resembles the ones obtained from the transitional flow data. The benefit in this case is the ability to arbitrarily modify the parameters of the synthetic time-series and evaluate their influence on the graph separately. The synthetic time-series is generated by superimposing three out of phase sinusoidal components with frequency f_i and amplitude ϕ_i ($i =$ low, mid, high), a small-scale Gaussian noise and a larger amplitude Gaussian noise that has a discontinuous support (*i.e.*, that is not defined at all time instants but only on a subset of them). The synthetic time-series is

$$u(t) = \sum_{i=\mathrm{low,mid,high}} A_i \sin\left(f_i t + \phi_i\right) + A_{\mathrm{noise}} w_1(t) + A_{\mathrm{burst}} w_2(t), \tag{7.1}$$

where w_1 and w_2 are white Gaussian noises and w_2 is nonzero only on a fraction I of the duration of the time-series, which corresponds to the intermittency of the signal. The support for the intermittent regions of the synthetic time-series is chosen at random, with some degree of spatial coherence.

In a visibility graph, the nodes situated in large, convex portion of the time-series have a direct line of sight with a larger number of other nodes, thus having large degree. Overall, the mean degree

$$K = \frac{1}{N}\sum_{i=1}^{N} k_i = \frac{1}{N(N-1)}\sum_{i,j} A_{ij} \tag{7.2}$$

of the visibility graph is tightly connected to the amplitude A_{low} of the lowest frequency components in the time-series, *i.e.*, those with the largest scale. All the panels in figure 7.3 show some of the synthetic time-series used to compute the visibility graph measures. Figure 7.3(a) shows how the degree grows as the low-frequency component becomes more important. Indeed, the prominence of peaks spaced far apart increases the overall number of links and thus the mean degree; also, we found that the mean degree is inversely proportional to the frequency f_{low}.

The clustering coefficient also depends strongly on the local convexity of the time-series around a given node. Differently from the degree centrality, the amount of connected triples and triangles is mostly determined by the time-steps immediately adjacent to the one considered, as it is far more frequent to find connections in triples of temporally close nodes. As such, the global average

$$C = \frac{1}{N}\sum_{i=1}^{N} c_i \in [0,\ 1] \tag{7.3}$$

of the clustering coefficient quantifies the importance of the small-scale components of the time-series [90]. In particular, we observe that the clustering coefficient increases as the amplitude of the small-scale Gaussian noise A_{noise} in the synthetic time-series increases (see figure 7.3(b)).

The visibility graph is also suited towards the analysis of the vertical separation, *i.e.*, the presence of components whose amplitude is markedly different in adjacent regions of the time-series. Iacobello et al. [87] gave an extended discussion regarding the ability of the assortativity coefficient r to discern between time-series whose amplitude is homogeneous over time and those that are not. In particular, when the amplitude of the time-series is homogeneous and there are no outliers, it is more probable that similar nodes are connected, leading to highly assortative networks. This behaviour is of outstanding importance in the study of transitional time-series, which are strongly characterized by their intermittent behaviour in the region where turbulence is not fully developed.

Varying the intermittency in the synthetic time-series (that is the fraction of time in which large-amplitude Gaussian noise is present) allowed us to study the behaviour of the assortativity, as is shown in figure 7.3(c). The simulated turbulent component is highly fluctuating, but is still somewhat homogeneous with respect to the underlying laminar component. Accordingly, the assortativity is high. As the intermittency grows the network becomes increasingly assortative until the intermittency reaches unity (the series becomes fully turbulent), where the assortativity drops significantly. As already stated, the visibility graph is highly sensitive to the interplay of the different scales rather than to their actual amplitude. When the intermittency reaches unity, the laminar component disappears from the time-series and the heterogeneity of the turbulent component leads to a decrease of the assortativity.

Finally, the average path length is a measure of the topological distance between nodes; it follows easily from this consideration that the presence of localized peaks determines a decrease of the value of L, as long-distance nodes are more easily connected. As shown in figure 7.3(d), the average path length decreases when the amplitude of the temporally localized Gaussian noise in the synthetic time-series increases.

7.3 Results

7.3.1 Network measures

We computed the visibility graph from time-series of the streamwise velocity u from a set of points in the flow domain. In particular, for each $(x,\, y)$ coordinate, we considered time-series from $N_z = 120$ equally spaced points across the homogeneous z direction of the domain. For each visibility graph, we computed the relevant network measures; in the following, we will provide results averaged along z in order to achieve statistical accuracy.

The four visibility graph measures (K, C, r and L) are shown over a grid of points that comprises the regions of the boundary layer experiencing bypass transition, in figures 7.4(a)-(d). We can use these values, together with their physical significance, to provide insight on the boundary layer time-series properties.

The turbulent fluctuations in the free stream outside of the boundary layer induce low-frequency, high-amplitude fluctuations of the streamwise velocity in the near wall region. The degree centrality (figure 7.4(a)), which is sensitive to these low-frequency components, has a marked peak near $(x,\, y) = (200,\, 0.2)L$. This is the region where the low-frequency amplification induced by shear-sheltering appears to be at a maximum. Downstream, the clustering coefficient (shown in figure 7.4(b)) increases. As the low frequency streaks undergo secondary instability and therefore initiate the energy cascade towards smaller flow scales, the time-series exhibits more and more small-scale features, which in turn are captured by the clustering coefficient. We locate the start of the streak breakdown process at around $x = 300L$ in the innermost portion of the boundary layer, while at higher y values the high-frequency components of the time-series acquire stronger importance further downstream. Indeed, the first occurrences of turbulence appear to be located in the innermost portion of the boundary layer.

We also note that, in the region where streaks are generated, the clustering coefficient is at a minimum, as the high-frequency components of the freestream turbulence are filtered out and do not exert forcing on the boundary layer flow.

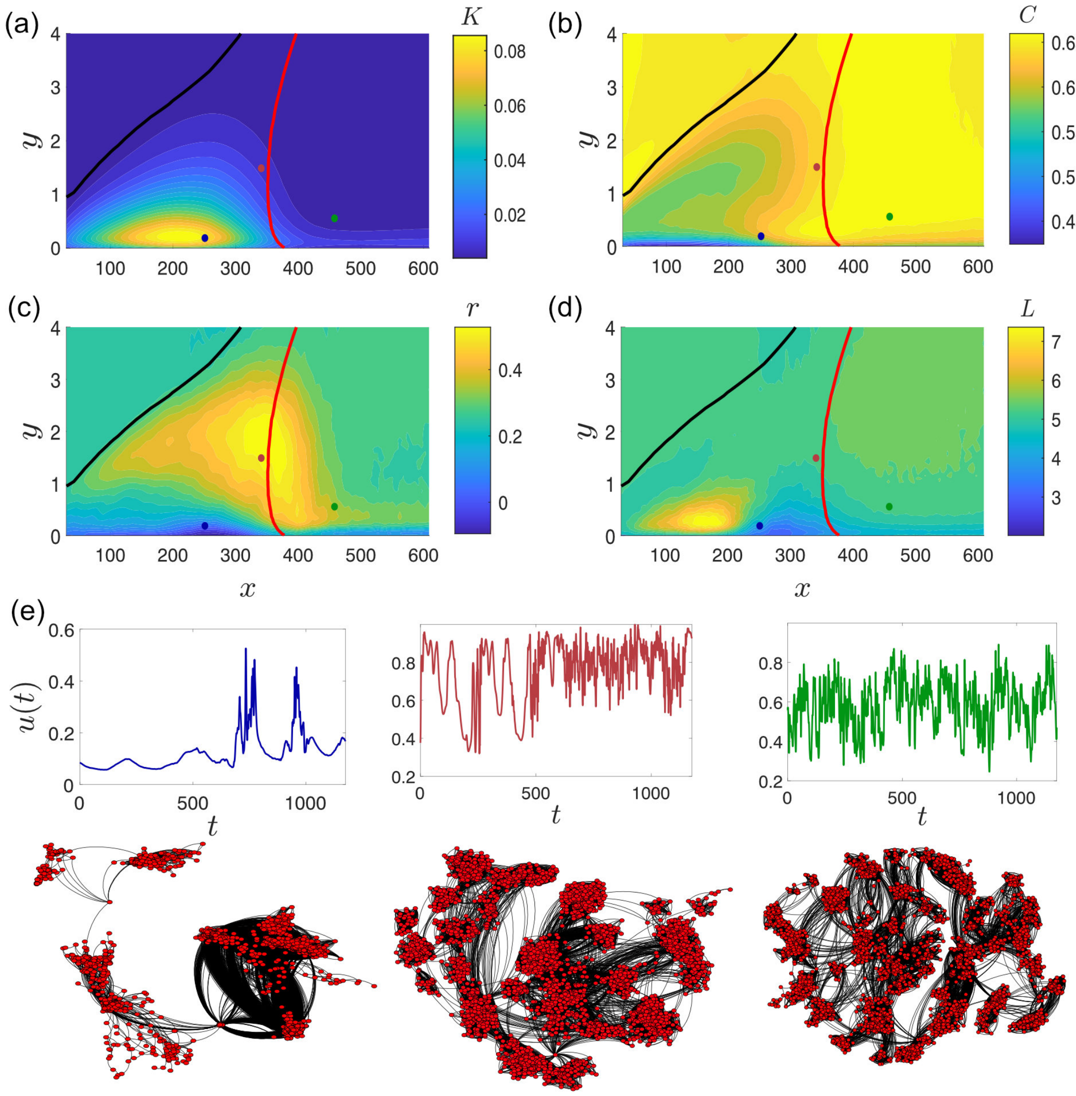

Figure 7.4: Visibility graph measures in the transitional boundary layer: a) Average degree, b) clustering coefficient, c) assortativity and d) average path length. The boundary layer height δ_{99} is shown in black, while the average position of the TNTI $\bar{x}_{\mathrm{TNTI}}(y)$ is shown in red. Panel e) shows three time-series sampled at the corresponding, color-coded points of the domain; the spanwise coordinate is $z = 13.95$ for all time-series. Below each time-series, the corresponding visibility graph is drawn by a force-directed algorithm.

Additionally, the clustering coefficient in the turbulent region of the boundary layer is slightly higher than in the free-stream, indicating some difference in the structure of turbulence (regardless of the amplitude, which is neglected by the visibility graph).

We now use the assortativity and the average path length to characterize the intermittent behaviour which is typical of the region immediately preceding the full onset of turbulence. We show both these measures in figures 7.4(c)-(d). The fixed points at which time-series are taken are traversed by turbulent spots. Also, the frequency at which turbulence appears at a fixed-point in space depends on the streamwise coordinate and increases downstream. The ability of the assortativity to distinguish between intermittent time-series (even with high intermittency values) and fully turbulent ones allows us to identify a region, located prior to the fully developed turbulent boundary layer, where intermittency is at a maximum (but still not unity, which would correspond to turbulence). This region with high assortativity appears, from the spatial point of view, as an almost vertical front located at around $x = 380L$, which is followed by a region where the assortativity decreases rapidly. We hypothesize that the region of maximum assortativity is the region which hosts the turbulent-non turbulent interface.

The average path length has a maximum in the streaky region, where the low-frequency fluctuations of the streamwise velocity present no clear, localized peak. Instead, there is a minimum at around $x = 300L$ and very low y values. The minimum indicates that time-series in this region present localized peaks and a somewhat reduced intermittency (the assortativity is also very low in the same region, indicating a strongly heterogeneous time-series). It is interesting to note that at slightly higher x coordinates the strong increase of the clustering coefficient takes place; indeed, it is the expansion and coalescence of localized spots that generates complete transition to turbulence.

Figure 7.4(e) shows three time-series extracted from the corresponding, color-coded, points indicated in figures 7.4(a)-(d) and at $z = 13.95$ and, below, the corresponding visibility graph plotted with a force-directed algorithm [129]. The leftmost time-series is taken from the region of the domain in which turbulent spots are present. The low values of L are linked with the presence of peaks, which are evident in the graph plot as single nodes connected with large, separate clusters (which are the time steps to the left and to the right of each peak). The presence of the laminar regions determines instead the high values of the mean degree. Aiming to quantify the community organization inside the network with respect to the phases of transition, we applied the Louvain partitioning algorithm and computed the average size of communities [24]. In the case of the leftmost time-series, the average cluster comprises of 522 nodes.

In the central time-series and in its corresponding graph plot, taken near the turbulent-non turbulent interface where the assortativity r is at a maximum, the hub-spoke organization typical of the spotty time-series is less evident, but clusters still appear visibly larger than in the fully turbulent case due to the contribution of persistent low frequency components (the average cluster size is 204). Owing to the remaining contribution of some low-frequency component, the average degree centrality is also larger than in the fully turbulent case.

Finally, in the rightmost time-series, taken from a region where turbulence is fully developed, the size of clusters is much smaller (on average, they comprise 130 nodes). Conversely, here the clustering coefficient is at a maximum as the high-frequency components are predominant.

To further complement our results, we added to the plots in figure 7.4 the boundary layer height δ_{99} (black curves), which is the y coordinate at which the streamwise average velocity is 99% the freestream velocity, and an approximate location of the TNTI (red curves). To find the location of the turbulent-non turbulent interface across the wall-normal coordinate y we used the procedure described in Chapter 2, involving the application of Otsu's method to the sum of the wall-normal and spanwise velocity fluctuations $|v'| + |w'|$ at each wall-normal height [143].

After we obtained the spatial profile of the TNTI as a surface $x_{\mathrm{TNTI}}(y, z, t)$ at different times we averaged the results along time and along z to obtain an expected average profile of the TNTI, $\bar{x}_{\mathrm{TNTI}}(y)$.

First, we note that the variation of the network measures takes place inside the boundary layer, at y coordinates lower than δ_{99}, while in the free-stream the measures remain mostly stationary. Moreover, the expected position of the turbulent-non turbulent interface using Otsu's thresholding is clearly superimposable to the regions where network measures signal the transition to fully developed turbulence. In particular, the region of maximum assortativity and the TNTI intersect in a wide range of y coordinates, indicating that the assortativity measures, as was hypothesized before, incipient transition. It is also worth noting that the spike of the clustering coefficient in the innermost region of the boundary layer is located slightly before the expected location of the interface, possibly indicating that to some extent the transfer of energy to smaller scales precedes full transition. The benefit in this case is that the visibility graph approach is the same for all y coordinates, differently from the application of Otsu's method.

7.3.2 Sensitivity analysis

The visibility graph was proved to be an insightful tool for the analysis of time-series. Still, in the previous section it was applied to data obtained from high resolution numerical simulation, which is fully resolved and contains complete information regarding all flow scales. To evaluate the ability of the visibility graph to analyse under-resolved data, we will provide results that are averaged along a reduced number of points along z and results obtained using subsampled time-series. In particular, the analysis of subsampled time-series is relevant because directly applies to many contexts where fully-resolved data may not be available, as are experiments or large eddy simulations.

Panels from figure 7.5(a) show the network measures averaged using only 10 points along z (instead of $N_z = 120$ used precedently); we also plotted the location of the TNTI computed using Otsu's method and its standard deviation along z

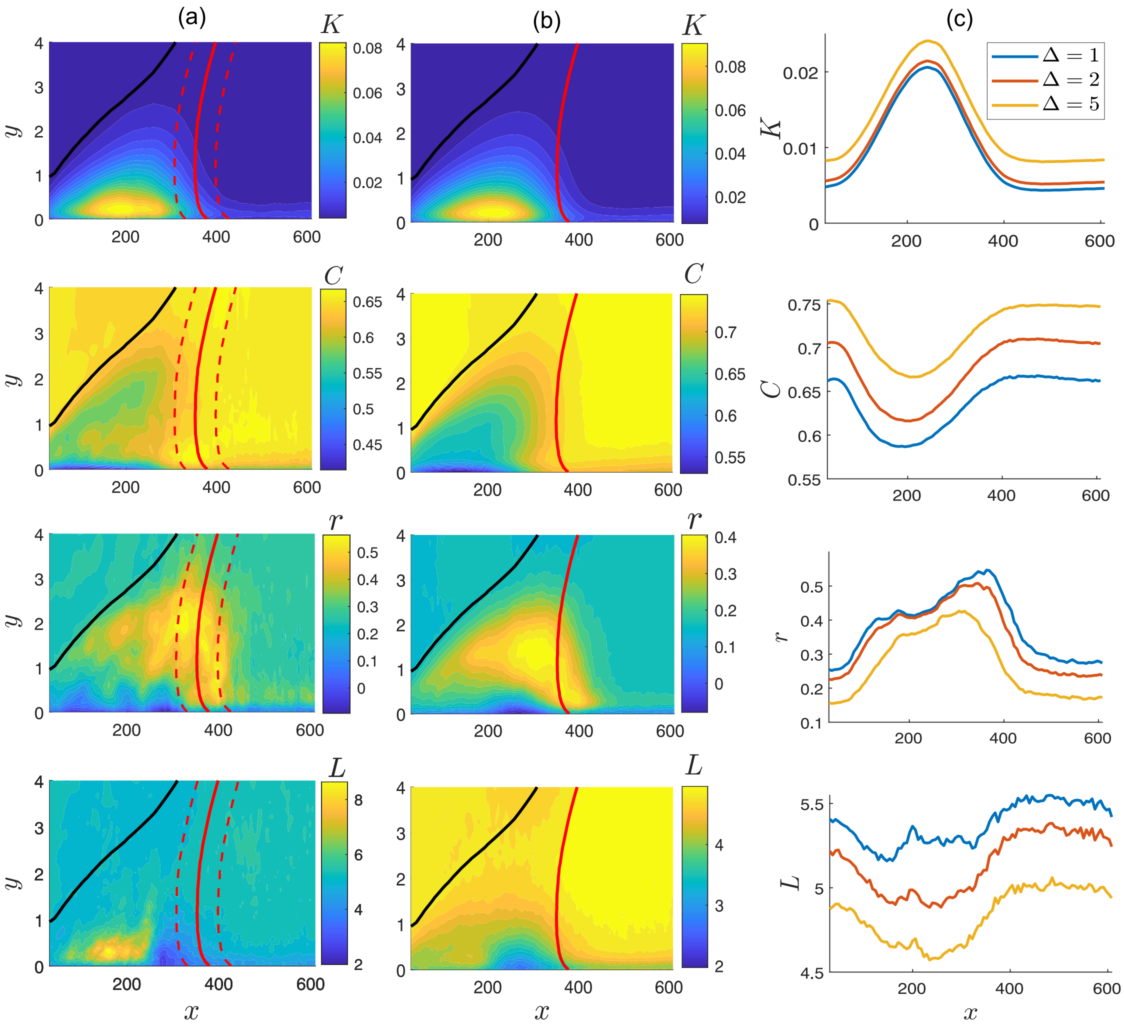

Figure 7.5: a) Degree, clustering coefficient, assortativity and average path length of the visibility graph at a fixed spanwise coordinate ($z = 13.95$); black lines indicate the values of δ_{99}, while the red lines the average position of the TNTI and the dashed red lines its standard deviation along z. b) Measures for networks obtained from subsampled time-series with $\Delta = 5$ (results are now averaged along $N_z = 120$ points in the spanwise direction). c) Network measures from the subsampled time-series at $y = 0.98$ with different values of the subsampling parameter Δ (again, results are averaged along $N_z = 120$ points)

(dashed lines). The overall trends of the measures across the domain are preserved. In particular, a peak of the assortativity is still present near the transition region, making this measure suitable for a local determination of the TNTI. The network representation shows good statistical accuracy even when a lesser number of sample points is used.

Figures 7.5(b)-(c) show the network measures obtained from subsampled time-series. Starting from the full time-series, comprising of N_t time-steps, we constructed the subsampled time-series by taking one out of Δ points, so that $u_i^{\Delta} = u_{\Delta i}$. Δ is the subsampling parameter. We thus obtained subsampled time-series which are effectively deprived of the highest frequency components. Concerning the visibility graph itself, the effect of the subsampling is a consequence of both the elimination of a fraction of the original data and of the reduction in the number of nodes, which is in general not predictable *a priori*.

In figure 7.5(b), the four network measures (K, C, r and L) obtained from a subsampled time-series with $\Delta = 5$ are shown. The degree centrality has been normalized with the correct number of nodes, which is N_t/Δ. Even if 80% of the original information contained in the time-series is lost, the visibility measures of the subsampled time-series are tightly related to those of the full ones. All the previously identified spatial patterns correctly reported by the visibility graph after the subsampling. The degree centrality is left mostly unchanged, as the subsampling procedure affects only slightly the larger timescale in the time-series (which are the ones that influence the degree centrality); moreover, the decrease of the number of nodes can be fully accounted for by normalization. The clustering coefficient, while retaining the previously found spatial trends (most notably, the presence of a minimum around $x = 200$), increases everywhere in the domain. While the removal of the high-frequency components triggers a decrease of the clustering coefficient at a fixed number of time-steps (see figure 7.3(b)), this seems to not be the case when the number of time-steps is decreased. Moreover, it appears that the increase of the clustering coefficient has the same magnitude in regions of the domain where the time-series are dominated by either low- or high-frequency components, indicating that the reduction of the number of nodes has the most prominent effect on the visibility graph structure. Indeed, as the visibility graph is scale invariant, the removal of high-frequency components by itself is not sufficient to significantly alter its properties, as the components that where not removed now appear as high-frequency themselves in the perspective of the visibility graph.

The assortativity appears to be slightly reduced everywhere, although not by much. Moreover, the spatial location of its maximum, which we correlated to the location of the TNTI, appears to be located at slightly lower x coordinates. It is possible that this is due to the loss of information occurring because of the subsampling, which makes it impossible to distinguish a time-series with a high value of the intermittency I from a fully turbulent one. Finally, the average path length L diminishes everywhere as the lesser number of nodes is correlated to a reduction of the shortest path lengths. Around $x = 200$ the average path length of the full time-series presents a peak, which is progressively smoothed as the subsampling parameter Δ increases. In that region of the domain the dynamics of the flow is dominated by low-frequency streaks and turbulent spots are mostly yet to appear, which, in the fully sampled case, leads to high values of L. It appears that fine-structure changes like those induced by the subsampling considerably affect the structure of the visibility graph obtained from time-series of streaky flow.

The panels of figure 7.5(c) show the network measures at a fixed wall-normal coordinate ($y = 0.98$) and two different subsampling parameters, $\Delta = 2$ and 5. With $\Delta = 2$, even if half the information of the original time-series is lost, the network properties behave in a similar manner to the fully sampled ones. In particular, we note that the assortativity r is mostly unchanged and the peak is located at the same x-location as in the fully sampled case. Moreover, a peak of L in the streaky region is still present, indicating that the effects of the subsampling with $\Delta = 2$ are mostly due to the halving of the number of nodes.

We performed the same analysis at higher values of Δ (up to $\Delta = 20$, not shown here) obtaining a progressive loss of quality in the network measures. This is indeed expected, as the loss of information due to the subsampling inevitably reflects on the quality of the visibility graph analysis. Nonetheless, if the sampling guarantees that all the relevant scales of the flow are retained, the qualitative behavior of the results obtained through the visibility graph is independent from the exact value of the sampling rate.

7.4 Discussion

The results delineated in this Chapter contribute to assess the properties of the visibility graph and of its application to time-series obtained from flow data. The visibility graph methodology appears suited toward the analysis of flows with abrupt changes in their dynamics, as it is able to capture the transition from the laminar state to the turbulent one, with particular precision regarding the highly intermittent states in between. We have found a connection between the visibility graph properties and those of the underlying time-series, noting in particular that intemittent behaviour in the flow data corresponds to assortative networks, that is, networks in which links appear more frequently between nodes with similar degrees.

It is of particular importance that the visibility graph is able to provide a measure of the approximate position of the TNTI which, differently from traditional methods, is defined independently of the distance from the wall and is resilient to under-resolved input data. Furthermore, as the assortativity coefficient is bounded in the interval $[-1, 1]$, its analysis can be readily extended to other flow cases without much reassessment of its properties. More complex flow settings should not pose significant problems to the application of the visibility approach, nor the undersampling of the data (which is possible in experiments) affects significantly the results.

All four network parameters considered in this chapter were able to describe separate features of the time-series, effectively condensing the information contained in $N_t = 4701$ data points into a reduced set of scalar measures. While it holds true that the visibility graph is a tool geared towards the analysis of the geometrical appearance of time-series, we note that it is particularly suited to analyse the geometrical features spurring from the interaction of multiscale components, which is a fundamental features of turbulent flows. Because of this, it was possible to infer the relation between network metrics and time-series properties and quantify the arising of irreversibility due to transition to turbulence.

Chapter 8

Shape evolution of particle puffs in transitional channel flow

Some of the contents presented in this Chapter have been previously published. Below are provided the references:

D. Perrone, J.G.M. Kuerten, L. Ridolfi, S. Scarsoglio, "Spatio-temporal evolution of particle puffs in transitional channel flow", in *Physics of Fluids* **35**, 124110 (2023)

8.1 Rationale

In this Chapter the deformation of particle puffs released in a transitional channel flow will be studied. When considering multiparticle dispersion, the simplest case is that of particle pairs, whose relative motion is solely determined by the flow features at the scale of their mutual distance. Instead, puffs comprising of a large number of particles are subject to a multitude of flow scales up to the size of the puff. Works concerning the analysis of puffs through integration of the trajectories of their particles are scarce and focus on homogeneous turbulence. In this case, the effect of the flow on the shape evolution of puffs does not depend on position and, on average, puffs do not orient themselves along a preferential direction. Still, due to small scale stretching phenomena (which are linked to continuity), the initial deformation of individual puffs is highly anisotropic [21]. Puffs take an elongated shape at short times (comparable to the Kolmogorov timescale) and only after return to anisotropy due to larger scale dispersion.

The focus of this chapter is instead on the motion of puffs in a transitional channel flow. The flow in a channel undergoing transition is non homogeneous both along the wall-normal direction (because of the no-slip boundary, which originates the presence of mean shear), and along the streamwise direction, where the flow evolves from laminar to turbulent. Because of this flow case, puffs become also subject to mean shear of varying intensity (depending on wall distance), to the typical flow structures of wall-bounded flows, and to the different features of perturbed laminar flow, transitional flow and fully developed turbulence.

We study the motion of puffs released at several locations inside the channel, investigating their behaviour with respect to the point they are released at (both along the wall-normal and the streamwise directions). Furthermore, because the shape evolution of puffs is heavily conditioned by their overall size, we analyse puffs of different initial sizes r_0, so that the multiscale nature of transition and turbulence is properly accounted for.

To study the shape of puffs we compute the principal axes of the approximating ellipsoid of each particle cloud and define simplified measures of their size and elongation. We describe these methods and the numerical simulation details in section 8.2. Subsequently, we present the results in section 8.3 and give a discussion in section 8.4.

8.2 Methods

8.2.1 Numerical simulation of transitional channel flow

We run a simulation of transitional channel flow using a pseudospectral direct numerical simulation code in conjunction with a method to set the boundary conditions that allow spatially developing flow. For the simulation, we use the same code that was used in chapters 5-6, which employs Fourier polynomials along the x (streamwise) and z (spanwise) directions. The main parameters are shown in table 8.1. We chose the Reynolds number so that, after the transitional phase, the channel achieves stable turbulence.

Table 8.1: Main parameters for the direct numerical simulations of transitional channel flow: domain size $L_x \times L_y \times L_z$, number of polynomials used for the simulation $N_x \times N_y \times N_z$ and time step of the simulation Δt

Re_b	$L_x \times L_y \times L_z$	$N_x \times N_y \times N_z$	Δt
3333	$32\pi\delta \times 2\delta \times \pi\delta$	$6144 \times 192 \times 192$	0.00025

Concerning the boundary conditions along the streamwise direction, we employ the fringe forcing method already introduced in chapter 3, which consists of imposing a distributed forcing at the end of the domain in order to achieve the desired inflow condition at the periodic inlet. As a distributed boundary condition, we impose a superimposition of the laminar profile and of two-dimensional and three-dimensional, spatially evolving solutions of the Orr-Sommerfeld and Squire equations, obtained by solving 3.37-3.38 with $\beta = 0$ and $\beta = 2$, respectively. The initial amplitude of the two- and three-dimensional perturbations is set to 6% and 0.2% of the centerline velocity U_c. While these values are higher than what is found in similar simulations of temporally evolving channel flow, these values allow transition to happen in a shorter length, thus reducing the computational cost.

With reference to equation 3.35, the main parameters of the forcing method are provided in table 8.2. The bulk Reynolds number Re_b is kept constant by the fringe forcing. Figure 3.7 shows one instantaneous velocity field obtained from this simulation, along with the evolution of the friction Reynolds number Re_τ. Figure 8.1 shows instead the mean streamwise velocity extracted at different locations in the domain, showing the evolution from the laminar profile to the turbulent one.

Finally, particle trajectories are integrated with the same trilinear scheme that was used in the previous chapters. After particles exit the physical portion of the domain and enter the fringe region, their behaviour is no longer physical.

Table 8.2: Parameters used for the fringe forcing method (see equation 3.35

$\lambda_{\max}$	x_{start}	x_{start}	Δ_{rise}	Δ_{fall}
8000	$0.8L_x$	L_x	$0.12L_x$	$0.04L_x$

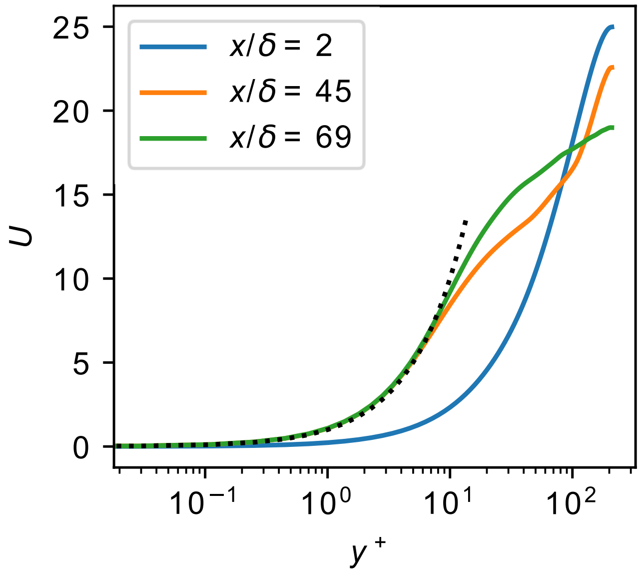

Figure 8.1: Mean longitudinal velocity profiles at different streamwise locations; dotted lines: linear velocity profile at low y^+.

8.2.2 Measuring particle puff deformation

We release puffs of particles, composed of $N_p = 1024$ tracers disposed uniformly at random on a spherical surface of radius r_0. Since we compute the trajectory of each tracer using the time-dependent velocity field of the simulation, we are able to obtain the shape of puffs at all times after release. Puffs are disposed on an equispaced grid comprising of 48 different locations along both x and y, resulting in 2304 distinct release locations covering the complete domain. For each location, we released several ($N = 128$) puffs at different times in order to obtain statistically significant results, making sure that the spacing between realizations was enough to avoid correlation issues.

To measure the deformation of each puff we compute the gyration tensor, that is the covariance matrix of particle positions. The gyration tensor $\mathbf{G}(t)$ is defined as

$$G_{ij}(t) = \frac{1}{N_p} \sum_{n=1}^{N_p} (r_i^n(t) - \langle r_i \rangle)(r_j^n(t) - \langle r_j \rangle), \tag{8.1}$$

where $r_{i,n}(t)$ is the i-th component of the position of the n-th particle of the puff at time t, and $\langle r_i \rangle = \frac{1}{N_p} \sum_{n=1}^{N_p} r_{i,n}(t)$ is the coordinate of the center of mass. The eigenvalues λ_i of the gyration tensor $G(t)$ are non-negative and can be used to obtain information regarding the shape of the puff. The trace of the gyration tensor (which is equal to the sum of its eigenvalues) is equal to the squared radius of gyration $R^2(t)$, which measures puff size. A similar value is obtained when computing the mean distance of particles from the center of mass of the puff.

The asphericity

$$A(t) = \sum_{i=1}^{3} \frac{\left(\lambda_i(t) - \overline{\lambda}(t)\right)^2}{6\overline{\lambda}^2(t)}, \tag{8.2}$$

where $\overline{\lambda}(t)$ is the average of the three eigenvalues, measures how spherical the puff is. If $A \approx 0$, all eigenvalues have similar values and the shape of the puff is spherical, while if $A = 1$ one eigenvalue dominates the others and the puff has the shape of a rod.

8.3 Results

In the following, we analyse puff shape evolution at different stages. In particular, we focus first on the ballistic regime of their motion, and later on the phase in which the velocities of tracers are uncorrelated to those at release. Finally, we study the long term dispersion of puffs, which takes place at times much larger than the integral timescale (*i.e.*, the integral up to infinity of the Lagrangian velocity autocorrelation).

8.3.1 Short term deformation of puffs

In this section, the first stage of puff motion is analysed, in which puffs are still small compared to the size of the channel δ and the velocities of particles are strongly correlated to the initial ones.

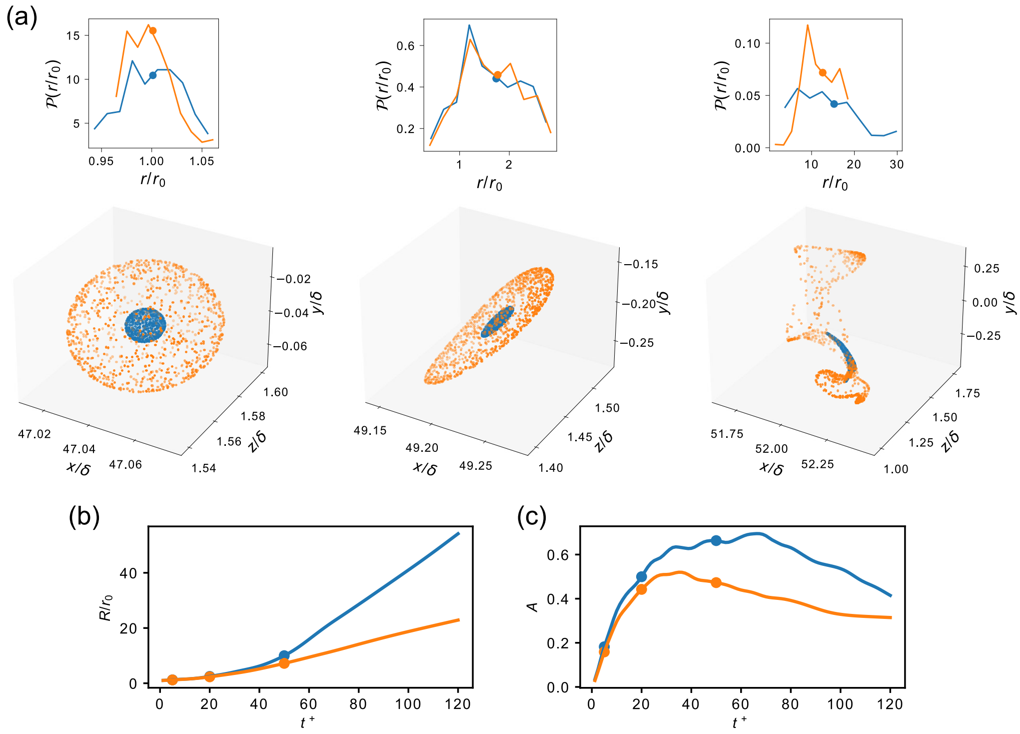

Figure 8.2: a) Shape evolution of two puffs of different radii, released at the same location ($x/\delta = 46$, $y/\delta = 0$), at times $t^+ = 1.25$, $t^+ = 20$ and $t^+ = 50$; the radius of the smaller puff is $r_0^+ = 1.5$, that of the larger is $r_0^+ = 6$. In the inset, the probability density function of the distance of particles from the center of mass of the puff is shown, while dots indicate the average, *i.e.* the radius R (the distance is normalized by r_0 of the puff). b) Time evolution of the radius of the puffs shown above (the larger one in orange color, the smaller in blue); dots indicate the time at which the puffs in panel a) are shown. c) Time evolution of the asphericity of puffs shown above, with the same color-coding.

The shape of a puff with initial radius $r_0^+ = 1.5$ released inside the transitional region ($x/\delta \approx 46$, $y/\delta = 0$) is depicted in figure 8.2(a) in blue color, as an example of puff shape evolution. The shape of the puff is shown in the three panels at three different times: $t^+ = 1.25$ (immediately after release, when the puff is still spherical), $t^+ = 20$ and $t^+ = 50$. The puff remains inside the transitional region in all three panels, as it has travelled a distance $x/\delta \approx 5$ downstream from its release location at $t^+ = 50$. In the insets, the distribution of the distance of particles from the center of mass of the puff is shown, at the same time as the one used to depict the puffs. While for the first inset the distribution is narrow due to particles being located close to their origin, the distribution widens as time passes and puffs are deformed. While most particles are driven apart from each other, some are closer to the center of mass (and also to each other).

Both mean shear and velocity fluctuations contribute to the modification of the shape of puffs. Most importantly, the different local features of the flow field have different effects on puff deformation. In the laminar region only mean shear is present (the Tollmien-Schlichting waves have no significant effect on puff shape as their behaviour is periodic) and puffs stretch along the streamwise direction (except those released on the centreline). On the other hand, further downstream the effects of the transitional and turbulent flow regimes reflect onto puffs, which deform chaotically.

In order to systematically analyse the shape of puffs, we computed the quantities defined in section 8.2. Figure 8.2(b)-(c) show the temporal evolution of the normalized radius of gyration, R/r_0, and the asphericity, A, for the puffs shown above (blue lines). Due to small-scale stretching mechanisms, the radius and the asphericity of puffs rapidly increase after release. Subsequently, we observe that the asphericity decreases, while the rate of increase of the radius grows, but the radius remains small compared to δ. Indeed, as particles sample a larger region of the domain, they are dispersed along all directions by the velocity fluctuations at larger scales, which no longer cause unidirectional stretching. Instead, larger-scale dispersion causes a return to isotropy (reducing the asphericity) and is also more effective (leading to faster radius growth).

The cause of the end of the upward transient of the asphericity is to be found in the increase of spatial scale of the puff and its relation with the flow scales. Conversely, the size of puffs at times later than release depends on the initial scale, which is the main factor that determines the point at which puffs are large enough to be subject to the flow scales that decrease the asphericity. To assess the influence of the initial size r_0 and, consequently, the scale-dependent behaviour of puffs at later times, for each release point in the channel, we placed concentric puffs with different radii r_0, ranging from $r_0^+ = 0.375$ to $r_0^+ = 6$ (the set of concentric puffs closest to the wall is placed with its center at $y^+ = 6$).

Figure 8.2 shows, in orange color, the shape and properties of a puff released at the same location as the aforementioned one, but with a radius $r_0^+ = 6$. Already after a short time, of the order of tens of viscous units, the shape of the two puffs evolve differently. After $t^+ \approx 30$, the normalized radius R/r_0 of the smaller puff grows faster than that of the larger one. It is also notable that the asphericity of the smaller puff is larger.

To further delve on the role of r_0, we show in figure 8.3(a) the ratio $A|_{r_0^+=1.5}/A|_{r_0^+=6}$ between the asphericity of the puffs with $r_0^+ = 1.5$ and the puffs with $r_0^+ = 6$. The ratio between the two values of the asphericity is shown here at time $t^+ = 50$.

Using the sets of concentric puffs released at several locations in the channel, we were able to study their different shape evolution depending on the initial position. Similarly to what was shown in figure 8.2(c), the imbalance between the asphericity of small and large puffs is present everywhere in the transitional and turbulent regions. Instead, the asphericity of puffs of different sizes in the laminar region always has similar values (resulting in a ratio equal or very close to one).

Interestingly, the ratio between the asphericity of small and large puffs is larger in the transitional region than in the turbulent region. Figures 8.3(b)-(c) show the normalized radius and the asphericity with respect to the radius r_0 at three different times (the same as in Figure 8.2), for puffs located in the transitional region ($x/\delta = 46$) and at a wall-normal coordinate $y/\delta = 0$ (the center of the channel). Shortly after release, the shape of puffs evolves independently of r_0. Only after $t^+ \approx 10$ the imbalance arises. From figure 8.3(d) we also notice how the imbalance of the asphericity is stronger in the transitional region (solid lines) than in the turbulent one (dotted lines).

Furthermore, at a later time (shown in red in the figure), the asphericity of puffs in the turbulent region is still increasing, while that of puffs released in the transitional portion of the flow is decreasing (especially for larger puffs). While all puffs follow the general trend shown in figure 8.2(c), the moment at which the asphericity stops its growth depends on the release location and on the initial size. Because of this, the imbalance is able to appear, as puffs released at the same location may evolve differently depending on r_0. In both the transitional and the turbulent region, the imbalance is increasing with time (at least for times that are not much greater than the integral timescale of particles).

Finally, the imbalance is mostly independent of the wall-normal coordinate, as is visible from figure 8.3(a). The effect of shear appears to be the same on puffs of different sizes. Accordingly, the asphericity is scale-independent in the laminar region (where only mean shear is present), while its scale dependence does not depend on y in the transitional and turbulent regions.

In general, puff shape evolution in the transitional and turbulent regions is characterized by two distinct regimes, whose balance depends on the release location and the initial radius. Both regimes take place when puffs are still smaller than the integral scale of the flow δ and for times shorter than the Lagrangian integral timescale. While still happening at relatively short times, the associated behaviours are quite different. The first regime is tightly linked with the initial velocities of particles, due to the very short timescales involved which are well within the ballistic regime. Accordingly, we will show how little shape imbalance can be found during this initial phase. The imbalance regime instead is scale-dependent and linked to the Lagrangian evolution of trajectories beyond the ballistic regime. In the following both regimes will be analysed.

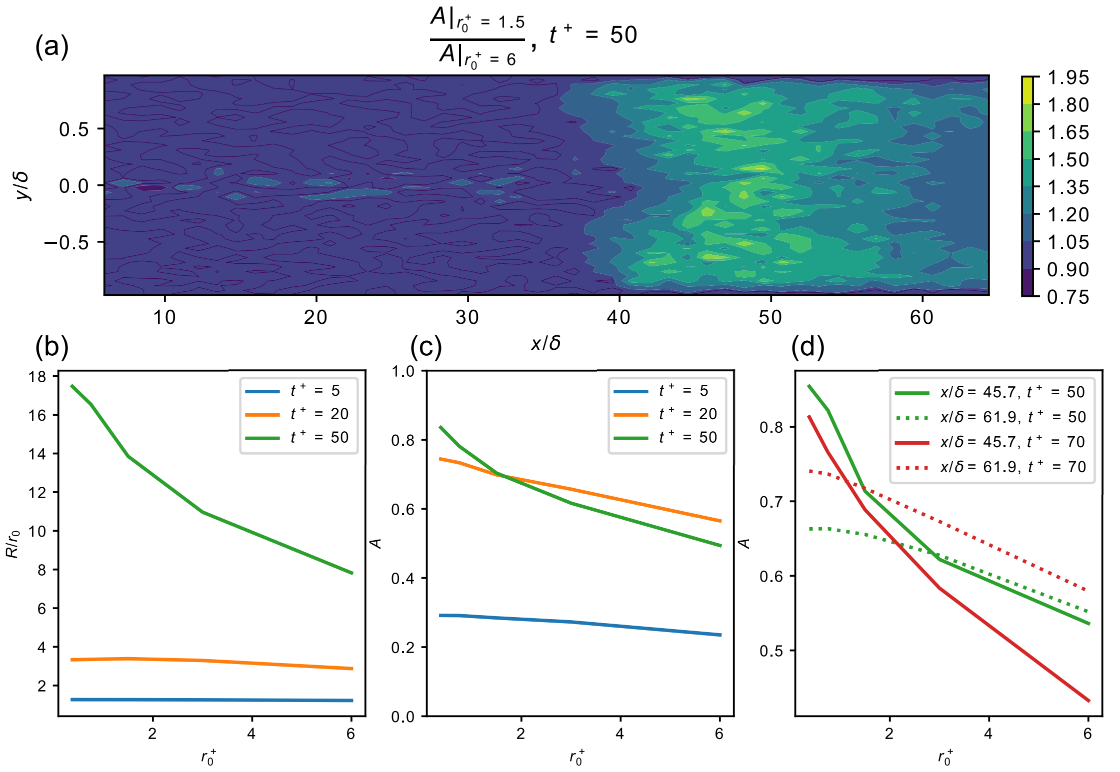

Figure 8.3: a) Ratio between the asphericity for puffs with $r_0^+ = 1.5$ and puffs with $r_0^+ = 6$ at $t^+ = 50$; black contour lines indicate a ratio of one. b) Radius of puffs (normalized by the radius at release) as a function of r_0, shown at subsequent times (puffs released at $x/\delta \approx 46$, $y/\delta = 0$). c) Asphericity of puffs as a function of r_0, shown at subsequent times, same puffs as in (b). d) Asphericity of puffs shown at two different x locations ($x/\delta \approx 46$ in the transitional region and $x/\delta \approx 62$ in the region where turbulence is fully developed), $y/\delta = 0$, and at two different times.

Ballistic regime

In the ballistic regime of particle motion, only the initial velocity of tracers plays a relevant role, as all subsequent values of the velocity are still strongly correlated with it. Accordingly, also puff shapes evolve ballistically, in the sense that their deformation is solely determined by the initial velocity field at the location of the puff.

In this regime, the most important role is played by the initial velocity differences, *i.e.* the local Eulerian structure functions

$$D_{i,j}(r) = \langle (v_i(\mathbf{x} + r\hat{\mathbf{e}}_j) - v_i(\mathbf{x}))^2 \rangle. \tag{8.3}$$

The initial stretching and straining of a puff can be related to the set of velocity differences at its scale, *i.e.*, $2r_0$ (the puff diameter). This is a reasonable approximation, even if the actual deformation reflects the relative motion of N_p^2 particle pairs, whose initial separation may be smaller than or equal to the diameter.

We computed the Eulerian velocity structure function everywhere in the channel domain and at scales r up to the initial size of the largest puffs (that is, twice the value $r^+_{0,\max} = 6$). In homogeneous and isotropic flows, the longitudinal Eulerian structure function ($i = j$ in equation 8.3) follows a power law of the kind $D_{ii}(r) \propto r^\alpha$. The transverse structure functions, instead, follow

$$D_{ij}(r) = D_{ii} + 1/2r\partial_r D_{ii}, \tag{8.4}$$

which is still a power law with the same exponent α as the longitudinal structure function. Accordingly, the ratio between transverse and longitudinal structure functions is independent of the scale r. This independence holds also in our data, even if not from homogeneous and isotropic turbulence. Since the ratio between transverse and longitudinal structure functions is scale-independent, then also its effects on puff shape could not be a function of r.

To further investigate whether the effect of the initial velocities is responsible for the appearance of the imbalance, we computed the asphericity of puffs of different sizes r_0 deformed by the effects of velocity differences at the scale of the puff. To do so, we stretched and sheared puffs using the displacements exerted by the structure functions computed from the simulated velocity field. The coordinates of the synthetically deformed puffs were obtained using

$$x_i(t) = x_i^0 + \sum_{i=1}^{3} x_j^0 \, \frac{t\sqrt{D_{i,j}(r_0)}}{2r_0}. \tag{8.5}$$

The asphericity of these puffs was found to be independent of r_0 for short values of t, consistent with the typical times in which no differences between the asphericity of puffs appeared. This value is of the order of $t^+ = 10$ inside the transitional region (see figures 8.2(b)-(c)). Therefore, the effect of the initial velocity differences is consistent with the observed initial behaviour of puffs, whose shape evolves for very short times independently of r_0. Accordingly, the cause of the appearance of the shape imbalance is not to be found in initial velocity differences, but rather in their later behaviour.

Imbalance regime

Puff behaviour becomes determined by the entire velocity field along their path after the end of the ballistic regime. The imbalance observed previously (recall figure 8.3) is not due to the initial velocity field and is instead linked to the second phase of puff shape evolution, *i.e.* when particles are spread along three dimensions by the velocity fluctuations at intermediate scales. In this new regime the asphericity of larger puffs is, in general, smaller than those of smaller ones, which are more elongated and have rod-like shapes.

We recall that puffs, after being released in the flow, are stretched into elongated shapes with high asphericity, as is shown in figure 8.2. After that, the dispersion of particles by velocity fluctuations at scales larger than that at release results in a decrease of the asphericity. The shift from one behaviour (of growing asphericity) to another (leading to more spherical puffs) is linked to the different features of flow scales at different sizes and, accordingly, strongly depends on the scale of the puff. Initially larger puffs are the first to return to an isotropic shape and reduce their asphericity, because the larger r_0 makes so that they undergo the action of the dispersing flow scales earlier. Although the smaller puffs grow faster than the larger ones, as shown in figure 8.3(b), the non-normalized radius R of the puffs with lower r_0 always remains smaller than that of larger puffs.

We observe the absence of imbalance in the laminar region, indicating that the shape of puffs with different r_0 evolves equally. Furthermore, the magnitude of the imbalance is the same independently of the y coordinate both in the transitional and turbulent region. From this observation, it follows that the effect of the y-dependent mean shear does not contribute to the imbalance. In particular, while it deforms puffs, it does so irrespective of their scale.

The last notable feature regarding the imbalance is the fact that it is larger in the transitional region. In figures 8.4(a)-(b) we report the mean and standard deviation of the three components of the acceleration of particles with respect to the wall-normal coordinate y at two streamwise locations; one is located well inside the transitional region (dotted lines), while the other is in fully developed turbulence (solid lines). We found larger values of the mean and standard deviation of particle acceleration for puffs inside the transitional region. Particles close to the wall have larger mean acceleration, where flow features are also far from isotropy. The intense accelerations to which particles located in the transitional region are subject lead to larger puff deformations.

Additionally, we show the Lagrangian velocity structure function

$$D_{L,i}(\tau) = \langle (v_i(t+\tau) - v_i(t))^2 \rangle, \tag{8.6}$$

which we computed starting from the velocity of particles, at the same two locations as the previous panels, in figure 8.4(c). Again, Lagrangian velocity differences, which are correlated to the acceleration, have far larger magnitude in the transitional region, as a direct result of the more intense velocity fluctuations.

The increased shape imbalance observed in the transitional region is caused by the peculiar features of transitional flow and of the trajectories within. Intermittency, which is linked and induced by transition and is particularly present at the smaller flow scales, determines stronger scale-dependence of puff properties. We have also measured the acceleration of particles belonging to separate puffs, finding that larger puffs have larger acceleration variance (which is due to the larger flow

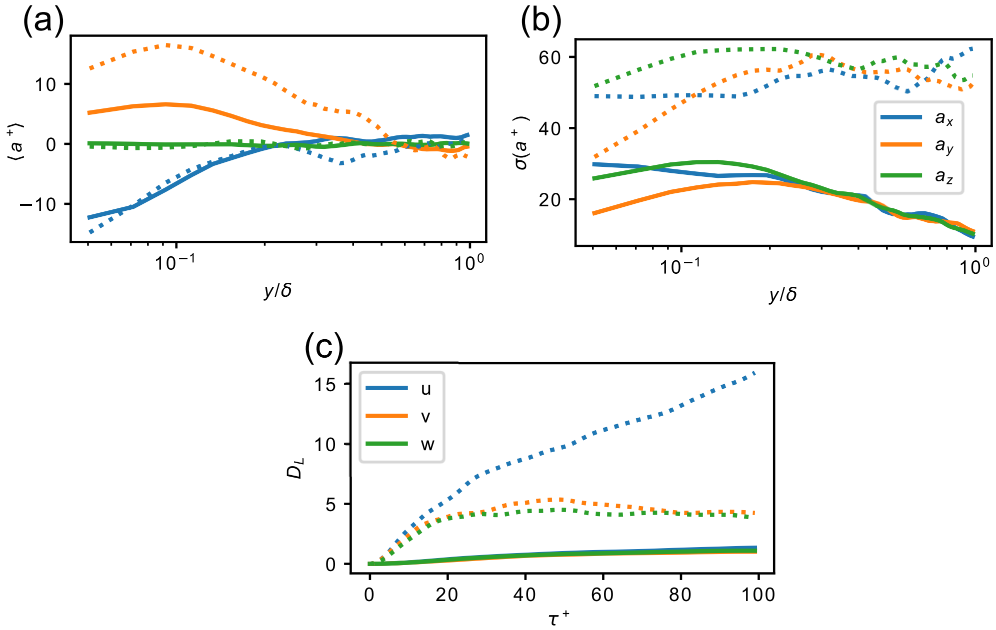

Figure 8.4: (a) Mean of the acceleration of particles depending on the y coordinate. Puffs were released at $x/\delta = 47$ (dashed lines) and $x/\delta = 70$ (solid lines); (b) Standard deviation of the acceleration of particles depending on the y coordinate (same locations as panel (a)); (c) Lagrangian structure functions at the same locations of panel (a), with blue, yellow and green indicating the streamwise, wall-normal and spanwise velocity components, respectively

field they sample), but also that the difference between the acceleration variance of small and large puffs is the largest in the transitional region.

The main features of puff shape evolution can be summarised as follows. The asphericity follows a non-monotonic trend, owing to the interplay between small scales that stretch puffs and larger scales that make their shape spherical again. Because the effects of the flow field are determined by puff size, the shape of puffs with different r_0 evolves differently. An imbalance originates, which is tightly linked to the presence of multiple flow scales. Finally, the small-scale intermittency and the larger intensity of velocity fluctuations in the laminar region make so that the imbalance peaks in the transitional region.

8.3.2 Long term behaviour

During the imbalance regime the action of intermediate flow scales causes the return to isotropy shown in the previous sections. As puffs grow larger they instead start to undergo the action of the largest, integral scales of the flow. These scales are anisotropic because of the geometry of the domain, which forces puffs to become elongated along the streamwise direction and instead bounded along y. This is different from what was observed by Bianchi et al. [21] in a homogeneous and isotropic setting, where the long term behaviour was that of a return to spherical puff shapes.

Figures 8.5(a) and (b) show the radius and the asphericity of puffs with respect to their streamwise x position. Puffs were released at $x/\delta = 30$ (just before the transitional region in the channel domain) and $y/\delta = -0.5$; two different values of r_0 are shown. The increase of R (figure 8.5(a)) slows down as puff size increases. Particle dispersion is now characterized by Taylor's dispersion regime, as the time from release is much larger than the Lagrangian integral timescale.

When the radius of puffs becomes of the order of the size of the channel δ, the main action exerted on puffs is that of mean shear, which advects particles at different velocities depending on their wall distance and thus displaces them into an elongated shape. Furthermore, the channel flow is bounded in the y direction. Both these effects contribute to the final increase of the asphericity after a local minimum is reached. As was the case for the maximum of the asphericity, the minimum is the outcome of the competing actions of the intermediate, isotropic scales and of the largest scales present in the channel that are anisotropic. At long times particles lose all memory of the initial condition, so that puff size r_0 and, to some extent, the release location, are irrelevant to their evolution. This is in stark contrast with the imbalance regime. Accordingly, puffs that have been advected for a long time, such as those shown in figure 8.5, have values of the radius R and the asphericity A that are independent of r_0.

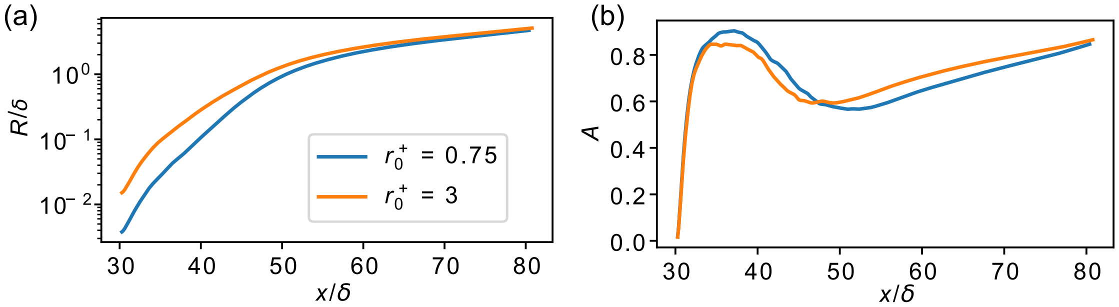

Figure 8.5: (a) Radius of puffs released at $x/\delta = 30$, $y/\delta = -0.5$, with two different values of r_0; (b) Asphericity of the puffs shown in panel (a)

8.3.3 Sensitivity to the number of particles

The measures introduced in section 8.2 were derived from the covariance matrix of particle position which, up to statistical accuracy, is not influenced by the number of particles. Because of this, the method employed in this work is affected only slightly by the number of particles present in each puff. In figure 8.6, we show the same results as in figure 8.3(b)-(c), with the addition of data computed with puffs composed of $N_p = 625$ particles (dotted lines); the results obtained in this way are very similar to those with $N_p = 1024$. We also note how the trends and the presence of the imbalance are unchanged. As long as particles are distributed uniformly in the puff at the time of release, no significant difference in the shape evolution emerges. Of course, the larger N_p, the more accurate the tracking of the puff shape at long times.

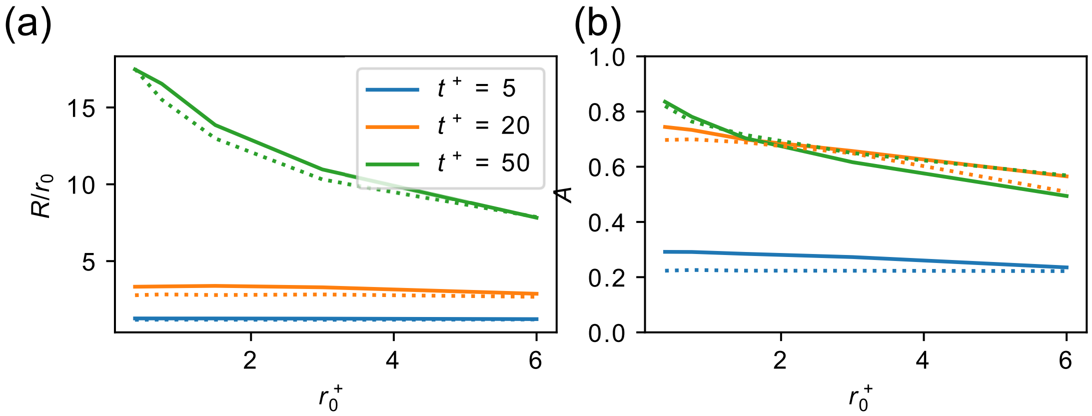

Figure 8.6: a) Radius of puffs (normalized by the radius at release) as a function of r_0, shown at subsequent times (puffs released at $x/\delta \approx 46$, $y/\delta = 0$); here and in the panel on the right, the dotted lines indicate the same results computed with 625 particles, while the solid lines report the results with $N_p = 1024$. b) Asphericity of puffs as a function of r_0, shown at subsequent times (same puffs as in (a)).

8.4 Discussion

Results shown in the previous section show that the overall behaviour of puffs depends on their release location and size, and after release is mostly conditioned by their instantaneous size (which is related to the flow scales exerting a deformation on them).

Shortly after release, puffs are subject to the stretching action of the smallest flow scales found in the transitional and turbulent regions. Due to this action, they become elongated and their asphericity increases. The stretching is related to small-scale Eulerian velocity differences, whose action has scale-independent features.

Accordingly, no imbalance between puffs of different initial sizes appears. Following this scale-independent size increase and elongation, puffs sample larger regions of space, whose flow scales have a dispersive effect of particles. Since this dispersion takes place along all three dimensions, puffs return towards isotropic shapes, causing a reduction of their asphericity.

We analysed the effect of the initial radius of puffs r_0 in order to discern its importance in the later shape evolution. After a short ballistic phase in which motion of puffs is regulated by the Eulerian velocity differences, the shape of puffs evolves differently depending on r_0 in the transitional and turbulent regions of the flow. Smaller puffs are more elongated than their larger counterparts, so that the ratio between the asphericity of small and large puffs (the *imbalance*) is generally larger than one. This is not due to mean shear. Indeed, no imbalance appears in the laminar region (where mean shear is the dominant cause of puff deformation). Furthermore the imbalance shows no dependence on y, indicating that the effect of mean shear on the asphericity is not dependent on the scale of puffs.

Aftere the ballistic regime, puffs with larger initial size are the first to undergo the action of the intermediate flow scales that cause the return to isotropic shapes. In particular, while at smaller scales puffs still evolve according to the local stretching and therefore assume elongated, highly anisotropic shapes, at larger scales particles are instead dispersed along all directions (thus reaching near isotropic shapes) by the intermediate flow scales. These phenomena do not have a clear distinction and are instead competing. The tipping point between the two phenomena (*i.e.*, the maximum value of the asphericity with respect to time) depends on the release location of puffs and on their initial size r_0. Furthermore, these two actions are present together, as puffs can still be locally stretched while larger flow scales reduce their asphericity. Indeed, given the high number of particles and the wide distribution of their pairwise distances, a multitude of flow scales is acting on the shape evolution of the puff at any time. The balance between the two actions is ruled by the (average) size of the puff R; when the size is small, the local stretching effects prevail, otherwise the isotropic dispersion dominates. Because of this, the imbalance of the asphericity appears to be caused by the different scales sampled at the same time by puffs with different r_0.

Most importantly, we found that the imbalance of the asphericity, at any (short) time, is maximum in the transitional region. We have shown how Lagrangian velocity fluctuations and accelerations are stronger and with larger variance in the transitional region, with respect to the rest of the flow and how these fluctuations have different spatial coherence due to small-scale intermittency.

In the transitional region, the asphericity of puffs initially increases for all values of r_0, similarly to what is found in the turbulent regions. Indeed, stretching motions due to velocity differences are linked to continuity at a small length scale and are therefore still present. The higher imbalance of the asphericity found in the transitional region emerges only later, when puffs grow larger. In this region, the balance between local stretching and intermediate-scale dispersion shifts in favour of dispersion (which has isotropic features) only for the larger puffs. This is so because of the less intense velocity fluctuations at small scales (which are nonetheless larger than those responsible for the initial stretching). The root cause is the reduced presence of the dispersing features of the flow (with respect to fully developed turbulence) caused by intermittency and the incompleteness of the energy cascade.

Finally, for very long times, all memory of the initial condition is lost and puffs become very large to the point that their deformation is mostly due to the largest scales of the flow, which because of geometrical constraints and the presence of mean flow cause puffs to become elongated along the streamwise direction. As particle trajectories at this stage have been integrated over times much longer than the integral Lagrangian timescale, the initial condition is no longer relevant to the evolution of puffs; most notably, because of this puffs behave independently of r_0.

Chapter 9

Conclusions

The contributions presented in this thesis are the result of the combination of large quantities of data from high resolution fluid motion simulations and newly developed interpretative approaches.

The association of these aspects is the foundation of the majority of recent advances in fluid dynamics. Computer simulations allow researchers to access unparalleled amounts of data by simulating practically any flow configuration and resolving the entire turbulent flow field. Furthermore, advances in computer systems will inevitably enhance the ability to simulate fluid flows and increase the range of achievable Reynolds numbers.

At the same time, the richness of information obtained through large simulations carries with itself the burden of developing interpretative approaches that are able to investigate the constitutive nature of fluid flows and elaborate large quantities of data into a synthetic representation. This task is made difficult by the complexity inherent to turbulence, but also by the vastness of the data itself.

Accordingly, it is clear that both aspects, *i.e.*, the extension of simulation capabilities and the development of interpretative frameworks, should go hand in hand. Indeed, producing large amounts of fluid flow data is unfruitful if their subsequent analysis is overlooked, also because the quantity of data becomes easily untreatable from a purely computational standpoint. Conversely, methods of analysis should be deeply rooted in the fundamentals of fluid physics, otherwise their results may prove sterile.

This thesis contains contributions both regarding the extension of simulation capabilities and the development of interpretative frameworks, with the ultimate goal of advancing the understanding of wall-bounded turbulence. An existing computer code for the simulation of turbulent channel flow was adapted to include non-periodic boundary conditions, allowing the simulation of transition. The architecture of a new code employing a compact finite differencing scheme and geared for higher Reynolds numbers Re_τ was also delineated.

At the same time, a strong focus in this work was given to explore new ways of systematically studying the data obtained from simulations. The analysis of Lagrangian trajectories provides a viewpoint which is complementary to Eulerian, fixed-point data. Mixing phenomena (as those studied in Chapters 5 and 6) and the deformation of material structures (Chapter 8) are the natural applications of the Lagrangian framework. Its application was shown in this work to be able to describe the features of wall-bounded turbulence, with particular regard to near-wall structures and the intermittency in transitional flows. The application of graph-based approaches as an interpretative framework for fluid flows was widely explored in this thesis. The results obtained show that additional insight on flow physics can be gained by the application of network measures, at the expense of an additional effort regarding the interpretation of results.

We will now briefly summarise the main findings reported in this thesis. In Chapter 5, the wall-normal mixing of tracers was studied in channel flow at varying Reynolds number Re_τ by means of a discrete, network-based representation. The network is built starting from the transition probability of the discretized position of particles, similarly to a Markovian process. Because of this, the network is just the discrete mapping of the wall-normal motion of particles, and network features readily report of the properties of tracer dispersion. The network approach computes the intensity of mixing and highlights the presence of secluded zones that exchange reduced amounts of fluid with the surrounding regions of the channel. Furthermore, the analysis of spectral properties of the network weight matrix highlights the presence of short term attractors of particles, whose existence is limited in time. Furthermore, cyclic motions close to the walls are linked again to reduced dispersion and constitute a dominant pattern of particle motion. Reynolds number scaling was also explored, showing that the overall mixing scales with the outer flow, although closer to the wall this is not always the case. The discretization used to compute the network plays a role in determining the minimum Reynolds number at which Reynolds-independence is achieved.

Mixing of inertial particles at different Stokes numbers in channel flow was analysed in Chapter 6, by counting the particle pairs that come in close proximity. The dependence of mixing properties on the position of particle sources was analysed, highlighting the role of anisotropy in the near wall region. Inertial clustering was shown to be highly dependent on the interplay between the particle timescale (which is ruled by St) and the local flow timescale, which depends on the wall-normal coordinate y. Accordingly, particles with different inertia experience peak clustering at different y locations.

In Chapter 7 we strayed away from the Lagrangian viewpoint to study time-series in a transitional boundary layer using the visibility graph. This methodology consists in transforming the geometry of a fixed-point time-series into a network through a convexity criterion. Network properties were used to measure the intermittency of the time-series and therefore provide an identification of the location of the turbulent-non turbulent interface from fixed-point data. Indeed, the visibility graph was successful in classifying the different flow regions according to the network features.

Finally, in Chapter 8 the deformation of puffs released in transitional channel flow was studied by means of approximate measures of their size and elongation. The deformation of puffs was shown to be highly sensitive on their size, due to the interplay with the flow scales. Notably, small puffs deform into more elongated shapes than larger ones. The interplay between flow scales and puff sizes originates another key feature of puff shape deformation in transitional flow, *i.e.* the increased shape imbalance in the transitional region. Correlating puff properties with flow statistics, we have shown how the increased imbalance is related to intermittency in the transitional flow and to the different distribution of energy across flow scales with respect to turbulence.

Overall, some key aspects emerge from the aforementioned results. Tracers and particles advected in wall-bounded turbulent flows follow (more or less precisely depending on their inertia) the underlying flow field, which is pseudo-chaotic as a direct consequence of the presence of turbulence. While single particle trajectories appear similarly chaotic, when one starts considering sets of them, coherence appears. This is particularly true at short and intermediate timescales, whereas for long times from a certain initial condition the effect of turbulent dispersion is to produce a fully mixed state where no coherent particle distributions may arise. Examples regarding the appearance of coherent patterns include the formation of cyclic motions of particles in the near-wall region of a turbulent channel flow, the formation of clusters depending on particle inertia and the peculiar evolution of puff shapes in transitional channel flow. We have shown that these coherent patterns are not only frequent, but also that they influence and are coupled to the evolution of Lagrangian turbulence. It is impossible to fully understand Lagrangian trajectories without devising methods that are able to account for coherent motions.

The interplay between the coherent features of particle motion and the peculiar aspects of wall turbulence was also considered. Particles sample a field which is statistically non homogeneous and therefore encounter, during their trajectory, regions of the flow with strongly diverse properties. Accordingly, their dispersion is ruled not only by the initial condition and the overall properties of the turbulent flow, but also by the succession of sampled locations along the path of particles (at least before a regime of asymptotic dispersion is achieved). Particles are also subject to the wealth of phenomena that populate the near-wall region, whose flow fields exhibit strong anisotropy which is in turn impressed onto particles. The near-wall features of turbulence are one of the most relevant causes of coherent particle motions in wall-bounded turbulence.

Network-based methods proved apt to tackle both the need to highlight coherent patterns of particle motion and adequately represent the effect of a statistically heterogeneous flow field. This ability is partly due to the fact that interconnections between sets of element emerge somewhat naturally in turbulent flows and can therefore be easily mapped into networks. Nonetheless, care must be ensued to make sure that the graph representation is directly linked to the underlying flow physics. In this way, the network results are unequivocally linked to the flow features and the interpretation of network measures is easier.

The usage of physically-sound network approaches may be extended to more flow cases, including industrial applications and geophysics. The ability of networks to analyse complex flows may indeed shine in this situations. Other network-based approaches can still provide useful results as they can be used as data analysis and classification techniques (as is the case for the visibility graph). Nonetheless, the lack of a clear connection between the graph definition and the flow physics makes the generalization of these techniques difficult and the extraction of information highly dependent on the user. Network approaches have also proven to be resilient when applied to under-resolved data (simply obtained by under-sampling the fully resolved time-series). As such, their application to experimental data and/or to simulations that do not fully resolve the flow field may be fruitful.

High-resolution simulations were key elements in the production of the aforementioned results. Future developments in this sense include the performance tuning of numerical codes in order to make them suitable for larger computer architectures. Furthermore, new numerical algorithms, such as the compact finite difference schemes shown in Chapter 3 can be used to push the boundaries of channel flow simulation with respect to the achievable Reynolds numbers.

The study of coherent particle motions and of the interactions between the Lagrangian features of turbulence and the specific features of wall-bounded flows deserve further investigation. The analysis of Lagrangian trajectories, owing to the strong coupling with the underlying flow field, may be leveraged to deepen the understanding of the basics elements of turbulent flows. Moreover, the complexity of dispersing phenomena can be further analysed, with particular regard to the relationship between the (supposed) appearance of superdiffusive scalings at intermediate timescales and the coherent features of particle motion. Finally, the effect of near-wall structures on the spatial organization of Lagrangian trajectories are dependent on a range of factors (among which are particle inertia, flow Reynolds number and many others) and a full characterization is lacking. This effort may be tackled by conducting particle studies at higher Reynolds number, so that a significant separation of scales is present and therefore a clear identification of inner and outer flow features is achievable.

Bibliography

[1] Réka Albert and Albert-László Barabási. “Statistical mechanics of complex networks”. In: *Rev. Mod. Phys.* 74 (1 Jan. 2002), pp. 47–97. DOI: 10.1103/RevModPhys.74.47.

[2] Francisco Alcántara-Ávila, Sergio Hoyas, and María Jezabel Pérez-Quiles. “Direct numerical simulation of thermal channel flow for $Re_\tau = 5000$ and $Pr = 0.71$”. In: *Journal of Fluid Mechanics* 916 (2021), A29. DOI: 10.1017/jfm.2021.231.

[3] Uri Alon. “Network motifs: theory and experimental approaches”. In: *Nature Reviews Genetics* 8.6 (2007), pp. 450–461. DOI: 10.1038/nrg2102.

[4] Kerstin Avila et al. “The Onset of Turbulence in Pipe Flow”. In: *Science* 333.6039 (2011), pp. 192–196. DOI: 10.1126/science.1203223.

[5] Marc Avila, Dwight Barkley, and Björn Hof. “Transition to Turbulence in Pipe Flow”. In: *Annual Review of Fluid Mechanics* 55.1 (2023), pp. 575–602. DOI: 10.1146/annurev-fluid-120720-025957.

[6] S. Bake, D. G. W. Meyer, and U. Rist. “Turbulence mechanism in Klebanoff transition: a quantitative comparison of experiment and direct numerical simulation”. In: *Journal of Fluid Mechanics* 459 (2002), pp. 217–243. DOI: 10.1017/S0022112002007954.

[7] C.J. Baker. “The turbulent horseshoe vortex”. In: *Journal of Wind Engineering and Industrial Aerodynamics* 6.1 (1980), pp. 9–23. ISSN: 0167-6105. DOI: 10.1016/0167-6105(80)90018-5.

[8] Ralf Banisch, Péter Koltai, and Kathrin Padberg-Gehle. “Network measures of mixing”. In: *Chaos: An Interdisciplinary Journal of Nonlinear Science* 29.6 (2019), p. 063125. DOI: 10.1063/1.5087632.

[9] Albert-László Barabási. “Network science”. In: *Philosophical Transactions of the Royal Society A: Mathematical, Physical and Engineering Sciences* 371.1987 (2013), p. 20120375. DOI: 10.1098/rsta.2012.0375.

[10] Marc Barthelemy. “Betweenness centrality in large complex networks”. In: *The European physical journal B* 38.2 (2004), pp. 163–168. DOI: 10.1140/epjb/e2004-00111-4.

[11] Maxime Bassenne et al. “Extraction of coherent clusters and grid adaptation in particle-laden turbulence using wavelet filters”. In: *Phys. Rev. Fluids* 2 (5 May 2017), p. 054301. DOI: 10.1103/PhysRevFluids.2.054301.

[12] G. K. Batchelor. “The application of the similarity theory of turbulence to atmospheric diffusion”. In: *Quarterly Journal of the Royal Meteorological Society* 76.328 (1950), pp. 133–146. DOI: 10.1002/qj.49707632804.

[13] G. K. Batchelor. “Diffusion in a field of homogeneous turbulence: II. The relative motion of particles”. In: *Mathematical Proceedings of the Cambridge Philosophical Society* 48.2 (1952), pp. 345–362. DOI: 10.1017/S0305004100027687.

[14] George Keith Batchelor and Geoffrey Ingram Taylor. “The effect of homogeneous turbulence on material lines and surfaces”. In: *Proceedings of the Royal Society of London. Series A. Mathematical and Physical Sciences* 213.1114 (1952), pp. 349–366. DOI: 10.1098/rspa.1952.0130.

[15] GK Batchelor. “Diffusion in a field of homogeneous turbulence. I. Eulerian analysis”. In: *Australian Journal of Chemistry* 2.4 (1949), pp. 437–450. DOI: 10.1071/CH9490437.

[16] J. Bec et al. “Heavy Particle Concentration in Turbulence at Dissipative and Inertial Scales”. In: *Phys. Rev. Lett.* 98 (8 Feb. 2007), p. 084502. DOI: 10.1103/PhysRevLett.98.084502.

[17] Jérémie Bec. “Fractal clustering of inertial particles in random flows”. In: *Physics of Fluids* 15.11 (Sept. 2003), pp. L81–L84. ISSN: 1070-6631. DOI: 10.1063/1.1612500.

[18] Jérémie Bec, Holger Homann, and Samriddhi Sankar Ray. “Gravity-Driven Enhancement of Heavy Particle Clustering in Turbulent Flow”. In: *Phys. Rev. Lett.* 112 (18 May 2014), p. 184501. DOI: 10.1103/PhysRevLett.112.184501.

[19] D. W. Bechert et al. “Experiments on drag-reducing surfaces and their optimization with an adjustable geometry”. In: *Journal of Fluid Mechanics* 338 (1997), pp. 59–87. DOI: 10.1017/S0022112096004673.

[20] Shanti Bhushan et al. “Identification of Bypass Transition Onset Markers Using Direct Numerical Simulation”. In: *Journal of Fluids Engineering* 140.11 (June 2018), p. 111107. ISSN: 0098-2202. DOI: 10.1115/1.4040299.

[21] S. Bianchi et al. “On the evolution of particle-puffs in turbulence”. In: *European Journal of Mechanics - B/Fluids* 55 (2016). Vortical Structures and Wall Turbulence, pp. 324–329. ISSN: 0997-7546. DOI: 10.1016/j.euromechflu.2015.06.009.

[22] L. Biferale et al. “Lagrangian statistics of particle pairs in homogeneous isotropic turbulence”. In: *Physics of Fluids* 17.11 (Nov. 2005), p. 115101. ISSN: 1070-6631. DOI: 10.1063/1.2130742.

[23] L. Biferale et al. “Multiparticle dispersion in fully developed turbulence”. In: *Physics of Fluids* 17.11 (Nov. 2005), p. 111701. ISSN: 1070-6631. DOI: 10.1063/1.2130751.

[24] Vincent D Blondel et al. “Fast unfolding of communities in large networks”. In: *Journal of Statistical Mechanics: Theory and Experiment* 2008.10 (2008), P10008. DOI: 10.1088/1742-5468/2008/10/p10008.

[25] S. Boccaletti et al. “Complex networks: Structure and dynamics”. In: *Physics Reports* 424.4 (2006), pp. 175–308. ISSN: 0370-1573. DOI: 10.1016/j.physrep.2005.10.009.

[26] Béla Bollobás. *Modern graph theory*. Vol. 184. Springer Science & Business Media, 1998.

[27] Phillip Bonacich. “Factoring and weighting approaches to status scores and clique identification”. In: *The Journal of Mathematical Sociology* 2.1 (1972), pp. 113–120. DOI: 10.1080/0022250X.1972.9989806.

[28] Guillem Borrell and Javier Jiménez. “Properties of the turbulent/non-turbulent interface in boundary layers”. In: *Journal of Fluid Mechanics* 801 (2016), pp. 554–596. DOI: 10.1017/jfm.2016.430.

[29] Andrew D. Bragg, Peter J. Ireland, and Lance R. Collins. “Mechanisms for the clustering of inertial particles in the inertial range of isotropic turbulence”. In: *Phys. Rev. E* 92 (2 Aug. 2015), p. 023029. DOI: 10.1103/PhysRevE.92.023029.

[30] Andrew D. Bragg, Peter J. Ireland, and Lance R. Collins. “Forward and backward in time dispersion of fluid and inertial particles in isotropic turbulence”. In: *Physics of Fluids* 28.1 (Jan. 2016), p. 013305. ISSN: 1070-6631. DOI: 10.1063/1.4939694.

[31] Luca Brandt and Filippo Coletti. “Particle-Laden Turbulence: Progress and Perspectives”. In: *Annual Review of Fluid Mechanics* 54.1 (2022), pp. 159–189. DOI: 10.1146/annurev-fluid-030121-021103.

[32] John W. Brooke et al. “Turbulent deposition and trapping of aerosols at a wall”. In: *Physics of Fluids A: Fluid Dynamics* 4.4 (Apr. 1992), pp. 825–834. ISSN: 0899-8213. DOI: 10.1063/1.858299.

[33] J. J. H. Brouwers. “Langevin and diffusion equation of turbulent fluid flow”. In: *Physics of Fluids* 22.8 (Aug. 2010), p. 085102. ISSN: 1070-6631. DOI: 10.1063/1.3466658.

[34] J. J. H. Brouwers. “Langevin equation of a fluid particle in wall-induced turbulence”. In: *Theoretical and Mathematical Physics* 163 (2010), pp. 677–695. DOI: 10.1007/s11232-010-0050-2.

[35] D. Buaria, Brian L. Sawford, and P. K. Yeung. "Characteristics of backward and forward two-particle relative dispersion in turbulence at different Reynolds numbers". In: *Physics of Fluids* 27.10 (Oct. 2015), p. 105101. ISSN: 1070-6631. DOI: `10.1063/1.4931602`.

[36] D. Buaria et al. "Single-particle Lagrangian statistics from direct numerical simulations of rotating-stratified turbulence". In: *Phys. Rev. Fluids* 5 (6 June 2020), p. 064801. DOI: `10.1103/PhysRevFluids.5.064801`.

[37] Enrico Calzavarini et al. "Quantifying Turbulence-Induced Segregation of Inertial Particles". In: *Phys. Rev. Lett.* 101 (8 Aug. 2008), p. 084504. DOI: `10.1103/PhysRevLett.101.084504`.

[38] Claudio Canuto et al. *Spectral methods: fundamentals in single domains.* Springer Science & Business Media, 2007.

[39] Rohit Chandra. *Parallel programming in OpenMP.* Morgan kaufmann, 2001.

[40] A. K. Charakopoulos et al. "The application of complex network time series analysis in turbulent heated jets". In: *Chaos: An Interdisciplinary Journal of Nonlinear Science* 24.2 (2014), p. 024408. DOI: `10.1063/1.4875040`.

[41] Avraam Charakopoulos, Theodoros Karakasidis, and Ioannis Sarris. "Analysis of magnetohydrodynamic channel flow through complex network analysis". In: *Chaos: An Interdisciplinary Journal of Nonlinear Science* 31.4 (2021), p. 043123. DOI: `10.1063/5.0043817`.

[42] Kapil Chauhan et al. "The turbulent/non-turbulent interface and entrainment in a boundary layer". In: *Journal of Fluid Mechanics* 742 (2014), pp. 119–151. DOI: `10.1017/jfm.2013.641`.

[43] L. Chen, S. Goto, and J. C. Vassilicos. "Turbulent clustering of stagnation points and inertial particles". In: *Journal of Fluid Mechanics* 553 (2006), pp. 143–154. DOI: `10.1017/S0022112006009177`.

[44] Jung-Il Choi, Kyongmin Yeo, and Changhoon Lee. "Lagrangian statistics in turbulent channel flow". In: *Physics of Fluids* 16.3 (Feb. 2004), pp. 779–793. ISSN: 1070-6631. DOI: `10.1063/1.1644576`.

[45] Subharthi Chowdhuri, Giovanni Iacobello, and Tirtha Banerjee. "Visibility network analysis of large-scale intermittency in convective surface layer turbulence". In: *Journal of Fluid Mechanics* 925 (2021), A38. DOI: `10.1017/jfm.2021.720`.

[46] Lyndon Clarke, Ian Glendinning, and Rolf Hempel. "The MPI message passing interface standard". In: *Programming Environments for Massively Parallel Distributed Systems: Working Conference of the IFIP WG 10.3, April 25–29, 1994*. Springer. 1994, pp. 213–218.

[47] C. T. Crowe, R. A. Fore, and T. R. Troutt. “Particle dispersion by coherent structures in free shear flows”. In: *Particulate Science and Technology* 3.3-4 (1985), pp. 149–158. DOI: 10.1080/02726358508906434.

[48] Michael Dellnitz et al. “Seasonal variability of the subpolar gyres in the Southern Ocean: a numerical investigation based on transfer operators.” In: *Nonlinear Processes in Geophysics* 16.6 (2009).

[49] Edsger W Dijkstra. “A note on two problems in connexion with graphs”. In: *Numer. Math.* (1959), pp. 269–271. DOI: 10.1007/BF01386390.

[50] Henk A Dijkstra et al. *Networks in climate*. Cambridge University Press, 2019.

[51] Luca Donetti and Miguel A Muñoz. “Detecting network communities: a new systematic and efficient algorithm”. In: *Journal of Statistical Mechanics: Theory and Experiment* 2004.10 (Oct. 2004), P10012. DOI: 10.1088/1742-5468/2004/10/P10012.

[52] Reik V. Donner, Emilio Hernández-García, and Enrico Ser-Giacomi. “Introduction to Focus Issue: Complex network perspectives on flow systems”. In: *Chaos: An Interdisciplinary Journal of Nonlinear Science* 27.3 (2017), p. 035601. DOI: 10.1063/1.4979129.

[53] Reik V. Donner et al. “Recurrence-based time series analysis by means of complex network methods”. In: *International Journal of Bifurcation and Chaos* 21.04 (2011), pp. 1019–1046. DOI: 10.1142/S0218127411029021.

[54] S. N. Dorogovtsev and J. F. F. Mendes. “Evolution of networks”. In: *Advances in Physics* 51.4 (2002), pp. 1079–1187. DOI: 10.1080/00018730110112519.

[55] Yiqing Du and George Em Karniadakis. “Suppressing Wall Turbulence by Means of a Transverse Traveling Wave”. In: *Science* 288.5469 (2000), pp. 1230–1234. DOI: 10.1126/science.288.5469.1230.

[56] Bruno Eckhardt et al. “Turbulence Transition in Pipe Flow”. In: *Annual Review of Fluid Mechanics* 39.1 (2007), pp. 447–468. DOI: 10.1146/annurev.fluid.39.050905.110308.

[57] *Eigen library*. https://eigen.tuxfamily.org/index.php?title=Main_Page. [Online; accessed 25th October 2023]. 2023.

[58] G.E. Elsinga, T. Ishihara, and J.C.R. Hunt. “Non-local dispersion and the reassessment of Richardson’s t3-scaling law”. In: *Journal of Fluid Mechanics* 932 (2022), A17. DOI: 10.1017/jfm.2021.989.

[59] Paul Erdős, Alfréd Rényi, et al. “On the evolution of random graphs”. In: *Publ. math. inst. hung. acad. sci* 5.1 (1960), pp. 17–60.

[60] Mahdi Esmaily-Moghadam and Ali Mani. “Analysis of the clustering of inertial particles in turbulent flows”. In: *Phys. Rev. Fluids* 1 (8 Dec. 2016), p. 084202. DOI: 10.1103/PhysRevFluids.1.084202.

[61] L. da F. Costa et al. “Characterization of complex networks: A survey of measurements”. In: *Advances in Physics* 56.1 (2007), pp. 167–242. DOI: `10.1080/00018730601170527`.

[62] Giorgio Fagiolo. “Clustering in complex directed networks”. In: *Phys. Rev. E* 76 (2 2007), p. 026107. DOI: `10.1103/PhysRevE.76.026107`.

[63] Gregory Falkovich et al. “On Lagrangian single-particle statistics”. In: *Physics of Fluids* 24.5 (May 2012), p. 055102. ISSN: 1070-6631. DOI: `10.1063/1.4711397`.

[64] M. Farhan, F. C. G. A. Nicolleau, and A. F. Nowakowski. “Effect of gravity on clustering patterns and inertial particle attractors in kinematic simulations”. In: *Phys. Rev. E* 91 (4 Apr. 2015), p. 043021. DOI: `10.1103/PhysRevE.91.043021`.

[65] A. Ferrante and S. Elghobashi. “On the physical mechanisms of two-way coupling in particle-laden isotropic turbulence”. In: *Physics of Fluids* 15.2 (Jan. 2003), pp. 315–329. ISSN: 1070-6631. DOI: `10.1063/1.1532731`.

[66] Kee Onn Fong, Omid Amili, and Filippo Coletti. “Velocity and spatial distribution of inertial particles in a turbulent channel flow”. In: *Journal of Fluid Mechanics* 872 (2019), pp. 367–406. DOI: `10.1017/jfm.2019.355`.

[67] Luciano da Fontoura Costa et al. “Analyzing and modeling real-world phenomena with complex networks: a survey of applications”. In: *Advances in Physics* 60.3 (2011), pp. 329–412. DOI: `10.1080/00018732.2011.572452`.

[68] Jens H. M. Fransson et al. “Delaying Transition to Turbulence by a Passive Mechanism”. In: *Phys. Rev. Lett.* 96 (6 Feb. 2006), p. 064501. DOI: `10.1103/PhysRevLett.96.064501`.

[69] Uriel Frisch. *Turbulence: The Legacy of A. N. Kolmogorov*. Cambridge University Press, 1995. DOI: `10.1017/CBO9781139170666`.

[70] Gary Froyland. “Statistically optimal almost-invariant sets”. In: *Physica D: Nonlinear Phenomena* 200.3 (2005), pp. 205–219. ISSN: 0167-2789. DOI: `10.1016/j.physd.2004.11.008`.

[71] Gary Froyland and Kathrin Padberg. “Almost-invariant sets and invariant manifolds - Connecting probabilistic and geometric descriptions of coherent structures in flows”. In: *Physica D: Nonlinear Phenomena* 238.16 (2009), pp. 1507–1523. ISSN: 0167-2789. DOI: `10.1016/j.physd.2009.03.002`.

[72] Gary Froyland et al. “Detection of Coherent Oceanic Structures via Transfer Operators”. In: *Phys. Rev. Lett.* 98 (22 May 2007), p. 224503. DOI: `10.1103/PhysRevLett.98.224503`.

[73] Zhong-Ke Gao et al. “Recurrence networks from multivariate signals for uncovering dynamic transitions of horizontal oil-water stratified flows”. In: *Europhysics Letters* 103.5 (Sept. 2013), p. 50004. DOI: `10.1209/0295-5075/103/50004`.

[74] Michelle Girvan and Mark EJ Newman. “Community structure in social and biological networks”. In: *Proceedings of the national academy of sciences* 99.12 (2002), pp. 7821–7826. DOI: `10.1073/pnas.122653799`.

[75] V. Godavarthi et al. “Recurrence networks to study dynamical transitions in a turbulent combustor”. In: *Chaos: An Interdisciplinary Journal of Nonlinear Science* 27.6 (2017), p. 063113. DOI: `10.1063/1.4985275`.

[76] Sébastien Gomé, Laurette S. Tuckerman, and Dwight Barkley. “Statistical transition to turbulence in plane channel flow”. In: *Phys. Rev. Fluids* 5 (8 Aug. 2020), p. 083905. DOI: `10.1103/PhysRevFluids.5.083905`.

[77] Susumu Goto and J. C. Vassilicos. “Sweep-Stick Mechanism of Heavy Particle Clustering in Fluid Turbulence”. In: *Phys. Rev. Lett.* 100 (5 Feb. 2008), p. 054503. DOI: `10.1103/PhysRevLett.100.054503`.

[78] P. Gualtieri, F. Picano, and C. M. Casciola. “Anisotropic clustering of inertial particles in homogeneous shear flow”. In: *Journal of Fluid Mechanics* 629 (2009), pp. 25–39. DOI: `10.1017/S002211200900648X`.

[79] J. F. Hackl, P. K. Yeung, and B. L. Sawford. “Multi-particle and tetrad statistics in numerical simulations of turbulent relative dispersion”. In: *Physics of Fluids* 23.6 (June 2011), p. 065103. ISSN: 1070-6631. DOI: `10.1063/1.3586803`.

[80] Alireza Hadjighasem et al. “Spectral-clustering approach to Lagrangian vortex detection”. In: *Phys. Rev. E* 93 (6 June 2016), p. 063107. DOI: `10.1103/PhysRevE.93.063107`.

[81] George Haller. “Lagrangian Coherent Structures”. In: *Annual Review of Fluid Mechanics* 47.1 (2015), pp. 137–162. DOI: `10.1146/annurev-fluid-010313-141322`.

[82] Adam Hammond and Hui Meng. “Particle radial distribution function and relative velocity measurement in turbulence at small particle-pair separations”. In: *Journal of Fluid Mechanics* 921 (2021), A16. DOI: `10.1017/jfm.2021.486`.

[83] M. A. T. van Hinsberg et al. “Optimal interpolation schemes for particle tracking in turbulence”. In: *Phys. Rev. E* 87 (4 Apr. 2013), p. 043307. DOI: `10.1103/PhysRevE.87.043307`.

[84] Björn Hof et al. “Eliminating Turbulence in Spatially Intermittent Flows”. In: *Science* 327.5972 (2010), pp. 1491–1494. DOI: `10.1126/science.1186091`.

[85] Sergio Hoyas et al. “Wall turbulence at high friction Reynolds numbers”. In: *Phys. Rev. Fluids* 7 (1 Jan. 2022), p. 014602. DOI: 10.1103/PhysRevFluids.7.014602.

[86] G. Iacobello, L. Ridolfi, and S. Scarsoglio. “A review on turbulent and vortical flow analyses via complex networks”. In: *Physica A: Statistical Mechanics and its Applications* 563 (2021), p. 125476. ISSN: 0378-4371. DOI: 10.1016/j.physa.2020.125476.

[87] G. Iacobello et al. “Experimental investigation of vertical turbulent transport of a passive scalar in a boundary layer: Statistics and visibility graph analysis”. In: *Phys. Rev. Fluids* 4 (10 2019), p. 104501. DOI: 10.1103/PhysRevFluids.4.104501.

[88] Giovanni Iacobello, Luca Ridolfi, and Stefania Scarsoglio. “Large-to-small scale frequency modulation analysis in wall-bounded turbulence via visibility networks”. In: *Journal of Fluid Mechanics* 918 (2021), A13. DOI: 10.1017/jfm.2021.279.

[89] Giovanni Iacobello and David E Rival. “Identifying dominant flow features from very-sparse Lagrangian data: a multiscale recurrence network-based approach”. In: *Experiments in fluids* 64.10 (2023), p. 157. DOI: 10.1007/s00348-023-03700-0.

[90] Giovanni Iacobello, Stefania Scarsoglio, and Luca Ridolfi. “Visibility graph analysis of wall turbulence time-series”. In: *Physics Letters A* 382.1 (2018), pp. 1–11. DOI: 10.1016/j.physleta.2017.10.027.

[91] Giovanni Iacobello et al. “Spatial characterization of turbulent channel flow via complex networks”. In: *Physical Review E* 98.1 (2018), p. 013107. DOI: 10.1103/PhysRevE.98.013107.

[92] Giovanni Iacobello et al. “Lagrangian network analysis of turbulent mixing”. In: *Journal of Fluid Mechanics* 865 (2019), pp. 546–562. DOI: 10.1017/jfm.2019.79.

[93] Giovanni Iacobello et al. “Coherent structures at the origin of time irreversibility in wall turbulence”. In: *Communications Physics* 6.1 (2023), p. 91. DOI: 10.1038/s42005-023-01215-y.

[94] Alessio Innocenti et al. “Lagrangian stochastic modelling of acceleration in turbulent wall-bounded flows”. In: *Journal of Fluid Mechanics* 892 (2020), A38. DOI: 10.1017/jfm.2020.203.

[95] Donald J. Jacobs et al. “Protein flexibility predictions using graph theory”. In: *Proteins: Structure, Function, and Bioinformatics* 44.2 (2001), pp. 150–165. DOI: 10.1002/prot.1081.

[96] Robert G. Jacobs and Paul A. Durbin. “Shear sheltering and the continuous spectrum of the Orr-Sommerfeld equation”. In: *Physics of Fluids* 10.8 (Aug. 1998), pp. 2006–2011. ISSN: 1070-6631. DOI: `10.1063/1.869716`.

[97] J. Jeong et al. “Coherent structures near the wall in a turbulent channel flow”. In: *Journal of Fluid Mechanics* 332 (1997), pp. 185–214. DOI: `10.1017/S0022112096003965`.

[98] Javier Jiménez. “Near-wall turbulence”. In: *Physics of Fluids* 25.10 (Oct. 2013), p. 101302. ISSN: 1070-6631. DOI: `10.1063/1.4824988`.

[99] Javier Jiménez and Alfredo Pinelli. “The autonomous cycle of near-wall turbulence”. In: *Journal of Fluid Mechanics* 389 (1999), pp. 335–359. DOI: `10.1017/S0022112099005066`.

[100] Jennifer Jucha et al. “Time-reversal-symmetry Breaking in Turbulence”. In: *Phys. Rev. Lett.* 113 (5 July 2014), p. 054501. DOI: `10.1103/PhysRevLett.113.054501`.

[101] Marie-Caroline Jullien, Jérôme Paret, and Patrick Tabeling. “Richardson Pair Dispersion in Two-Dimensional Turbulence”. In: *Phys. Rev. Lett.* 82 (14 Apr. 1999), pp. 2872–2875. DOI: `10.1103/PhysRevLett.82.2872`.

[102] Praveen Kasthuri et al. “Dynamical systems approach to study thermoacoustic transitions in a liquid rocket combustor”. In: *Chaos: An Interdisciplinary Journal of Nonlinear Science* 29.10 (2019), p. 103115. DOI: `10.1063/1.5120429`.

[103] R. R. Kerswell and O. R. Tutty. “Recurrence of travelling waves in transitional pipe flow”. In: *Journal of Fluid Mechanics* 584 (2007), pp. 69–102. DOI: `10.1017/S0022112007006301`.

[104] John Kim, Parviz Moin, and Robert Moser. “Turbulence statistics in fully developed channel flow at low Reynolds number”. In: *Journal of Fluid Mechanics* 177 (1987), pp. 133–166. DOI: `10.1017/S0022112087000892`.

[105] Andrey Nikolaevich Kolmogorov. “The local structure of turbulence in incompressible viscous fluid for very large Reynolds”. In: *Numbers. In Dokl. Akad. Nauk SSSR* 30 (1941), p. 301.

[106] K. Hauke Kraemer et al. “Recurrence threshold selection for obtaining robust recurrence characteristics in different embedding dimensions”. In: *Chaos: An Interdisciplinary Journal of Nonlinear Science* 28.8 (Aug. 2018), p. 085720. ISSN: 1054-1500. DOI: `10.1063/1.5024914`.

[107] William H. Kruskal and W. Allen Wallis. “Use of Ranks in One-Criterion Variance Analysis”. In: *Journal of the American Statistical Association* 47.260 (1952), pp. 583–621. ISSN: 01621459.

[108] J. G. M. Kuerten. "Subgrid modeling in particle-laden channel flow". In: *Physics of Fluids* 18.2 (Feb. 2006), p. 025108. ISSN: 1070-6631. DOI: `10.1063/1.2176589`.

[109] J. G. M. Kuerten and A. W. Vreman. "Collision frequency and radial distribution function in particle-laden turbulent channel flow". In: *International Journal of Multiphase Flow* 87 (2016), pp. 66–79. ISSN: 0301-9322. DOI: `10.1016/j.ijmultiphaseflow.2016.09.005`.

[110] J. G. M. Kuerten and A. W. Vreman. "Collision frequency and radial distribution function in particle-laden turbulent channel flow". In: *International Journal of Multiphase Flow* 87 (2016), pp. 66–79. ISSN: 0301-9322. DOI: `10.1016/j.ijmultiphaseflow.2016.09.005`.

[111] J.G.M. Kuerten and J.J.H. Brouwers. "Lagrangian statistics of turbulent channel flow at Re_τ= 950 calculated with direct numerical simulation and Langevin models". In: *Physics of fluids* 25.10 (2013), p. 105108. DOI: `10.1063/1.4824795`.

[112] Anubhav Kushwaha, Jae Sung Park, and Michael D. Graham. "Temporal and spatial intermittencies within channel flow turbulence near transition". In: *Phys. Rev. Fluids* 2 (2 Feb. 2017), p. 024603. DOI: `10.1103/PhysRevFluids.2.024603`.

[113] Lucas Lacasa and Raul Toral. "Description of stochastic and chaotic series using visibility graphs". In: *Phys. Rev. E* 82 (3 2010), p. 036120. DOI: `10.1103/PhysRevE.82.036120`.

[114] Lucas Lacasa et al. "From time series to complex networks: The visibility graph". In: *Proceedings of the National Academy of Sciences* 105.13 (2008), pp. 4972–4975. DOI: `10.1073/pnas.0709247105`.

[115] Lucas Lacasa et al. "Time series irreversibility: a visibility graph approach". In: *The European Physical Journal B* 85 (2012), pp. 1–11. DOI: `10.1140/epjb/e2012-20809-8`.

[116] Xin Lan et al. "Fast transformation from time series to visibility graphs". In: *Chaos: An Interdisciplinary Journal of Nonlinear Science* 25.8 (2015), p. 083105. DOI: `10.1063/1.4927835`.

[117] O E Lanford. "The Strange Attractor Theory of Turbulence". In: *Annual Review of Fluid Mechanics* 14.1 (1982), pp. 347–364. DOI: `10.1146/annurev.fl.14.010182.002023`.

[118] Elizabeth A Leicht and Mark EJ Newman. "Community structure in directed networks". In: *Physical review letters* 100.11 (2008), p. 118703. DOI: `10.1103/physrevlett.100.118703`.

[119] Sanjiva K. Lele. “Compact finite difference schemes with spectral-like resolution”. In: *Journal of Computational Physics* 103.1 (1992), pp. 16–42. ISSN: 0021-9991. DOI: `10.1016/0021-9991(92)90324-R`.

[120] Yi Li et al. “A public turbulence database cluster and applications to study Lagrangian evolution of velocity increments in turbulence”. In: *Journal of Turbulence* 9 (2008), N31. DOI: `10.1080/14685240802376389`.

[121] Yuanqing Liu et al. “Life and death of inertial particle clusters in turbulence”. In: *Journal of Fluid Mechanics* 902 (2020), R1. DOI: `10.1017/jfm.2020.710`.

[122] Miquel F. Llop, Narcis Gascons, and Francesc X. Llauró. “Recurrence plots to characterize gas-solid fluidization regimes”. In: *International Journal of Multiphase Flow* 73 (2015), pp. 43–56. ISSN: 0301-9322. DOI: `10.1016/j.ijmultiphaseflow.2015.03.003`.

[123] Federico Lluesma-Rodríguez et al. “A Code for Simulating Heat Transfer in Turbulent Channel Flow”. In: *Mathematics* 9.7 (2021). ISSN: 2227-7390. DOI: `10.3390/math9070756`.

[124] Paolo Luchini. “Universality of the Turbulent Velocity Profile”. In: *Phys. Rev. Lett.* 118 (22 June 2017), p. 224501. DOI: `10.1103/PhysRevLett.118.224501`.

[125] William I. Machaca Abregu, Enzo A. Dari, and Federico E. Teruel. “Study of the spatial transition in a plane channel flow”. In: *Computers and Fluids* 247 (2022), p. 105650. ISSN: 0045-7930. DOI: `10.1016/j.compfluid.2022.105650`.

[126] C. Marchioli et al. “Statistics of particle dispersion in direct numerical simulations of wall-bounded turbulence: Results of an international collaborative benchmark test”. In: *International Journal of Multiphase Flow* 34.9 (2008), pp. 879–893. ISSN: 0301-9322. DOI: `10.1016/j.ijmultiphaseflow.2008.01.009`.

[127] Cristian Marchioli, Maurizio Picciotto, and Alfredo Soldati. “Particle dispersion and wall-dependent turbulent flow scales: implications for local equilibrium models”. In: *Journal of Turbulence* 7 (2006), N60. DOI: `10.1080/14685240600925171`.

[128] Cristian Marchioli and Alfredo Soldati. “Mechanisms for particle transfer and segregation in a turbulent boundary layer”. In: *Journal of Fluid Mechanics* 468 (2002), pp. 283–315. DOI: `10.1017/S0022112002001738`.

[129] Shawn Martin et al. “OpenOrd: an open-source toolbox for large graph layout”. In: *Visualization and Data Analysis 2011*. Ed. by Pak Chung Wong et al. Vol. 7868. International Society for Optics and Photonics. SPIE, 2011, pp. 45–55. DOI: `10.1117/12.871402`.

[130] Martin R. Maxey and James J. Riley. “Equation of motion for a small rigid sphere in a nonuniform flow”. In: *The Physics of Fluids* 26.4 (Apr. 1983), pp. 883–889. ISSN: 0031-9171. DOI: `10.1063/1.864230`.

[131] I. M. Mazzitelli et al. “Pair and multi-particle dispersion in numerical simulations of convective boundary layer turbulence”. In: *Physics of Fluids* 26.5 (May 2014), p. 055110. ISSN: 1070-6631. DOI: `10.1063/1.4878318`.

[132] John B. McLaughlin. “Aerosol particle deposition in numerically simulated channel flow”. In: *Physics of Fluids A: Fluid Dynamics* 1.7 (July 1989), pp. 1211–1224. ISSN: 0899-8213. DOI: `10.1063/1.857344`.

[133] Yoichi Mito and Thomas J Hanratty. “Use of a modified Langevin equation to describe turbulent dispersion of fluid particles in a channel flow”. In: *Flow, turbulence and combustion* 68 (2002), pp. 1–26. DOI: `10.1023/A:1015614823809`.

[134] Parviz Moin and Krishnan Mahesh. “Direct numerical simulation: a tool in turbulence research”. In: *Annual review of fluid mechanics* 30.1 (1998), pp. 539–578.

[135] R. Monchaux, M. Bourgoin, and A. Cartellier. “Preferential concentration of heavy particles: A Voronoï analysis”. In: *Physics of Fluids* 22.10 (2010), p. 103304. DOI: `10.1063/1.3489987`.

[136] Romain Monchaux, Mickael Bourgoin, and Alain Cartellier. “Analyzing preferential concentration and clustering of inertial particles in turbulence”. In: *International Journal of Multiphase Flow* 40 (2012), pp. 1–18. ISSN: 0301-9322. DOI: `10.1016/j.ijmultiphaseflow.2011.12.001`.

[137] L. F. Mortimer, D. O. Njobuenwu, and M. Fairweather. “Near-wall dynamics of inertial particles in dilute turbulent channel flows”. In: *Physics of Fluids* 31.6 (2019), p. 063302. DOI: `10.1063/1.5093391`.

[138] M. E. J. Newman. “Analysis of weighted networks”. In: *Phys. Rev. E* 70 (5 Nov. 2004), p. 056131. DOI: `10.1103/PhysRevE.70.056131`.

[139] M. E. J. Newman and M. Girvan. “Finding and evaluating community structure in networks”. In: *Phys. Rev. E* 69 (2 2004), p. 026113. DOI: `10.1103/PhysRevE.69.026113`.

[140] Mark Newman. *Networks*. Oxford university press, 2018.

[141] Mark EJ Newman. “Detecting community structure in networks”. In: *The European physical journal B* 38.2 (2004), pp. 321–330. DOI: `10.1140/epjb/e2004-00124-y`.

[142] Quoc Nguyen and Dimitrios V. Papavassiliou. “Scalar Mixing in Anisotropic Turbulent Flow”. In: *AIChE Journal* 64.7 (2018), pp. 2803–2815. ISSN: 1547-5905. DOI: `10.1002/aic.16104`.

[143] Kevin P. Nolan and Tamer A. Zaki. "Conditional sampling of transitional boundary layers in pressure gradients". In: *Journal of Fluid Mechanics* 728 (2013), pp. 306–339. DOI: 10.1017/jfm.2013.287.

[144] Rogier Noldus and Piet Van Mieghem. "Assortativity in complex networks". In: *Journal of Complex Networks* 3.4 (Mar. 2015), pp. 507–542. ISSN: 2051-1310. DOI: 10.1093/comnet/cnv005.

[145] Yuji Nomi et al. "Complex network analysis of spatiotemporal dynamics of premixed flame in a Hele-Shaw cell: A transition from chaos to stochastic state". In: *Chaos: An Interdisciplinary Journal of Nonlinear Science* 31.12 (2021), p. 123133. DOI: 10.1063/5.0070526.

[146] Jan Nordström, Niklas Nordin, and Dan Henningson. "The Fringe Region Technique and the Fourier Method Used in the Direct Numerical Simulation of Spatially Evolving Viscous Flows". In: *SIAM Journal on Scientific Computing* 20.4 (1999), pp. 1365–1393. DOI: 10.1137/S1064827596310251.

[147] A Obukhov. "On the distribution of energy in the spectrum of turbulent flow". In: *Dokl. Akad. Nauk SSSR*. Vol. 32. 1941, p. 22.

[148] A.M. Obukhov. "Description of Turbulence in Terms of Lagrangian Variables". In: ed. by H.E. Landsberg and J. Van Mieghem. Vol. 6. Advances in Geophysics. Elsevier, 1959, pp. 113–116. DOI: 10.1016/S0065-2687(08)60098-9.

[149] Benoit Oesterlé and Leonid I. Zaichik. "On Lagrangian time scales and particle dispersion modeling in equilibrium turbulent shear flows". In: *Physics of Fluids* 16.9 (July 2004), pp. 3374–3384. ISSN: 1070-6631. DOI: 10.1063/1.1773844.

[150] Sunao Oka and Susumu Goto. "Generalized sweep-stick mechanism of inertial-particle clustering in turbulence". In: *Phys. Rev. Fluids* 6 (4 Apr. 2021), p. 044605. DOI: 10.1103/PhysRevFluids.6.044605.

[151] William M.F. Orr. "The stability or instability of the steady motions of a perfect liquid and of a viscous liquid. Part II: A viscous liquid". In: *Proceedings of the Royal Irish Academy. Section A: Mathematical and Physical Sciences*. Vol. 27. 1907, pp. 69–138.

[152] Steven A. Orszag. "Accurate solution of the Orr-Sommerfeld stability equation". In: *Journal of Fluid Mechanics* 50.4 (1971), pp. 689–703. DOI: 10.1017/S0022112071002842.

[153] Nobuyuki Otsu. "A Threshold Selection Method from Gray-Level Histograms". In: *IEEE Transactions on Systems, Man, and Cybernetics* 9.1 (1979), pp. 62–66. DOI: 10.1109/TSMC.1979.4310076.

[154] Thibault Oujia, Keigo Matsuda, and Kai Schneider. “Divergence and Convergence of Inertial Particles in High-Reynolds-number Turbulence”. In: *Journal of Fluid Mechanics* 905 (Dec. 2020). ISSN: 0022-1120, 1469-7645. DOI: `10.1017/jfm.2020.672`.

[155] K. Padberg-Gehle and C. Schneide. “Network-based study of Lagrangian transport and mixing”. In: *Nonlinear Processes in Geophysics* 24.4 (2017), pp. 661–671. DOI: `10.5194/npg-24-661-2017`.

[156] Jae Sung Park and Michael D. Graham. “Exact coherent states and connections to turbulent dynamics in minimal channel flow”. In: *Journal of Fluid Mechanics* 782 (2015), pp. 430–454. DOI: `10.1017/jfm.2015.554`.

[157] Yongnam Park and Changhoon Lee. “Gravity-driven clustering of inertial particles in turbulence”. In: *Phys. Rev. E* 89 (6 June 2014), p. 061004. DOI: `10.1103/PhysRevE.89.061004`.

[158] Jr. Patterson G. S. and Steven A. Orszag. “Spectral Calculations of Isotropic Turbulence: Efficient Removal of Aliasing Interactions”. In: *The Physics of Fluids* 14.11 (Nov. 1971), pp. 2538–2541. ISSN: 0031-9171. DOI: `10.1063/1.1693365`.

[159] Eric Perlman et al. “Data exploration of turbulence simulations using a database cluster”. In: *SC ’07: Proceedings of the 2007 ACM/IEEE Conference on Supercomputing*. 2007, pp. 1–11. DOI: `10.1145/1362622.1362654`.

[160] W. Pfenninger. “Boundary layer suction experiments with laminar flow at high Reynolds numbers in the inlet length of a tube by various suction methods”. In: *Boundary Layer and Flow Control*. Ed. by G.V. Lachmann. Pergamon, 1961, pp. 961–980. ISBN: 978-1-4832-1323-1. DOI: `10.1016/B978-1-4832-1323-1.50013-0`.

[161] U. Piomelli. “Large-eddy simulation: achievements and challenges”. In: *Progress in Aerospace Sciences* 35.4 (1999), pp. 335–362. ISSN: 0376-0421. DOI: `10.1016/S0376-0421(98)00014-1`.

[162] Enrico Pitton et al. “Anisotropy in pair dispersion of inertial particles in turbulent channel flow”. In: *Physics of Fluids* 24.7 (July 2012), p. 073305. ISSN: 1070-6631. DOI: `10.1063/1.4737655`.

[163] J.I. Polanco et al. “Relative dispersion of particle pairs in turbulent channel flow”. In: *International Journal of Heat and Fluid Flow* 71 (2018), pp. 231–245. ISSN: 0142-727X. DOI: `10.1016/j.ijheatfluidflow.2018.04.007`.

[164] Juan Ignacio Polanco. “Lagrangian properties of turbulent channel flow : a numerical study”. Theses. Université de Lyon, Mar. 2019.

[165] S.B. Pope. “PDF methods for turbulent reactive flows”. In: *Progress in Energy and Combustion Science* 11.2 (1985), pp. 119–192. ISSN: 0360-1285. DOI: `10.1016/0360-1285(85)90002-4`.

[166] Stephen B Pope. *Turbulent flows.* Cambridge university press, 2000.

[167] Satish C. Reddy et al. “On stability of streamwise streaks and transition thresholds in plane channel flows”. In: *Journal of Fluid Mechanics* 365 (1998), pp. 269–303. DOI: 10.1017/S0022112098001323.

[168] Osborne Reynolds. “XXIX. An experimental investigation of the circumstances which determine whether the motion of water shall be direct or sinuous, and of the law of resistance in parallel channels”. In: *Philosophical Transactions of the Royal society of London* 174 (1883), pp. 935–982.

[169] Lewis Fry Richardson and Gilbert Thomas Walker. “Atmospheric diffusion shown on a distance-neighbour graph”. In: *Proceedings of the Royal Society of London. Series A, Containing Papers of a Mathematical and Physical Character* 110.756 (1926), pp. 709–737.

[170] Victor Rodríguez-Méndez, Enrico Ser-Giacomi, and Emilio Hernández-García. “Clustering coefficient and periodic orbits in flow networks”. In: *Chaos: An Interdisciplinary Journal of Nonlinear Science* 27.3 (2017), p. 035803. DOI: 10.1063/1.4971787.

[171] Damian W. I. Rouson and John K. Eaton. “On the preferential concentration of solid particles in turbulent channel flow”. In: *Journal of Fluid Mechanics* 428 (2001), pp. 149–169. DOI: 10.1017/S0022112000002627.

[172] S.G Rubin and P.K Khosla. “Polynomial interpolation methods for viscous flow calculations”. In: *Journal of Computational Physics* 24.3 (1977), pp. 217–244. ISSN: 0021-9991. DOI: 10.1016/0021-9991(77)90036-5.

[173] I. I. Rypina, S. G. Llewellyn Smith, and L. J. Pratt. “Connection between encounter volume and diffusivity in geophysical flows”. In: *Nonlinear Processes in Geophysics* 25.2 (2018), pp. 267–278. DOI: 10.5194/npg-25-267-2018.

[174] Irina I. Rypina and Lawrence J. Pratt. “Trajectory Encounter Volume as a Diagnostic of Mixing Potential in Fluid Flows”. In: *Nonlinear Processes in Geophysics* 24.2 (2017), pp. 189–202. DOI: 10.5194/npg-24-189-2017.

[175] Juan P. L. C. Salazar et al. “Experimental and numerical investigation of inertial particle clustering in isotropic turbulence”. In: *Journal of Fluid Mechanics* 600 (2008), pp. 245–256. DOI: 10.1017/S0022112008000372.

[176] Juan P.L.C. Salazar and Lance R. Collins. “Two-Particle Dispersion in Isotropic Turbulent Flows”. In: *Annual Review of Fluid Mechanics* 41.1 (2009), pp. 405–432. DOI: 10.1146/annurev.fluid.40.111406.102224.

[177] N. D. Sandham and L. Kleiser. “The late stages of transition to turbulence in channel flow”. In: *Journal of Fluid Mechanics* 245 (1992), pp. 319–348. DOI: 10.1017/S002211209200048X.

[178] Masaki Sano and Keiichi Tamai. “A universal transition to turbulence in channel flow”. In: *Nature Physics* 12.3 (2016), pp. 249–253. DOI: 10.1038/nphys3659.

[179] G. Sardina et al. “Wall accumulation and spatial localization in particle-laden wall flows”. In: *Journal of Fluid Mechanics* 699 (2012), pp. 50–78. DOI: 10.1017/jfm.2012.65.

[180] Benoit Saussol. “An introduction to quantitative Poincaré recurrence in dynamical systems”. In: *Reviews in Mathematical Physics* 21.08 (2009), pp. 949–979. DOI: 10.1142/S0129055X09003785.

[181] Ewe Wei Saw et al. “Inertial Clustering of Particles in High-Reynolds-Number Turbulence”. In: *Phys. Rev. Lett.* 100 (21 May 2008), p. 214501. DOI: 10.1103/PhysRevLett.100.214501.

[182] B. L. Sawford. “Generalized random forcing in random-walk turbulent dispersion models”. In: *The Physics of Fluids* 29.11 (1986), pp. 3582–3585. DOI: 10.1063/1.865784.

[183] B. L. Sawford and P. K. Yeung. “Lagrangian statistics in uniform shear flow: Direct numerical simulation and Lagrangian stochastic models”. In: *Physics of Fluids* 13.9 (Sept. 2001), pp. 2627–2634. ISSN: 1070-6631. DOI: 10.1063/1.1388539.

[184] Brian Sawford. “Turbulent relative dispersion”. In: *Annual Review of Fluid Mechanics* 33.1 (2001), pp. 289–317. DOI: 10.1146/annurev.fluid.33.1.289.

[185] Stefania Scarsoglio, Giovanni Iacobello, and Luca Ridolfi. “Complex networks unveiling spatial patterns in turbulence”. In: *International Journal of Bifurcation and Chaos* 26.13 (2016), p. 1650223.

[186] Stefania Scarsoglio, Francesco Laio, and Luca Ridolfi. “Climate dynamics: a network-based approach for the analysis of global precipitation”. In: *PLoS One* 8.8 (2013), e71129. DOI: 10.1371/journal.pone.0071129.

[187] Philipp Schlatter, Steffen Stolz, and Leonhard Kleiser. “Large-eddy simulation of spatial transition in plane channel flow”. In: *Journal of Turbulence* 7 (2006), N33. DOI: 10.1080/14685240600602929.

[188] Philipp Schlatter et al. “On streak breakdown in bypass transition”. In: *Physics of Fluids* 20.10 (Oct. 2008), p. 101505. ISSN: 1070-6631. DOI: 10.1063/1.3005836.

[189] Kristy L Schlueter-Kuck and John O Dabiri. “Coherent structure colouring: identification of coherent structures from sparse data using graph theory”. In: *Journal of Fluid Mechanics* 811 (2017), pp. 468–486. DOI: 10.1017/jfm.2016.755.

[190] Christiane Schneide et al. “Probing turbulent superstructures in Rayleigh-Bénard convection by Lagrangian trajectory clusters”. In: *Phys. Rev. Fluids* 3 (11 Nov. 2018), p. 113501. DOI: 10.1103/PhysRevFluids.3.113501.

[191] Christiane Schneide et al. “Lagrangian coherent sets in turbulent Rayleigh-Bénard convection”. In: *Phys. Rev. E* 100 (5 Nov. 2019), p. 053103. DOI: 10.1103/PhysRevE.100.053103.

[192] Alice C. Schwarze and Mason A. Porter. “Motifs for Processes on Networks”. In: *SIAM Journal on Applied Dynamical Systems* 20.4 (2021), pp. 2516–2557. DOI: 10.1137/20M1361602.

[193] Enrico Ser-Giacomi et al. “Flow networks: A characterization of geophysical fluid transport”. In: *Chaos: An Interdisciplinary Journal of Nonlinear Science* 25.3 (2015), p. 036404. DOI: 10.1063/1.4908231.

[194] Alexander J. Smits, Beverley J. McKeon, and Ivan Marusic. “High-Reynolds Number Wall Turbulence”. In: *Annual Review of Fluid Mechanics* 43.1 (2011), pp. 353–375. DOI: 10.1146/annurev-fluid-122109-160753.

[195] *Snellius hardware*. https://servicedesk.surf.nl/wiki/display/WIKI/Snellius+hardware+and+file+systems. [Online; accessed 25th October 2023]. 2023.

[196] A. Sommerfeld. *Ein Beitrag zur hydrodynamischen Erklärung der turbulenten Flüssigkeitsbewegungen*. 1909.

[197] Philippe R Spalart, Robert D Moser, and Michael M Rogers. “Spectral methods for the Navier-Stokes equations with one infinite and two periodic directions”. In: *Journal of Computational Physics* 96.2 (1991), pp. 297–324. ISSN: 0021-9991. DOI: 10.1016/0021-9991(91)90238-G.

[198] Kyle D. Squires and John K. Eaton. “Lagrangian and Eulerian statistics obtained from direct numerical simulations of homogeneous turbulence”. In: *Physics of Fluids A: Fluid Dynamics* 3.1 (Jan. 1991), pp. 130–143. ISSN: 0899-8213. DOI: 10.1063/1.857872.

[199] Katepalli R. Sreenivasan and Jörg Schumacher. “Lagrangian views on turbulent mixing of passive scalars”. In: *Philosophical Transactions of the Royal Society A: Mathematical, Physical and Engineering Sciences* 368.1916 (2010), pp. 1561–1577. DOI: 10.1098/rsta.2009.0140.

[200] Nickolas Stelzenmuller et al. “Lagrangian acceleration statistics in a turbulent channel flow”. In: *Phys. Rev. Fluids* 2 (5 May 2017), p. 054602. DOI: 10.1103/PhysRevFluids.2.054602.

[201] R. I. Sujith and Vishnu R. Unni. “Complex system approach to investigate and mitigate thermoacoustic instability in turbulent combustors”. In: *Physics of Fluids* 32.6 (2020), p. 061401. DOI: 10.1063/5.0003702.

[202] Christian Szegedy et al. “Some Applications of the weighted combinatorial Laplacian”. PhD thesis. Fakultät der Rheinischen Friedrich-Wilhelms-Universität Bonn, 2005.

[203] Kunihiko Taira and Aditya G. Nair. “Network-based analysis of fluid flows: Progress and outlook”. In: *Progress in Aerospace Sciences* 131 (2022), p. 100823. ISSN: 0376-0421. DOI: `10.1016/j.paerosci.2022.100823`.

[204] Kunihiko Taira, Aditya G. Nair, and Steven L. Brunton. “Network Structure of Two-Dimensional Decaying Isotropic Turbulence”. In: *Journal of Fluid Mechanics* 795 (2016). ISSN: 0022-1120, 1469-7645. DOI: `10.1017/jfm.2016.235`.

[205] Floris Takens. “Detecting strange attractors in turbulence”. In: *Dynamical Systems and Turbulence, Warwick 1980: proceedings of a symposium held at the University of Warwick 1979/80*. Springer. 2006, pp. 366–381.

[206] Shiyong Tan and Rui Ni. “Universality and Intermittency of Pair Dispersion in Turbulence”. In: *Phys. Rev. Lett.* 128 (11 Mar. 2022), p. 114502. DOI: `10.1103/PhysRevLett.128.114502`.

[207] Shruti Tandon and R. I. Sujith. “Condensation in the phase space and network topology during transition from chaos to order in turbulent thermoacoustic systems”. In: *Chaos: An Interdisciplinary Journal of Nonlinear Science* 31.4 (2021), p. 043126. DOI: `10.1063/5.0039229`.

[208] L. Tang et al. “Self-organizing particle dispersion mechanism in a plane wake”. In: *Physics of Fluids A: Fluid Dynamics* 4.10 (Oct. 1992), pp. 2244–2251. ISSN: 0899-8213. DOI: `10.1063/1.858465`.

[209] Robert Tarjan. “Depth-first search and linear graph algorithms”. In: *SIAM journal on computing* 1.2 (1972), pp. 146–160.

[210] Geoffrey I Taylor. “Diffusion by continuous movements”. In: *Proceedings of the London Mathematical Society* 2.1 (1922), pp. 196–212.

[211] Roger Temam. *Navier-Stokes equations: theory and numerical analysis*. Vol. 343. American Mathematical Soc., 2001.

[212] H. A. Kierstead Tomasz Bartnicki Jarosław Grytczuk and Xuding Zhu. “The Map-Coloring Game”. In: *The American Mathematical Monthly* 114.9 (2007), pp. 793–803. DOI: `10.1080/00029890.2007.11920471`.

[213] Federico Toschi and Eberhard Bodenschatz. “Lagrangian Properties of Particles in Turbulence”. In: *Annual Review of Fluid Mechanics* 41.1 (2009), pp. 375–404. DOI: `10.1146/annurev.fluid.010908.165210`.

[214] Philipp P. Vieweg et al. “Lagrangian heat transport in turbulent three-dimensional convection”. In: *Phys. Rev. Fluids* 6 (4 2021), p. L041501. DOI: `10.1103/PhysRevFluids.6.L041501`.

[215] Philipp P. Vieweg et al. “Lagrangian studies of coherent sets and heat transport in constant heat flux-driven turbulent Rayleigh-Bénard convection”. In: *European Journal of Mechanics - B/Fluids* 103 (2024), pp. 69–85. ISSN: 0997-7546. DOI: `10.1016/j.euromechflu.2023.08.007`.

[216] R. Volk et al. “Acceleration of heavy and light particles in turbulence: Comparison between experiments and direct numerical simulations”. In: *Physica D: Nonlinear Phenomena* 237.14 (2008). Euler Equations: 250 Years On, pp. 2084–2089. ISSN: 0167-2789. DOI: `10.1016/j.physd.2008.01.016`.

[217] A. W. Vreman and J. G. M. Kuerten. “Comparison of direct numerical simulation databases of turbulent channel flow at Re = 180”. In: *Physics of Fluids* 26.1 (Jan. 2014), p. 015102. ISSN: 1070-6631. DOI: `10.1063/1.4861064`.

[218] Lian-Ping Wang, Anthony S. Wexler, and Yong Zhou. “Statistical mechanical description and modelling of turbulent collision of inertial particles”. In: *Journal of Fluid Mechanics* 415 (2000), pp. 117–153. DOI: `10.1017/S0022112000008661`.

[219] Qunzhen Wang, Kyle D. Squires, and Xiaohua Wu. “Lagrangian statistics in turbulent channel flow”. In: *Atmospheric Environment* 29.18 (1995), pp. 2417–2427. ISSN: 1352-2310. DOI: `10.1016/1352-2310(95)00190-A`.

[220] Duncan J Watts and Steven H Strogatz. “Collective dynamics of "small-world" networks”. In: *nature* 393.6684 (1998), pp. 440–442. DOI: `10.1038/30918`.

[221] Sebastian Wernicke. “Efficient Detection of Network Motifs”. In: *IEEE/ACM Transactions on Computational Biology and Bioinformatics* 3.4 (2006), pp. 347–359. DOI: `10.1109/TCBB.2006.51`.

[222] John D Wilson and Brian L Sawford. “Review of Lagrangian stochastic models for trajectories in the turbulent atmosphere”. In: *Boundary-layer meteorology* 78 (1996), pp. 191–210. DOI: `10.1007/BF00122492`.

[223] S.X. Yang and C. Luo. “A neural network approach to complete coverage path planning”. In: *IEEE Transactions on Systems, Man, and Cybernetics, Part B (Cybernetics)* 34.1 (2004), pp. 718–724. DOI: `10.1109/TSMCB.2003.811769`.

[224] Chi-An Yeh, Muralikrishnan Gopalakrishnan Meena, and Kunihiko Taira. “Network broadcast analysis and control of turbulent flows”. In: *Journal of Fluid Mechanics* 910 (2021), A15. DOI: `10.1017/jfm.2020.965`.

[225] P. K. Yeung. “One- and two-particle Lagrangian acceleration correlations in numerically simulated homogeneous turbulence”. In: *Physics of Fluids* 9.10 (Oct. 1997), pp. 2981–2990. ISSN: 1070-6631. DOI: `10.1063/1.869409`.

[226] P. K. Yeung. “Lagrangian investigations of turbulence”. In: *Annual Review of Fluid Mechanics* 34.1 (2002), pp. 115–142. DOI: `10.1146/annurev.fluid.34.082101.170725`.

[227] P. K. Yeung and S. B. Pope. “Lagrangian statistics from direct numerical simulations of isotropic turbulence”. In: *Journal of Fluid Mechanics* 207 (1989), pp. 531–586. DOI: `10.1017/S0022112089002697`.

[228] P.K Yeung and S.B Pope. “An algorithm for tracking fluid particles in numerical simulations of homogeneous turbulence”. In: *Journal of Computational Physics* 79.2 (1988), pp. 373–416. ISSN: 0021-9991. DOI: `10.1016/0021-9991(88)90022-8`.

[229] Siti Nurul Akmal Yusuf et al. “A short review on rans turbulence models”. In: *CFD Letters* 12.11 (2020), pp. 83–96.

[230] Tamer A. Zaki. “From Streaks to Spots and on to Turbulence: Exploring the Dynamics of Boundary Layer Transition”. In: *Flow, Turbulence and Combustion* 3.91 (2013), pp. 451–473. ISSN: 1386-6184, 1573-1987. DOI: `10.1007/s10494-013-9502-8`.

[231] Tamer A. Zaki and Paul A. Durbin. “Mode interaction and the bypass route to transition”. In: *Journal of Fluid Mechanics* 531 (2005), pp. 85–111. DOI: `10.1017/S0022112005003800`.

[232] Yu-ning Zhang et al. “A selected review of vortex identification methods with applications”. In: *Journal of Hydrodynamics* 30 (2018), pp. 767–779.

[233] Yong Zou et al. “Complex network approaches to nonlinear time series analysis”. In: *Physics Reports* 787 (2019). Complex network approaches to nonlinear time series analysis, pp. 1–97. ISSN: 0370-1573. DOI: `10.1016/j.physrep.2018.10.005`.

This Ph.D. thesis has been typeset by means of the TEX-system facilities. The typesetting engine was pdfLATEX. The document class was `toptesi`, by Claudio Beccari, with option `tipotesi=scudo`. This class is available in every up-to-date and complete TEX-system installation.